CZECH TECHNICAL UNIVERSITY IN PRAGUE

FACULTY OF BIOMEDICAL ENGINEERING

Department of Biomedical Technology

Microwave imaging for selected medical diagnostic and monitoring applications

From numerical simulations to experimental applications

DOCTORAL THESIS

JAN TESAŘÍK

Kladno, August 2024

Ph.D. programme: Biomedical and Clinical Technology

Supervisor: prof. Dr.-Ing. Jan Vrba, M.Sc.

Microwave imaging for selected medical diagnostic and monitoring applications

JAN TESAŘÍK

Faculty of Biomedical Engineering
Czech Technical University in Prague
Nám. Sítná 3105, 272 01 Kladno, Česká republika
Phone: +420 224 358 419
www.fbmi.cvut.cz

Prohlášení

Prohlašuji, že jsem disertační práci s názvem: "Microwave imaging for selected medical diagnostic and monitoring applications," vypracoval(a) samostatně a uvedl(a) veškeré použité informační zdroje v souladu s Metodickým pokynem O dodržování etických principů při přípravě vysokoškolských závěrečných prací.

Declaration

I hereby declare that I have authored the doctoral thesis: " Microwave imaging for selected medical diagnostic and monitoring applications," on my own using the literature, which I list in the bibliography attached to this work.

In Kladno on

Signature of the author

Abstract

Microwave medical technologies have become a reliable and affordable method over the last three decades. The fact that the dielectric properties of healthy and pathological tissues differ showed a potential to examine the possibilities of using the microwave for both diagnostic and monitoring applications. Microwave imaging – MWI (tomography - MWT) systems have the potential to be an inexpensive, compact and non-harmful modality for patients. Despite the lower resolution, it can complement existing conventional imaging systems and help to improve healthcare quality in the future. The microwave diagnostic method that is considered the most is the early detection of breast cancer and the detection or classification of brain stroke, respectively. In addition, because of the temperature dependence of the dielectric parameters, the microwave thermometry during hyperthermia treatment seems to be a very promising way.

This dissertation thesis is mainly focused on the contribution to medical applications of microwave tomography for the detection of brain stroke and to the feasibility of microwave thermometry for hyperthermia based on the differential microwave imaging approach.

In the thesis, the new methodology for comparison of near-field radiation of different antenna elements was designed and on its basis, the new compact antenna suitable for MWI applications was developed. A laboratory 3D multichannel MWI system for testing of brain stroke detection on homogeneous head and stroke phantoms employing developed antennas was experimentally verified and parameters of the system such as sensitivity were evaluated. Further, the feasibility of microwave thermometry was studied. Experimental measurements on muscle phantom proved the ability of the differential MWI technique to track the trend of temperature progression based on the local change of dielectric properties. To combine hyperthermia and microwave thermometry using one hybrid system, some challenges, such as parameters of water bolus or antenna radiation, must be addressed in the future.

Keywords: Microwave imaging, Microwave tomography, Dielectric properties, Microwave thermometry, Microwave medical applications, Antenna design

Anotace

Mikrovlnné technologie v medicíně se za poslední tři desetiletí staly spolehlivou a dostupnou metodu. Skutečnost, že se dielektrické vlastnosti zdravých a patologických tkání liší, ukázala potenciál pro zkoumání možností využití mikrovln pro diagnostické i monitorovací aplikace. Mikrovlnné zobrazovací (tomografické) systémy mají v současnosti potenciál být levnou, kompaktní a pro pacienty bezpečnou variantou. I přes nižší rozlišovací schopnost mohou doplnit stávající konvenční zobrazovací systémy a v budoucnu pomoci zlepšit kvalitu zdravotní péče. Nejslibnějšími aplikacemi mikrovlnného zobrazování je včasná detekce rakoviny prsu a detekce nebo klasifikace cévní mozkové příhody (CMP). Vzhledem k teplotní závislosti dielektrických parametrů se navíc mikrovlnné zobrazování ukazuje jako velmi vhodné pro termometrii při hypertermické léčbě tumorů tkání.

Tato disertační práce je zaměřena především na přínos mikrovlnné tomografie pro detekci CMP a na proveditelnost mikrovlnné termometrie pro hypertermii pomocí tzv. diferenciálního mikrovlnného zobrazování.

V této práci byla navržena nová metodika pro porovnání vyzařování různých anténních elementů v blízkém poli a na základě této analýzy byla vyvinuta nová kompaktní anténa vhodná pro mikrovlnné zobrazování. Dále byl navržen a experimentálně ověřen laboratorní 3D vícekanálový mikrovlnný zobrazovací systém pro testování detekce CMP na homogenních fantomech lidské hlavy a CMP s využitím vyvinutých antén. Byly také vyhodnoceny parametry systému jako je citlivost. Dále byla v práci studována proveditelnost mikrovlnné termometrie. Experimentální měření na fantomu svalu prokázalo schopnost diferenciálního mikrovlnného zobrazování sledovat trend vývoje teploty na základě lokální změny dielektrických parametrů. Aby bylo možné kombinovat hypertermii a mikrovlnnou termometrii v jednom hybridní systému, je třeba v budoucnu vyřešit některé problémy, především parametry vodního bolu nebo vyzařování použitých antén.

Klíčová slova: Mikrovlnné zobrazování, Mikrovlnná tomografie, Dielektrické parametry, Mikrovlnná termometrie, Lékařské aplikace mikrovlnného záření, Návrh antén

Acknowledgements

First, I would like to thank my supervisor, Prof. Dr.-Ing. Jan Vrba, M.Sc., and also his brother and supervisor-specialist Prof. Ing. David Vrba, Ph.D., for their valuable consultations and advices during my entire doctoral studies.

Also, I would like to thank my colleague and friend Assoc. Prof. Ing. Ondřej Fišer, Ph.D., for his support and motivation.

Last but not least, I thank my family for their endless support and patience.

To my lovely Nina and Nela

CONTENT

List of author's publications

Papers with IF related to the thesis

[A1] **TESAŘÍK, J.,** T. POKORNÝ, and J. VRBA. Dielectric sensitivity of different antennas types for microwave-based head imaging: Numerical study and experimental verification. *International Journal of Microwave and Wireless Technologies*. 2020, 12 982-995. ISSN 1759-0787.
DOI 10.1017/S1759078720000835. **IF: 1,06; citation 1**

[A2] FIŠER, O., HRUBÝ, V., VRBA, J., DŘÍŽĎAL, T., **TESAŘÍK, J**., VRBA, J. Sr. and VRBA, D. UWB Bowtie Antenna for Medical Microwave Imaging Applications. *IEEE Transactions on Antennas and Propagation*. 2022, 70(7), 5357-5372. ISSN 0018-926X. DOI 10.1109/TAP.2022.3161355. **IF: 5,7; citation 12**

[A3] POKORNÝ, T., VRBA, D., **TESAŘÍK, J.,** RODRIGUES, D. B., and VRBA, J. Anatomically and Dielectrically Realistic 2.5D 5-Layer Reconfigurable Head Phantom for Testing Microwave Stroke Detection and Classification. *International Journal of Antennas and Propagation*. 2019, **2019** ISSN 1687-5869. DOI 10.1155/2019/5459391. **IF: 1,21; citation 8**

Conference papers related to the thesis

[A4] **TESAŘÍK, J**., J. VRBA, and H. DOBŠÍČEK TREFNÁ. Non-invasive Thermometry during Hyperthermia Using Differential Microwave Imaging Approach. In: *15th European Conference on Antennas and Propagation*. Düsseldorf, 2021-03-22/2021-03-26. Berlin: IEEE, 2021. ISSN 2164-3342. ISBN 978-88-31299-02-2. DOI 10.23919/EuCAP51087.2021.9411253.

[A5] **TESAŘÍK, J.** and J. VRBA. Validation of Multilevel 24-port Microwave Imaging System for Brain Stroke Monitoring on Synthetic Numerical Data. In: *2020 14TH EUROPEAN CONFERENCE ON ANTENNAS AND PROPAGATION (EUCAP)*. 14th European Conference on Antennas and Propagation, Copenhagen, 2020-03-15/2020-03-20. IEEE (Institute of Electrical and Electronics Engineers), 2020. p. 39-43. ISBN 978-88-31299-00-8. DOI 10.23919/EuCAP48036.2020.9135435.

[A6] **TESAŘÍK, J.,** J. HRNČÍŘ, and T. POKORNÝ. A Design of Geometry and Antennas Layout of 3D Microwave Imaging System for Brain Stroke Monitoring. In: *Progress in Electromagnetics Research Symposium*. 2019 PhotonIcs and Electromagnetics Research Symposium - Spring, PIERS-Spring 2019, Řím, 2019-06-17/2019-06-20. Institute of Electrical and Electronics Engineers, Inc., 2019. p. 3342-3347. ISSN 1559-9450. ISBN 9781728134031. DOI 10.1109/PIERS-Spring46901.2019.9017555.

[A7] **TESAŘÍK, J**. and O. FIŠER. Evaluating of Spatial and Contrast Resolution Ability of 2D Microwave Imaging System. In: *Progress in Electromagnetics Research Symposium*. 2019 PhotonIcs and Electromagnetics Research Symposium - Spring, PIERS-Spring 2019, Řím, 2019-06-17/2019-06-20. Institute of Electrical and Electronics Engineers, Inc., 2019. p. 1428-1433. ISSN 1559-9450. ISBN 9781728134031. DOI [10.1109/PIERS-Spring46901.2019.9017663](https://doi.org/10.1109/PIERS-Spring46901.2019.9017663).

[A8] **TESAŘÍK, J**. and T. POKORNÝ. Dielectric sensitivity of different antennas types for microwave-based head imaging: Numerical study. In: *Proceedings of European Microwave Conference in Central Europe, EuMCE 2019*. 2019 European Microwave Conference in Central Europe, Praha, 2019-05-13/2019-05-15. Louvain-la-Neuve: European Microwave Association (EuMA), 2019. p. 504-507. ISBN 9782874870675.

[A9] **TESAŘÍK, J.,** et al. A Numerical Study of Influence of a Matching Medium on Transmission Coefficients between Antennas Used in Microwave Imaging System. In: *2018 Progress In Electromagnetics Research Symposium (PIERS | Toyama)*. The 40th PIERS in Toyama, JAPAN, Toyama, 2018-08-01/2018-08-04. Cambridge: Electromagnetics Academy, 2018. p. 1076-1080. ISSN 1931-7360. ISBN 9784885523151.

[A10] **TESAŘÍK, J**., T. POKORNÝ, and L. HOLEK. Samples of Dry Head Tissues Phantoms for Brain Stroke Classification. In: *WORLD CONGRESS ON MEDICAL PHYSICS AND BIOMEDICAL ENGINEERING 2018, VOL 3*. World Congress on Medical Physics and Biomedical Engineering 2018, Prague, 2018-06-03/2018-06-08. Springer Nature Singapore Pte Ltd., 2019. p. 775-778. ISSN 1680-0737. ISBN 978-981-10-9022-6. DOI [10.1007/978-981-10-9023-3_140](https://doi.org/10.1007/978-981-10-9023-3_140).

[A11] **TESAŘÍK, J.,** L. DÍAZ RONDÓN, and O. FIŠER. Prototype of Simplified Microwave Imaging System for Brain Stroke Follow Up. In: LHOTSKÁ, L., et al., eds. *World Congress on Medical Physics and Biomedical Engineering 2018*. Prague, 2018-06-03/2018-06-08. Springer Nature Singapore Pte Ltd., 2019. p. 771-774. IFMBE Proceedings. vol. 68/2. ISSN 1680-0737. ISBN 978-981-10-9038-7. DOI [10.1007/978-981-10-9023-3_139](https://doi.org/10.1007/978-981-10-9023-3_139).

[A12] **TESAŘÍK, J.,** J. VRBA, and D. VRBA. Numerical Study of Propagation of EM Waves through Human Head. In: *Proceedings of the 39th PIERS in Singapore*. The 39th PIERS in Singapore, Singapore, 2017-11-19/2017-11-22. Cambridge, MA: The Electromagnetics Academy, 2017. ISSN 1559-9450.

Conference papers not related to the thesis

FIŠER, O. and **TESAŘÍK, J.** Non-contact Monitoring of Respiration and Heart Activity of Infants Using UWB Signals. In: *Progress in Electromagnetics Research Symposium*. 2019 PhotonIcs and Electromagnetics Research Symposium - Spring, PIERS-Spring 2019, Řím, 2019-06-17/2019-06-20. Institute of Electrical and Electronics Engineers, Inc., 2019. p. 2534-2537. ISSN 1559-9450. ISBN 9781728134031. DOI 10.1109/PIERS-Spring46901.2019.9017595

POKORNÝ, T. and **J. TESAŘÍK**. 3D Printed Multi-layer Molds of Human Head Tissue Phantoms for Microwave Stroke Detection. In: *Progress in Electromagnetics Research Symposium*. 2019 PhotonIcs and Electromagnetics Research Symposium - Spring, PIERS-Spring 2019, Řím, 2019-06-17/2019-06-20. Institute of Electrical and Electronics Engineers, Inc., 2019. p. 1424-1427. ISSN 1559-9450. ISBN 9781728134031. DOI 10.1109/PIERS-Spring46901.2019.9017648.

POKORNÝ, T. and **J. TESAŘÍK**. Microwave stroke detection and classification using different methods from MATLAB's classification learner toolbox. In: *Proceedings of European Microwave Conference in Central Europe, EuMCE 2019*. 2019 European Microwave Conference in Central Europe, Praha, 2019-05-13/2019-05-15. Louvain-la-Neuve: European Microwave Association (EuMA), 2019. p. 500-503. ISBN 9782874870675.

DÍAZ RONDÓN, L. and **J. TESAŘÍK**. Processing of standard MR images prior execution of the MR-based electrical properties tomography (MREPT) method. In: LHOTSKÁ, L., et al., eds. *World Congress on Medical Physics and Biomedical Engineering 2018*. Prague, 2018-06-03/2018-06-08. Springer Nature Singapore Pte Ltd., 2019. p. 785-788. IFMBE Proceedings. vol. 68/2. ISSN 1680-0737. ISBN 978-981-10-9038-7.DOI 10.1007/978-981-10-9023-3_142.

KANTOVÁ, M., FIŠER, O., MERUNKA, I., VRBA, J. and **J. TESAŘÍK** et al. High-water Content Phantom for Microwave Imaging and Microwave Hyperthermia. In: LHOTSKÁ, L., et al., eds. *World Congress on Medical Physics and Biomedical Engineering 2018*. Prague, 2018-06-03/2018-06-08. Springer Nature Singapore Pte Ltd., 2019. p. 779-783. IFMBE Proceedings. vol. 68/2. ISSN 1680-0737. ISBN 978-981-10-9038-7. DOI 10.1007/978-981-10-9023-3_141.

1 INTRODUCTION

In the rapidly advancing field of medical diagnostics and monitoring, the quest for non-invasive, cost-effective, portable, and non-harmful alternative technologies to conventional imaging methods such as computed tomography (CT) or magnetic resonance imaging (MRI) is more essential than ever. Microwave Imaging (MWI)/Microwave Tomography (MWT) has been shown to be an adequate candidate. It utilizes the lower part of the microwave frequency band, typically between 500 MHz and 10 GHz of the electromagnetic spectrum, to probe the human body. The principle is grounded in the different scattering of microwaves due to the contrast in dielectric properties between different tissues, healthy and pathological tissues or due to changes in temperature. The scattered electric field can then be measured and processed to reconstruct images of the internal structures of the body.

The history of microwave imaging, especially within the context of medical applications, spans several decades and involves a gradual evolution from theoretical concepts to experimental validations and towards ongoing clinical research studies. The concept of using microwaves for imaging purposes dates back to the mid-20th century. The early applications focused more on industrial and military uses such as radar than on medical diagnostics. Only since the end of 1980s have researchers begun to explore the potential of using MWI for medical imaging purposes. The main initiative was the need for non-invasive and ionizing-radiation-free method. First, theoretical models for microwave imaging were developed, focussing on understanding how microwaves interact with different materials, including biological tissues. In the late 1990s significant progress in computational electromagnetics was made by Taflove and Hagness [1]. The Finite Difference Time Domain (FDTD) method allowed for accurate simulations of microwave interactions with biological tissues and whole body parts and thus gave rise to future medical applications such as early breast cancer detection, prehospital brain stroke classification, or non-invasive 3D real-time thermometry during hyperthermia treatment.

Breast cancer accounts for about 25% of all cancer cases in women, making it the most frequently diagnosed cancer among women worldwide. In 2020, approximately 2.3 million women worldwide were diagnosed with breast cancer [2]

Each X-ray mammography examination by itself increases the risk of cancer formation in the future. Tumorous tissues show increased dielectric properties compared to healthy tissues. The potential of MWI systems is to fully eliminate ionizing radiation while maintaining the sensitivity and specificity.

Apart from the parameters mentioned earlier, primarily portability, high operation speed, and no need for trained professionals allow MWI systems to improve prehospital brain stroke classification in ambulance. Accurate differentiation between ischemic (approx. 80 % of all cases) and hemorrhagic stroke (approx. 19 % of all cases) is crucial to provide proper treatment. A hemorrhagic stroke is manifested by bleeding from a ruptured blood vessel in the brain, and thus, an increase in the values of the dielectric properties in the affected area. An ischemic stroke is caused by the blockage of an artery by a clot, thereby stopping blood flow and oxygenation in a specific part of the brain as shown in Figure 1.1. A decrease in blood content and thus water in the affected area leads to a local decrease in the value of the dielectric properties.

Figure 1.1 Schematic picture of two types of stroke, hemorrhagic on the left and ischemic on the right, adopted and edited from [3].

A typical patient loses 2 million neurones per minute during which the stroke is not treated – "Time *is the brain*" [4]. According to the WSO (*World Stroke Organisation*) over the last 25 years, stroke has become the second leading cause of disability and the second leading cause of death worldwide [5].

Last but not least, the prospective use of microwaves as an intersection of diagnostic and therapeutic technologies in oncology is undoubtedly thermometry during hyperthermia treatment. Hyperthermia involves increasing the temperature of the tumour tissues to 40-45°C to enhance the effectiveness of cancer treatments such as radiation therapy and chemotherapy. Precise temperature monitoring is crucial during hyperthermia to ensure that the therapeutic range is achieved without damaging the surrounding healthy tissues. As the dielectric properties of tissues are temperature dependent, MWI offers a non-invasive approach to real-time thermometry, leveraging the temperature-dependent dielectric properties of tissues. Here again, expensive MRI or invasive optical fibre probes are the current "competitors".

Today, technological advances have led to the development of prototype microwave imaging systems for clinical evaluation. Research efforts have focused on improving image resolution, developing efficient image reconstruction algorithms, and enhancing system development for practical use. Clinical trials have been conducted, particularly in breast cancer detection [6] and brain stroke imaging [7], to evaluate the efficacy and safety of microwave imaging. The main disadvantages of MWI still remain a lower, but acceptable resolution and a computationally more demanding image reconstruction. This could be addressed with computational cluster and accelerations of the numerical simulations using graphical processor units (GPUs) or by adapting the machine learning algorithms trained on large, measured data sets. On the other hand, the utilization of safe radiation, mobility, cost effectivity, and the possibility of untrained use are the current advantages of MWI compared to other imaging modalities as summarised in Table 1.1.

Table 1.1 Comparison of parameters of current imaging modalities and MWI

Feature	CT	MRI	US	MWI
Time resolution	✗	✗	✓	✓
Spatial resolution	~ 0.5 mm	~ 1 mm	~ 5 mm	~ 5 mm*
Untrained use	✗	✗	✗	✓
Safe radiation	✗	✓	✓	✓
Mobility	✗	✗	✓	✓
Cost-effectiveness	✗	✗	✓	✓

*at maximum, depending on used frequency and application

1.1 Thesis concept

Microwave imaging systems for medical applications, despite the potential benefits mentioned above, face several significant challenges that must be addressed. It involves a list of comprehensive technical, computational, and practical tasks. A huge part of the MWI systems development process is dedicated to numerical modelling and solving the inverse scattering problem (using the scattered microwave signals collected around the human body to reconstruct images of the internal tissues). The relationship between the electromagnetic (EM) properties of tissues and the scattered fields is highly nonlinear and ill-posed. Thus, before any measurements, a feasibility study based on, e.g., the finite element method (FEM) or the finite difference time domain (FDTD) method should be performed. Additionally, the heterogeneous and complex nature of biological tissues contributes to its difficulty. Tissues have varying, sometimes overlapping, frequency- and temperature-dependent dielectric properties, which can change over time.

First, the operating frequency range selection needs to be done. It is influenced by the application's specific requirements for penetration depth of EM waves and spatial resolution. We strongly believe that the frequency range with balanced penetration depth and resolution must be numerically validated only on realistic 2D and 3D models of human body parts, e.g. human head, with realistic frequency-dependent dielectric properties.

The second key factor is to design an antenna element that efficiently transmits EM waves in the selected frequency band into the examined domain with minimal loss and distortion. One of the tasks is to reach as wide bandwidth of the antenna as possible to accommodate the broad range of frequencies used in a microwave imaging system. But in our opinion, more important is elimination of backward radiation of antenna and symmetrical feeding/near-field radiation pattern. Additionally, in the field of medical applications, antennae need to be small and compact to facilitate close proximity to the body and to allow the construction of dense antenna arrays. The small physical shape influences the bandwidth. If we take mentioned into account, a paradigm shift in the antenna elements design is thus necessary: from wide-band, radiating to all directions and medium-large antennas to compact antennas, with eliminated backward radiation where a large bandwidth is not crucial.

The next essential challenge for the validation of MWI systems is to develop and fabricate phantoms that mimic the dielectric properties (permittivity and conductivity) of human tissues as well as its anatomical structures.

Common materials include gels (e.g., agarose or gelatin-based), liquids, and solid polymers, often mixed with additives to adjust the dielectric properties as realistic as possible. Gels and liquids evaporate over time and thus change their properties. The lower conformability could be an issue of solid phantoms. We suggest the use of substances such as urethan rubber, acetone, graphite and carbon black powder to create dry phantoms of human tissues as presented in [A3] and [A10]. The final mixture/phantom has stable dielectric properties over time, is easily reconfigurable, and is also quite flexible. The 3D printed moulds are suitable for mixture layering.

The last but not least task relates to the reconstruction of dielectric properties weighted images from measured data. A variety of algorithms based on different approaches such as back projection, inverse scattering, or iterative methods have already been developed. Some of algorithms are computationally demanding, others require forward linear solver or approximation. Algorithms that offer the highest accuracy often lack the necessary speed, making them unsuitable for continuous monitoring applications. We firmly believe that differential imaging algorithms using Born's approximation with selected regularization method are the approach with such a potential.

1.2 Main aims of the thesis

The dissertation thesis focusses mainly on the contribution to applications of microwave imaging/tomography for medical diagnostic and monitoring. The three main aims of the thesis are

(i) design and experimental validation of a suitable antenna element for MWI systems (Chapter 5),

(ii) development and in-laboratory validation of multichannel 3D MWI system for brain stroke detection (Chapter 5),

(iii) feasibility study towards microwave thermometry employing a differential microwave tomography approach (Chapter 6).

Some of the topics related to the thesis, such as numerical analysis of EM wave propagation through human head models or reconstruction algorithms for microwave imaging technique, are described in Chapter 4 or 3, respectively.

1.3 Thesis outline

This thesis is organized as follows.

In Chapter 2 the general concept of microwave imaging or radar-based and microwave tomography approaches ,respectively, is introduced. In addition, the dielectric properties of human tissues and the S-parameters of microwave systems are summarized.

The reconstruction algorithms suitable for the microwave imaging technique are introduced in Chapter 3, especially the linear algorithm based on the Born approximation is described.

Chapter 4 is focused on numerical studies, especially the study of EM wave propagation through human head models, validation of spatial resolution of the MWI method, and comparison of different coupling mediums suitable for use in MWI systems.

The following Chapter 5 deals with the design of the new antenna element, analysing its sensitivity to changes in dielectric properties, and identifying antenna near-field radiation patterns. Comparison with other available antennae for MWI is done as well as antenna validation within the developed 3D multilevel MWI system. The experimental results are analysed, and limitations as well as future perspectives are discussed.

Last but not least, in Chapter 6, we propose experimental real-time non-invasive microwave monitoring of temperature employing implemented linear reconstruction algorithm and differential microwave imaging (dMWI).

2 MICROWAVE IMAGING

Microwave imaging (MWI) is a technique that uses the interaction of microwaves with materials in the imaged area, particularly scattering and attenuation. The interaction is governed by Maxwell's equations [8] and depends, among other things, on the microwave frequencies and dielectric properties of the imaged objects. During imaging, the imaged area is exposed to incident electromagnetic waves and the parameters of the reflected and transmitted waves are measured.

Based on these measurements and solution of inverse scattering problem MWI can provide information about distribution of dielectric properties of body tissues which differs between the tissues, between healthy and pathological tissue and for different temperatures.

In general, MWI can be distinguished on microwave tomography or so-called radar-based approach. In this thesis we deal primarily with microwave tomography and for the sake of clarity the microwave imaging (MWI) and microwave tomography (MWT) are synonymous in this thesis.

2.1 Radar-based approach

This technique operates in the time domain and the location of dielectric contrast can be determined by measuring the delays between incident and both transmitted and reflected ultra-wideband signals. Before reconstruction, estimation of the EM waves propagation speed is necessary. Radar-based methods are primarily used to detect the presence, location or size of scatterers and thus providing “only” qualitative information. Reconstruction is rapid, with the potential for real-time monitoring and works well in media with high contrast. However, the main challenges include the maximum resolution of the reconstructed image, which depends on the pulse bandwidth, potential variations in propagation speed, and the multipath effect (multiple reflections from scatterers). Confocal microwave imaging (CMI), which incorporates the delay-and-sum algorithm, and its improved versions is one of the most commonly used reconstruction method for radar approach [9].

2.2 Microwave tomography

Microwave tomography involves reconstructing an image of the dielectric properties distribution within a region of interest by solving the inverse scattering problem which is more detailed described in [8]. It provides quantitative as well as qualitative information about the internal structure of an object, such as variations in permittivity and conductivity or location and size, respectively. The inverse scattering problem is usually ill-posed, leading to instability in the solutions thus to be solved it requires significant computational power and sophisticated algorithms [10]. When objects have low contrast and multiple scattering effects are minimal, the inverse problem can be linearized using methods such as the Born or Rytov approximations and their enhanced versions [8]. However, if multiple scattering effects are significant, nonlinear reconstruction algorithms are necessary. These algorithms use either linearization techniques or optimization methods, which can be stochastic or deterministic as introduced further in Chapter 3.

2.3 Dielectric properties of human tissues

The electrical behaviour of human tissues can be described by dielectric properties which are defined by so-called complex permittivity $\varepsilon(\omega)$.

$$\varepsilon(\omega) = \varepsilon'(\omega) - j\varepsilon''(\omega) = \varepsilon'(\omega) - j\frac{\sigma(\omega)}{\omega\varepsilon'}, \tag{2.1}$$

where ω is angular frequency, ε' is real part of complex permittivity. It reflects the ability of any tissue to store the electric field energy. The imaginary part ε'' describes dissipative nature of tissues. The absorbed energy is mainly converted into heat. The equivalent electrical conductivity σ is related to imaginary part by the equation above [11]. The dependency of both real and imaginary part of permittivity on frequency is depicted in Figure 2.1.

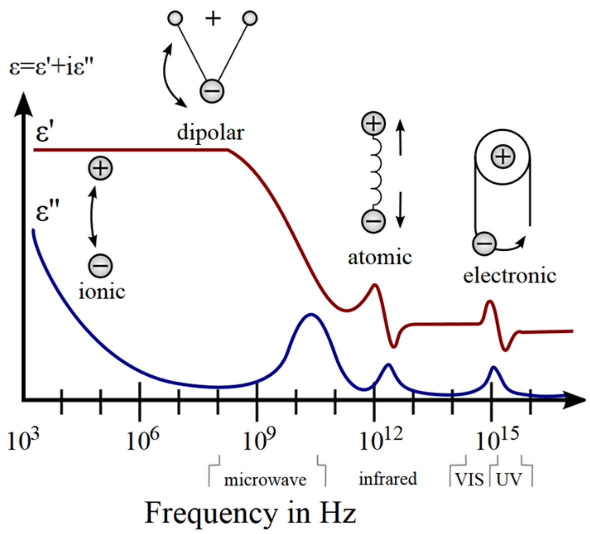

Figure 2.1 Dependency of complex permittivity on frequency. The red curve indicates the real part, and the blue curve the imaginary part [12].

In particular, at specific frequencies, polarisations occur and contribute to dispersions. These dispersion regions reflect the mechanisms that occur in various components of three main dispersion regions, α, β and γ along with other minor dispersions, including the δ to the tissue dielectric behaviour [13].

To describe the frequency behaviour of complex permittivity of human tissues for frequencies of interest some models have been developed. The two most common well-known models are Debey and Cole-Cole model which equations are defined for instance in [14]. These models allow import of dielectric properties of human tissues into numerical studies which are essential in the field of biomedical application of microwave imaging.

Debye model is suitable to approximate frequency dependency of complex permittivity of chemically pure substances (e.g. pure isopropanol or ethanol). It is not adequate for biological tissues. For biological tissues, there are several relaxation processes related to different types of polarization and occurring at different frequencies. According to numerous experimental studies on various tissues, the Cole-Cole equation includes multiple dispersion terms [15], [16].

2.4 S-parameters

S-parameters, so-called Scattering parameters characterize how an *N*-port network reacts to signals applied to any or all of its ports. The first number in the subscript indicates the receiving port, while the second number identifies the transmitting port. The S-parameters enables us to describe the behaviour of the network without the need to know the inner structure of the network. The principle can be shown using the two-port network system as presented in Figure 2.2.

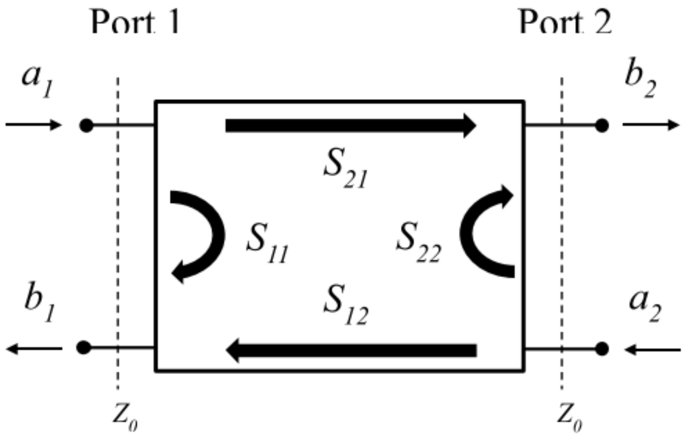

Figure 2.2 Generalized two-port network system with characteristic impedance Z_0 = 50 Ω, adopted and edited from [17].

In case of a 2-port, the complex-valued S-parameters, S_{11}, S_{21}, etc. can be expressed by ratio of complex voltage amplitude waves b_1 and a_1 or b_2 and a_1, respectively [17]. The ratios for S_{11} and S_{21} are derived by setting the incident signal $a_2 = 0$ and solving for the above S-parameter ratios as a function of a_1. Similarly, S_{12} and S_{22} are derived by setting the value of $a_1 = 0$ and solving for the other ratios.

It should be noted here that the above relations are valid in the case of knowledge of the value of the reference impedance of the ports (line), which is most often equal to 50 Ω in the case of microwave measurements. If we want to ensure the highest possible transmission of the electromagnetic wave (power) to the investigation domain, it is always necessary to match the impedance of the circuits (antennas) with the reference impedance. Typically, values of magnitude of S_{11} under –10 dB are desirable. Then less than 10 % of the incident power is reflected back to the generator.

3 CHAPTER: RECONSTRUCTION ALGORITHMS FOR MWI TECHNIQUE

3.1 Introduction

In the literature, reconstruction algorithms can be basically differentiated into two main categories: (1) linear (model-based) reconstruction algorithms and (2) nonlinear (iterative) algorithms [8], [10]. These two kinds of algorithms solve an inverse scattering problem to obtain dielectric properties in the investigation domain; they are also known as inverse scattering methods. Comparison of their parameters are summarized in Table 3.1.

In general, by linear methods, qualitative reconstructions can be obtained, e.g. the presence, position, and size of a target. The greatest advantage of these methods is their computational effectiveness; they are relatively simple, fast, and robust. These parameters favour the linear reconstruction algorithm for real-time monitoring applications. In addition, if the condition of weak scatterer is fulfilled, i.e. targets to be imaged inside the investigation object have low dielectric contrast against the background, it is also possible to obtain not only position and size of stroke, but also quantitative information (dielectric properties of object of interest) by these methods.

The principle of iterative (nonlinear) algorithms is to minimise the error between estimated (forward solver) and measured values of the scattered electrical field [8] in certain number of iterations. Two different iterative approaches can be distinguished [10]. The first approach uses the cost function which is based on the difference between the measured and predicted scattered electric fields to estimate the electrical properties of a given material. The second approach considers cost functions such as 'contrast sources', which relate the electric fields to the contrast of the unknown object of interest. Their disadvantage is computationally intensive, especially for large-scale problems or complex models, and the dependence of convergence on chosen parameters. Basically, at each iteration the algorithms call the forward solver to compute scattered electrical fields and then seek the dielectric properties of object (quantitative reconstruction) of interest by minimizing the cost function. Iterative methods are also limited by the need for a priori information.

Table 3.1 Comparison of parameters of linear and iterative reconstruction methods.

Aspect	Linear algorithms	Iterative algorithms
Basic principle	Direct computation of the solution using linear algebraic techniques	Solution refinement through iterative updates based on measured data and a predefined objective function
Convergence	Converges to the exact solution in a finite number of steps for well-posed problems	Converges to a solution through successive iterations, with convergence criteria determining stopping conditions
Computational complexity	Computationally efficient	Computationally intensive, particularly for large-scale or ill-posed problems, due to repeated computations and memory storage
Robustness to noise	May be sensitive to noise and measurement errors, particularly for ill-conditioned problems	Can be more robust to noise and errors, as regularization techniques and convergence criteria can mitigate their effects
Applicability	Well-suited for real-time monitoring applications.	Suitable for nonlinear, ill-posed, or noisy problems
Examples	Diffraction tomography, (Distorted) Born approximation	Distorted Born iterative method, Gauss-Newton

3.1.1 Linear reconstruction algorithms

Linear reconstruction methods exploit linear approximations like Born, Rytov, or Kirchhoff approximations, making them similar to inversion algorithms in CT. According to [8] the most common linear methods are diffraction tomography (DT) and Born approximation method (BA)/Distorted Born approximation (DBA). DT is based on the collection of the scattered electric field along a straight probing line located at a given distance Y_0 from the object and outside of the object at the same time. The basic principle is shown in Figure 3.1.

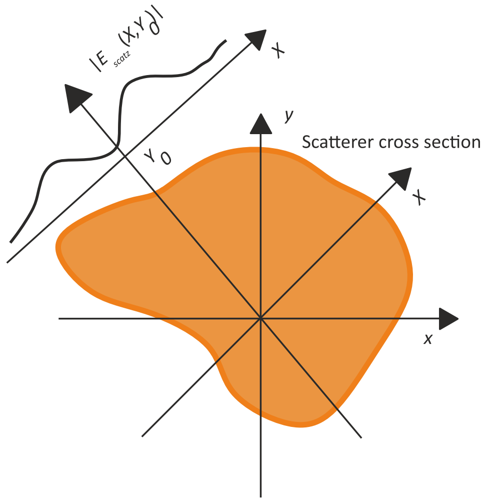

Figure 3.1 2D imaging configuration for diffraction tomography, adopted from [8].

The spatial resolution of diffraction tomography is limited by $\lambda/2$ [18] and it is not comparable to the resolution of conventional imaging systems based on X-rays. BA/DBA can be represented as a linear equation with only one unknown variable since the electric field is known everywhere. It is a linear inverse problem. To reach a stable solution, regularization schemes such as TSVD (Truncated Singular Values Decomposition) or Tikhonov regularization must be used [8]. The total electric field (x, y, z) at the measurement points is computed numerically using a forward solver. By the linear combination of these electric field components, a linear operator is created.

A linear operator is decomposed by TVSD. Calculation of electric fields using the forward solver is time consumable, and therefore it is carried out in advance [19]. This operator, together with measured S parameters, is the basis for calculating of the object function which describes a distribution of complex permittivity in the investigating domain. BA for microwave stroke monitoring has been described, for example, in [20], [21]. Its mathematical formulation is introduced in one of the following subchapters.

3.1.2 Iterative reconstruction algorithms

There coexist different iterative reconstruction methods. For example, Distorted Bron Iterative Approximation (DBIM), where an initial object function is iteratively updated until a stopping condition is reached. At each iteration, the first-order DBA is applied. DBIM is described more in [22]. The DBIM method was presented, for example, in 2013 in the study [23]. The authors used synthetic data obtained by numerical simulations of a realistic 2D head model. Reconstructions of the distribution of dielectric parameters showed individual tissues of a realistic head model. Reconstruction took 4 hours and is therefore not suitable for real-time measurements.

However, quantitative methods can also be divided into deterministic (local optimisation) or stochastic (global optimisation) [10]. Deterministic methods minimize the cost function using the Newton-type minimization (e.g., Gauss-Newton or Newton-Kantorovich) and always require some kind of regularization technique, the most often Tikhonov regularization, which is described, for example, in [24]. These regularizations work well when there are only a few scatterers with a small difference in dielectric properties (contrast) [10]. The main advantage of deterministic methods is their convergence speed.

Data provided by the second generation of MWI system designed at FBME [25] were reconstructed using a Gauss-Newton (GN) deterministic algorithm together with Tikhonov regularization. The results showed that the use of the GN algorithm led to a successful reconstruction of hemorrhagic stroke phantoms placed in the liquid phantom of a human head at 23 different positions. Some of the effects that could negatively influence measurements were discussed, and recommendations for future measurements were specified. Reconstructions were time-consuming, which can be reduced by using different forward solver (FDTD-based) and GPU acceleration in the future.

Among stochastic quantitative algorithms, there are especially population-based evolutionary algorithms such as neural networks (NN) or genetic algorithms (GAs) [10]. A stochastic approach is always a better choice if multiple scatterers are presented within homogeneous objects. The main disadvantage of this approach is its high computational cost and consumability. It is not suitable for high-resolution microwave imaging. To speed up this method, the runtime of forward solvers must be reduced or parallelisation must be used [10]. For example, the so-called 'supervised learning' algorithm for the detection and classification of brain stroke using the MWI method has been introduced and described in the study [26]. The use of GAs for brain stroke monitoring is presented, for example, in [27].

3.2 Main aim of the chapter

The aim of this chapter is to describe selected reconstruction methods in terms of problem statements and mathematical formulations. Also, algorithm implementation on considered diagnostic and monitoring applications, e.g. microwave-based brain stroke detection and non-invasive microwave thermometry, is demonstrated. The crucial algorithm parameter, the so-called truncation level, is defined and explained.

3.3 Problem statement and mathematical background

In the selected MWI medical applications explored in this thesis, namely the detection of brain stroke and non-invasive thermometry, the monitoring process necessitates periodic assessment at short time intervals. Differential microwave imaging (DMWI) is a method with such potential. It is imperative that both the algorithm and the imaging system should be 3D to enable the detection of potential hotspots across different planes of the imaging system.

In this regard, algorithms developed by the research group led by Prof. Bucci, Dr. Crocco, and Dr. Scapaticci [20], [28], [29], utilizing linear sampling method, Born approximation (BA) or Distorted Born approximation (DBA), along with various regularization schemes such as Truncated Singular Value Decomposition (TSVD) and Tikhonov regularization, have already been established.

Within these algorithms, the linear operator ($\mathbf{L}_e$) is built from numerically computed electric fields originating from each antenna of reference model, subsequently decomposed via TSVD to products *U*, *S* and *V*. This is called an **offline** phase and can be done in advance. Then in the **online** phase the measurements of the S-parameters of the scenarios in time t_0 and t_n and the evaluation of the object function based on the results of the measurements of the S parameters are executed. The mathematical details are described further in subchapter Mathematical formulation 3.3.1. The algorithm operation scheme is depicted in the flow chart in Figure 3.2.

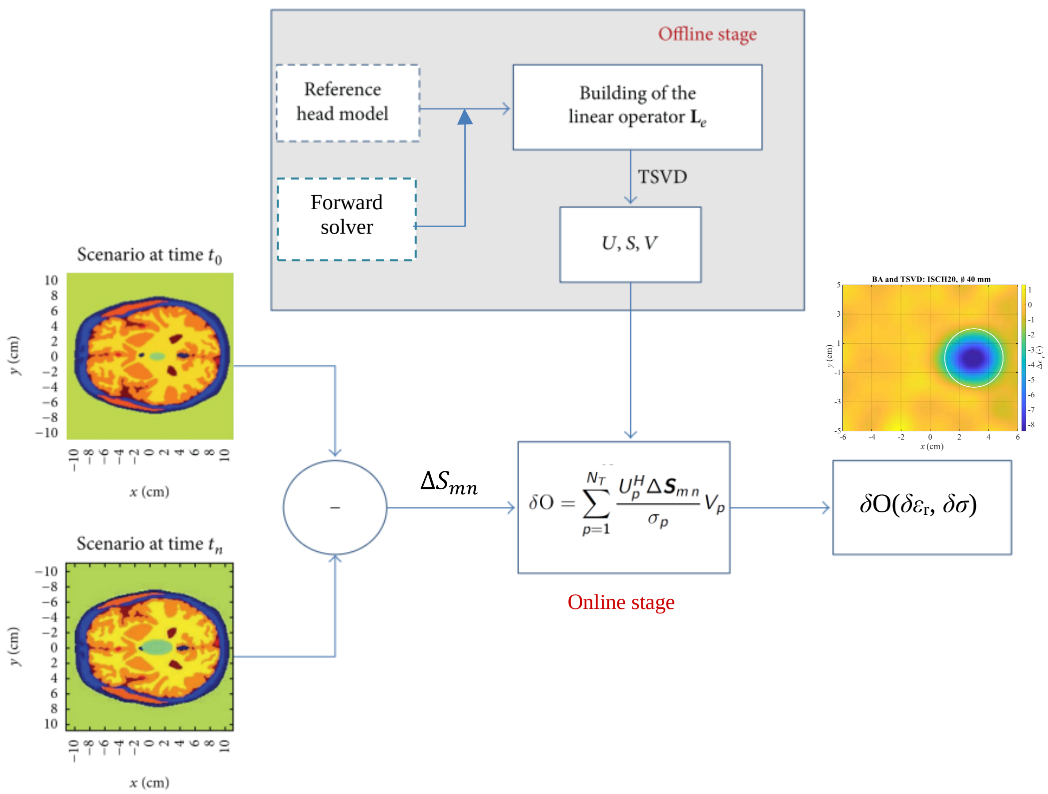

Figure 3.2 Flow chart of the algorithm for differential MWI of brain stroke. Adopted and edited from [28].

The algorithm was implemented for 3D problems and in order to prove its concept, the mathematical formulation [19] is defined in Subchapter 3.3.1. Some steps were adopted from [28], [29], [30].

3.3.1 Mathematical formulation

Let us consider multiview multistatic system with *N* number of transmitters *T* and *M* number of receivers *R* placed in observing domain Γ around the object to be imaged Ω as depicted in Figure 3.3. The number of *T*/*R* is often equal, i.e. *N* = *M;* for the sake of clarity, we preserve the distinction of these two in the following rows.

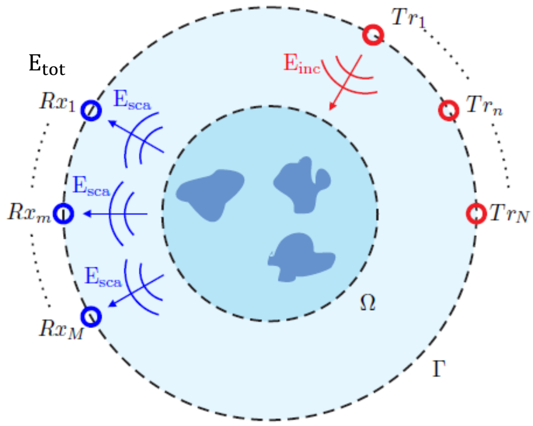

Figure 3.3 Multiview multistatic system, reprinted with permission of Prof. Jan Vrba Jr.

This general system can be described by Volume Integral Equation (VIE) defined e.g. in [19] and by equation (3.1) or (3.2), respectively,

$$\mathbf{E}_{\mathrm{tot}}(\mathbf{r}) = \mathbf{E}_{\mathrm{inc}}(\mathbf{r}) + \mathbf{E}_{\mathrm{sca}}(\mathbf{r}) \tag{3.1}$$

$$\mathbf{E}_{\mathrm{tot}}(\mathbf{r}) = \mathbf{E}_{\mathrm{inc}}(\mathbf{r}) + k_0^2 \int_{\Omega} \left(\bar{\mathbf{g}}(\mathbf{r},\mathbf{r}') \cdot \left(\mathrm{O}(\mathbf{r}')\mathbf{E}_{\mathrm{tot}}(\mathbf{r}') \right) \right) dV', \tag{3.2}$$

where $\mathbf{E}_{\mathrm{tot}}$, $\mathbf{E}_{\mathrm{inc}}$ and $\mathbf{E}_{\mathrm{sca}}$ are total, incident and scattered electric fields, k_0 is the lossless wave number in background medium and is equal to $k_0 = \omega\sqrt{\varepsilon_b \mu_0}$. The object function $\mathrm{O}(\mathbf{r}')$ is defined as reported for example in [30].

The principle of Born approximation is considering that object to be imaged is a so-called weak scatterer. Thus, the scattered electric field can be neglected, and the total electric field is directly equal to the initial electric field, which is typically obtained employing the FEM-based forward solver. Distorted Born approximation utilizes total electric fields.

For the case of differential imaging approach such as for instance a brain stroke follow-up or a non-invasive temperature monitoring, scattering parameters are measured at the time instance $t = t_0$ (before stroke/before thermotherapy) and at the time instance $t = t_1 \neq t_0$ (when stroke progresses/temperature elevates). The difference in S-parameters will be equal to differential S-matrix ΔS_{mn}

By sequencing mathematical operations, the so-called linear operator $\mathbf{L}_e$ is built from obtained initial electric field intensities as reported in [29]. Then linear equation (3.3)

$$\Delta S_{mn} = \mathbf{L}_e \delta O(\mathbf{r}), \tag{3.3}$$

where δO $(\delta\varepsilon_r, \delta\sigma)$ if differential object function, ΔS_{mn} is differential S-matrix. Number of pixels N_c of object function is usually higher than number of independent S-parameters (N+1) N/2. Thus, regularization has to be used. By TSVD (built-in function svd() in MATLAB®) linear operator $\mathbf{L}_e (N^2 \times N_c$ matrix) can be decomposed to $\mathbf{L}_e = \mathbf{USV}^H$. $\mathbf{U}$ is $N^2 \times N^2, \Delta S_{mn}$ is $N^2 \times N_c$ and $\mathbf{V}$ is $N_c \times N_c$.

The δO can be then expressed by equation (3.4) as

$$\delta O = \sum_{p=1}^{N_T} \frac{U_p^H \Delta S_{mn}}{\sigma_p} V_p, \tag{3.4}$$

where U_p is the n-th column of $\mathbf{U}, V_p$ is the n-th column of $\mathbf{V}^T$ and σ_p is the n-th diagonal element of $\mathbf{S}$ (singular value), N_T is the number of considered singular values in the TSVD, so-called truncation level [29].

Truncation level

The value of N_T should be equal at maximum to number of independent S-parameters inside the S-matrix which can be calculated as (N+1) N/2 where N is number of transmitters/receivers in MWI system. Taking into account some noise, the value is often lower and has to be determined individually or by tracking the changes in slope in the plotted curve of magnitude of singular values depending on its indices [31] as shown in Figure 3.4. It corresponds to a change in the singular functions involved in the image formation. The choice of truncation level involves the stability of the reconstruction and its accuracy. To achieve the finest details of images, the level should, in principle, be set to as highest number as possible. Nevertheless, the higher level of truncation, the lower magnitude (dB) of singular values, which is mostly affected by measurement noise or model errors.

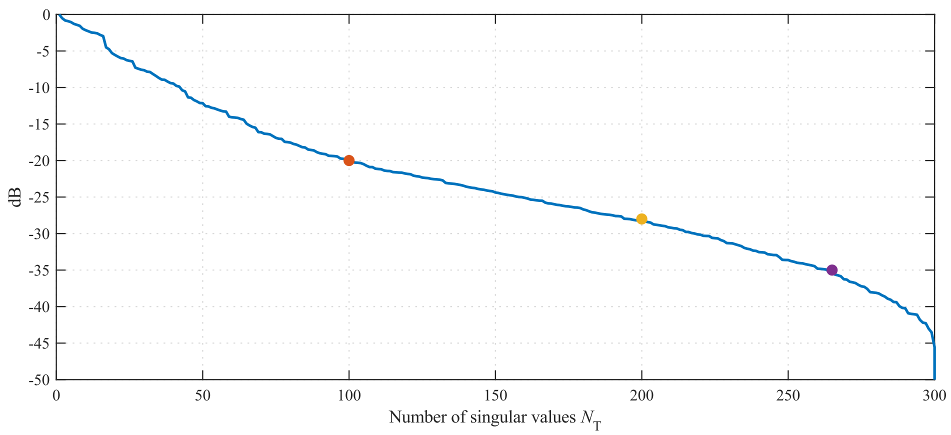

Figure 3.4 Magnitude of singular values (dB) of the discretized linear operator versus their indices for 24-port MWI system; the colour dots indicate the three main slope changes.

Implementation of reconstruction algorithm

These steps are divided to offline (can be done in advance before any measurements) and the online stage (periodically repeating during brain stroke or temperature monitoring) are also schematically depicted in Figure 3.2.

Offline stage includes

1. Modelling of MWI system (antenna array) and domain to be imaged, for example, phantom of human head or phantom of head and neck region with implemented frequency and temperature dependent dielectric properties.

2. Computing of initial/total electric fields $\mathbf{E}_{\mathrm{inc/tot}}$ as well as initial S-matrix $\mathrm{S}_{inc/tot}^{sim}$ using a full-wave numerical forward solver such as COMSOL Multiphysics. These parameters are obtained for the initial time $t = t_0$. Therefore, for the case of brain stroke detection, the phantom of a human head without any stroke is presented inside the MWI system. Or, e.g., neck phantom before initiating of thermotherapy.

3. Building of linear operator $\mathbf{L}_e$ from numerically obtained electric fields for each antenna combination of considered MWI system.

4. Performing of SVD and storing its outcomes.

Online stage includes

1. Measurement of S-parameters in time t_0 and then in defined time steps t_n to get differential S-matrix $\Delta S_{mn} = S_{mn}^{t_n} - S_{mn}^{t_0}$.

2. Import of outcomes of SVD and obtaining of differential object function δO defined by equation (3.3)

3. Separation of the differential object function to create image of differential relative permittivity and conductivity with qualitative as well as quantitative information about change of dielectric profile due to ischemic/haemorrhagic stroke appearance or temperature increase/decrease, respectively.

3.4 Chapter conclusion

This chapter summarized reconstruction algorithms suitable to use in microwave imaging diagnostic applications. Regarding the applications introduced in this thesis the suitable linear algorithm based on Born approximation (BA) and regularization scheme of TSVD was chosen and its mathematical formulation was described. The favourite parameters of algorithm such as high speed and robustness were optimal parameters for our applications.

4 CHAPTER: NUMERICAL STUDY OF EM WAVE PROPAGATION

This chapter is based on the following published papers.

[A12], [A9], [A7]

4.1 Introduction

Numerical parametric studies using full-wave electromagnetic simulations are an important part of the MWI system design. These are based on well-known numerical techniques, such as the finite element method (FEM) or finite differences in the time domain method (FDTD). To achieve the best possible MWI system performance, each of its parts must be properly designed, evaluated, and verified by experimental measurements. Due to the diverse dielectric properties of biological tissues in the human body, the propagation of electromagnetic waves is intricate, particularly within the layered structure of the human head, where waves scatter and attenuate rapidly.

Conducting measurements with MWI systems requires determining the degree of attenuation of electromagnetic waves through the human head or the amount of signal power transmitted from one side to the other. This can be achieved through the utilization of mentioned numerical solvers and realistic head models. Signal transmission is the crucial parameter concerning the dynamic range of commonly used microwave hardware components of MWI systems, such as a Vector Network Analyzer (VNA) or switching matrix. Another key feature that affects the transmission of microwave frequencies is the so-called matching medium, known also as coupling medium. Its placed between the transmitting/receiving antenna elements and investigated domain, e.g. model of human head, to ensure smooth transition of EM waves from antenna elements into the head. The last but not least parameter is used frequency band. According to [32] and [28], the most convenient frequency range is from 0,6 GHz to 1,5 GHz and 1 GHz can be considered as the most valuable single operation frequency for microwave brain stroke imaging.

4.2 Main aim of the chapter

We proposed several numerical studies focused on the identification of microwave signal attenuation at specified frequencies suitable for MWI. In the next step we verified the spatial and contrast resolution of the MWI method. Spatial resolution is theoretically defined by half of wavelength of planar EM wave inside the given medium of specified permittivity and at given frequency. In my opinion, it is the fundamental criterion which needs to be clarified prior to MWI system design.

4.3 EM wave propagation through human head models

We conducted a numerical study gradually transited from 1D analysis, through 2D analysis with artificial and realistic human head models and ended up with 3D simulations. The first 1D model was structured as a cross section of the human head with average thickness of each tissue (skin, skull, CSF, grey matter, and white matter) adopted from anatomical literature [33]. Based on the IT'IS Foundation database [34] the anatomical structure of realistic 2D and 3D models was created. All considered scenarios are shown in Figure 4.2. The dielectric properties of head tissues were obtained using the fourth-order Cole-Cole model and the parameters of the IT'IS database. Distilled water served as the coupling medium.

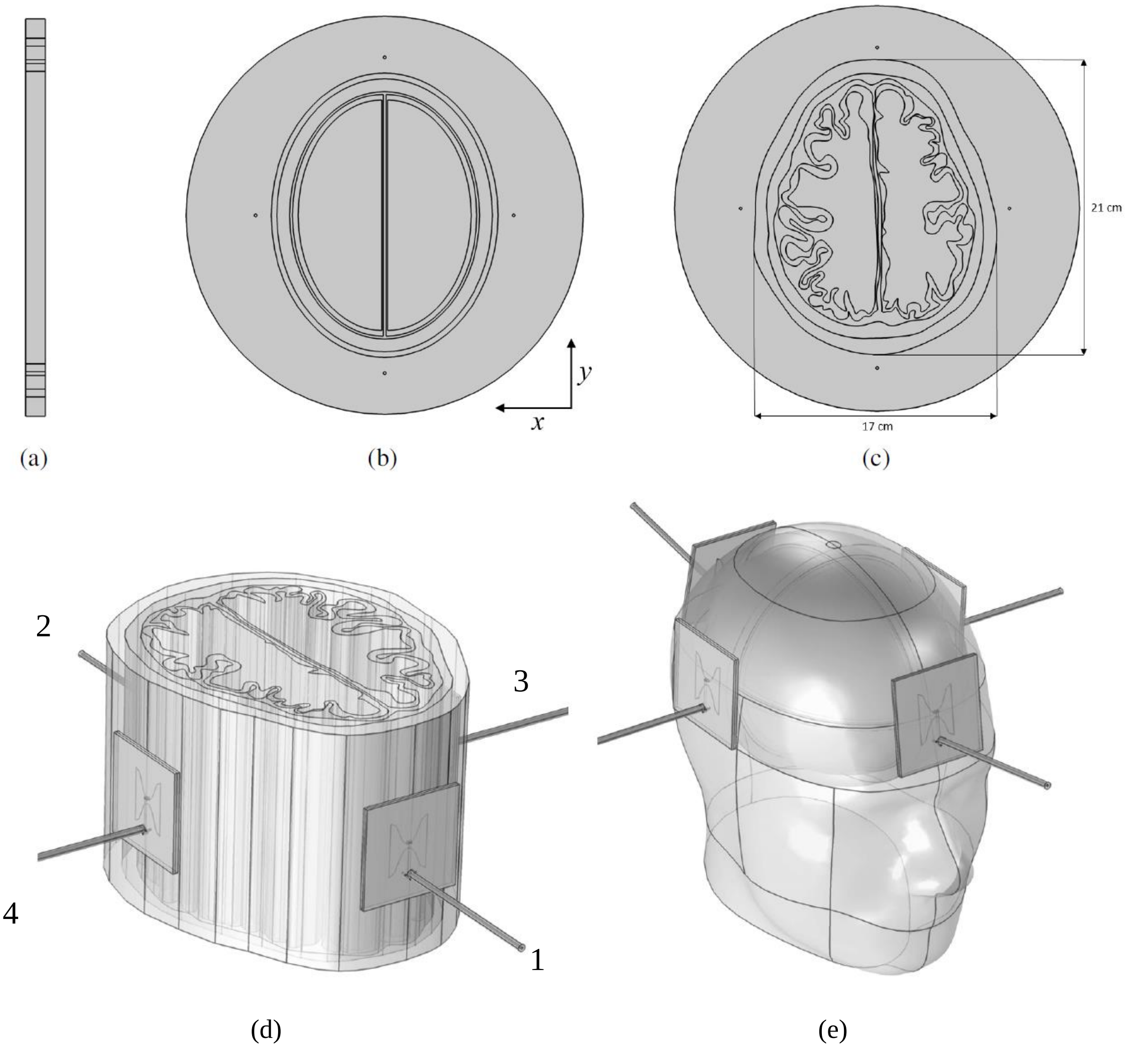

Figure 4.1 Models of human heads (a) 1D model where white matter in the middle of the model is surrounded by grey matter, CSF, skull, skin, and water bolus from both sides, (b) simplified 2D model of human head, and (c) realistic 2D slice of human head. In (d) realistic extruded slice of the human head and the so-called simplified 3D model and ellipsoids that represent the brain tissues (e).

The linear source of the EM wave and the point source were set in 1D or 2D models, respectively. In 3D models the slot antenna element designed in [35] was used to generate an electromagnetic field in the frequency range of 0,5 to 1,5 GHz. Previous studies [20] have shown that the frequency of 1 GHz is well suitable for MWI medical brain imaging as a good compromise between penetration depth of the EM wave and spatial resolution.

In 2D models, different distances *d* (mm) of EM wave sources in relation to head phantoms and different conductivities of the water bolus (0,005 S/m and 1 S/m) were tested. The modules of *S*-parameters in vertical and horizontal directions (*y* and *x*-axis) described as transmission coefficients S_{21} and S_{43} depend on frequency were observed and are shown in Figure 4.2.

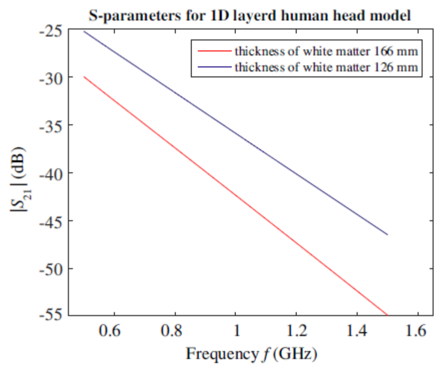

(a)

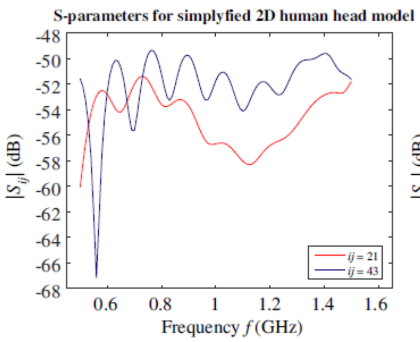

(b)

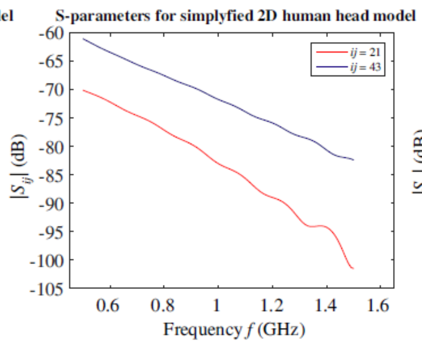

(c)

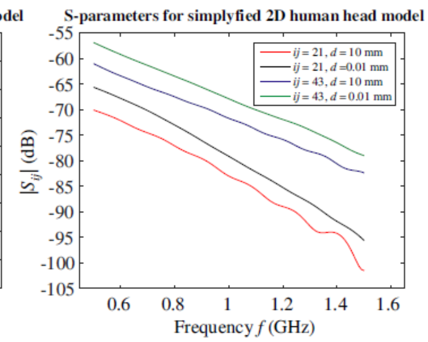

(d)

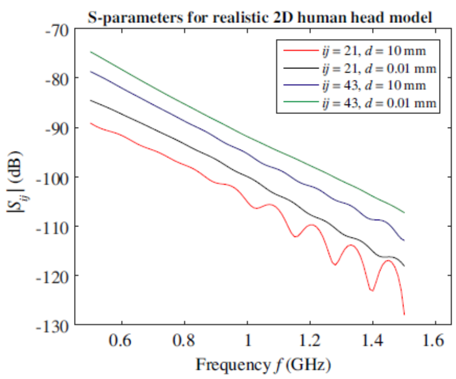

(e)

Figure 4.2 Continued.

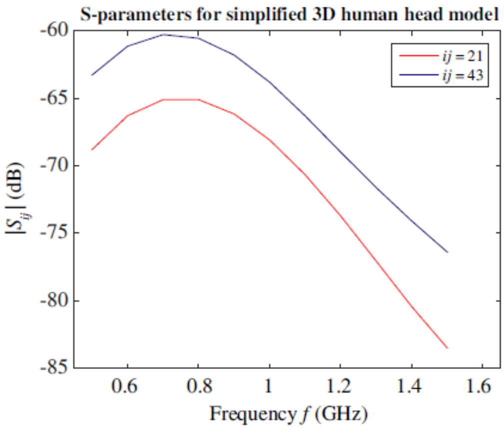

(f)

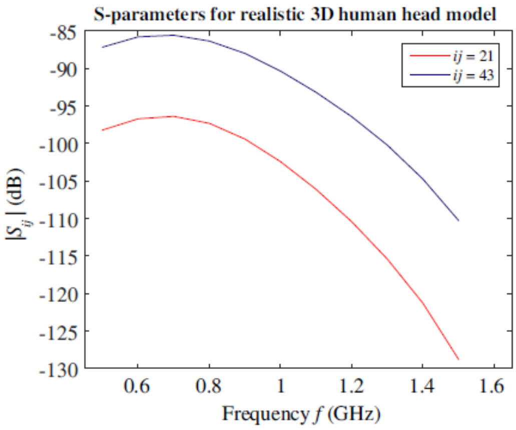

(g)

Figure 4.2 Modules of the *S*-parameters for different human head models and different scenarios. In (b), (c), different conductivities of water bolus (0,005 S/m and 1 S/m) were applied. In (d) various distances of the EM wave source from head models. All remaining scenarios were computed with conductivity of the water bolus 1 S/m.

Another numerical study focused on effect of different matching mediums to transmission coefficients and mutual antennas coupling was performed. On the simplified model of MWI system with 4 slot antennas and cylindrical layered phantom inside, we demonstrated the importance of lossy matching medium – salt water with conductivity of 1 S/m compared to distilled water with conductivity of 0,005 S/m. The values of the transmission coefficient corelated with the previous analysis and the additional distribution of the E field intensity around the antennas and inside the MWI system were explored.

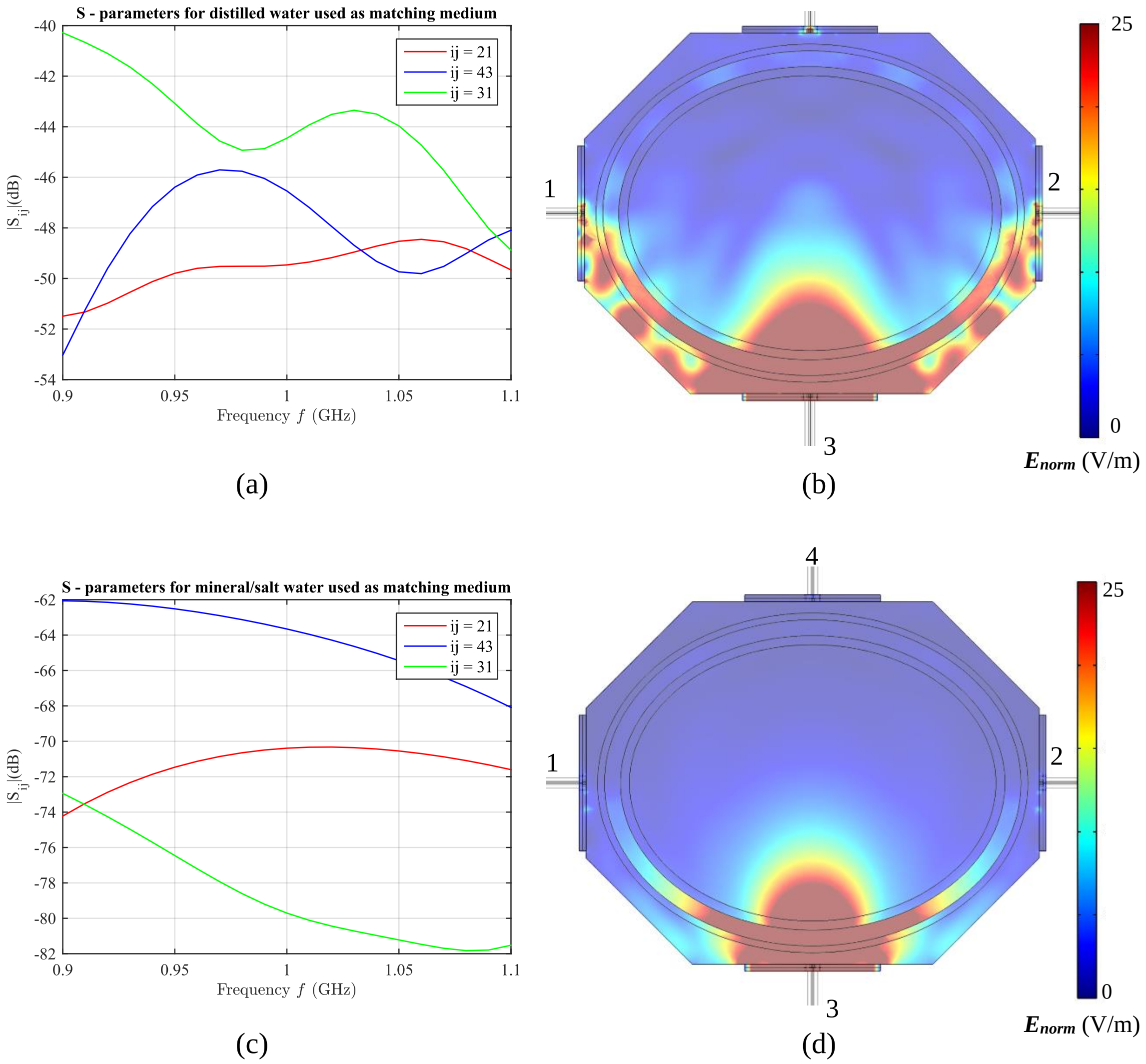

Figure 4.3 Modules of the *S*-parameters for different matching mediums (distilled and salt water) and mutual antenna position (a),(c). The module of normalized E field intensity in the range of 0 – 25 V/m with a step of 5 V/m.

4.4 Spatial and contrast resolution of the MWI technique

The goal of the following numerical trial was to evaluate the spatial and contrast resolution of the MWI technique. A model of 2D MWI system adopted from [25] consists of 10 slot antennas positioned equidistantly in one plane around homogenous brain phantom was implemented inside COMSOL Multiphysics. To determine the spatial resolution, cylindrical inclusions (stroke phantoms) of different diameters 10, 20 and 40 mm were positioned to specified coordinates inside the system as shown in Figure 4.4. The dielectric properties of inclusions were virtually created with respect to the properties of brain phantom as increase as well as decrease by approx. 10, 20 and 40 % as summarized in Table 4.1. This mimics the change of dielectric contrast inside the brain during haemorrhagic – HEM (increase) and ischemic – ICHS (decrease) stroke attack [36].

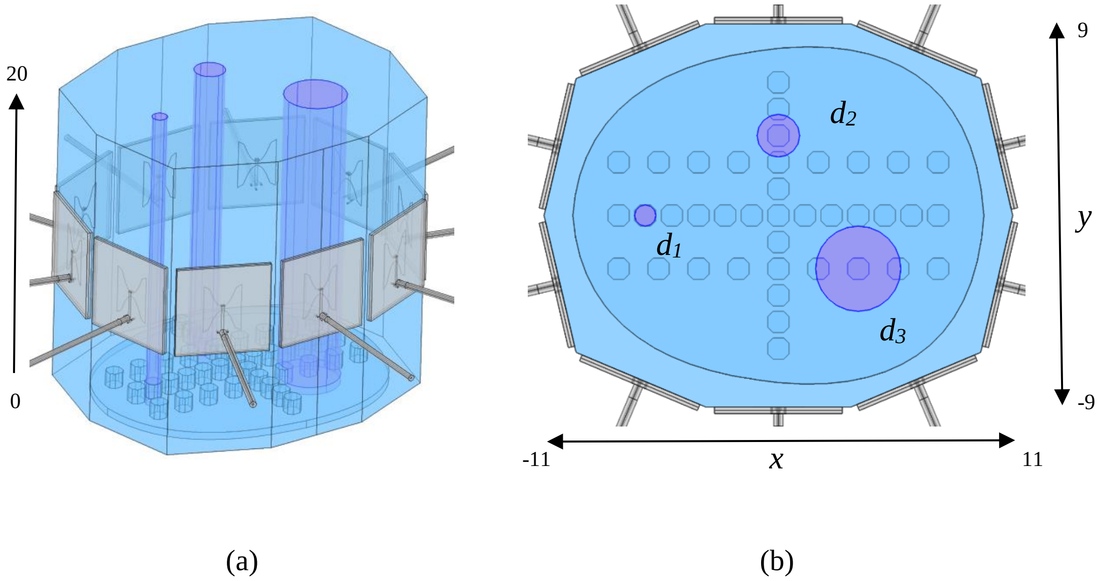

Figure 4.4 Numerical model of the 2D MWI system with 10 slot antennas and cylindrical inclusions.

Table 4.1 Dielectric properties, relative permittivity ε_r and conductivity σ of inclusions and difference of each and the brain phantom.

	Brain	**HEM1**	**HEM2**	**HEM3**	**ISCH1**	**ISCH2**	**ISCH3**
$\boldsymbol{\varepsilon_r}$ **(-)**	41,8	46,0	50,0	57,6	38,0	33,0	25,0
$\boldsymbol{\sigma}$ $(\mathbf{S \cdot m^{-1}})$	0,97	1,07	1,2	1,4	0,87	0,77	0,6
$\boldsymbol{\delta\varepsilon_r}$ **(-)**		$+4$	$+8$	$+15$	-4	-9	-16
$\boldsymbol{\delta\sigma}$ $(\mathbf{S \cdot m^{-1}})$		$+0{,}1$	$+0{,}2$	$+0{,}4$	$-0{,}1$	$-0{,}2$	$-0{,}4$

The numerically obtained data were processed by a reconstruction algorithm based on the so-called differential microwave imaging approach described in Chapter 3. The method of simplified Born approximation (BA) and regularization by TVSD (Truncated Singular Value Decomposition) were employed. The acquired images present a change of local complex permittivity known as object function separated to relative permittivity and conductivity.

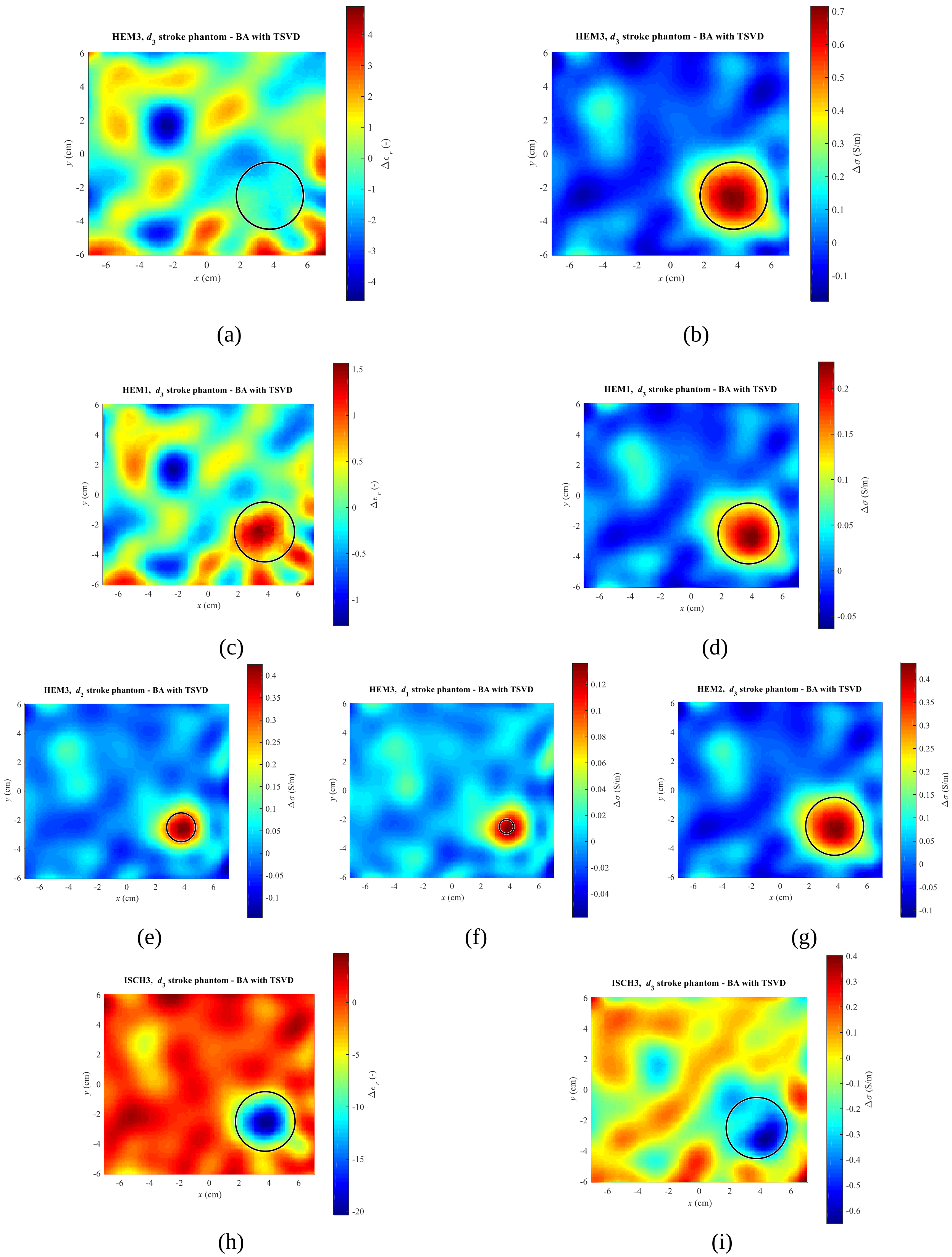

Figure 4.5 Continued.

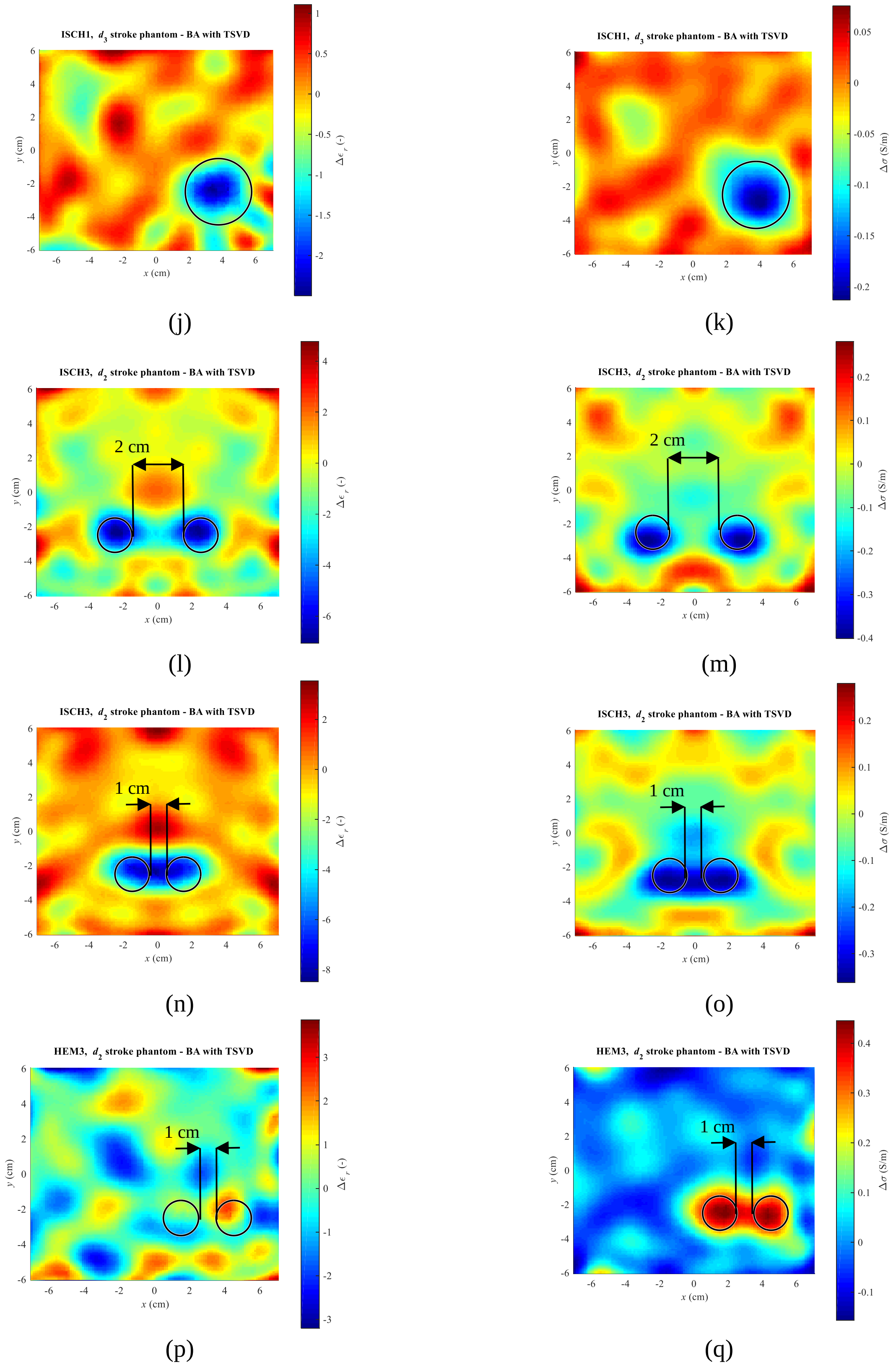

Figure 4.5 Reconstructed distribution of differential dielectric properties based on numerical synthetic data. The black circles mark the actual position of inclusion. The cut plane in the z-axis equal to 10 cm is presented.

4.5 Chapter conclusion

In this chapter, some results of conducted numerical studies focused on EM wave propagation through human head models, role of matching medium as well as spatial and contrast resolution ability of MWI method were introduced. Trends of transmission coefficients confirmed values at minimum approx. –100 dB in the frequency band around 1 GHz depending on the complexity of used head models, the matching medium and the distance of antennas from the models. These values match the parameters of frequently used hardware in MWI system, such as the switching matrix and VNA. Its dynamic range reaches typically up to 140 or 120 dB depending on the type of VNA, respectively. The analysis of lossy and lossless matching mediums (distilled/salt water) showed that transmission coefficients for distilled water got distorted due to mutual antenna coupling (Figure 4.2 (b)). The surface EM wave travels around the head model and not mainly through the head model. This fact was also confirmed by the second numerical study presented in Figure 4.3 where the distribution of the E field intensity is shown. In all cases values of transmission coefficient can be considered as minimum possible also due to the fact that the used slot antenna was not impedance matched for the given medium (water). The realistic complex geometry of the human brain plays a key aspect when the transmission coefficient decreases about – 30 dB compared to the simplified model. The data provided valuable information for future experimental measurements which will be presented further. Last numerical analysis validated spatial and contrast resolution of MWI technique on 10-port 2D MWI system. Various contrasts in dielectric properties of brain phantom and stroke phantoms were simulated, as well as different stroke phantom diameters. The suggested and implemented reconstruction routine based on the differential MWI approach proved good sensitivity to detect changes in dielectric properties, as shown in Figure 4.5. The reconstructed difference was always higher (relatively 20 – 50 %) than the simulated. It could be caused by the principle of Bron approximation (BA), which will be described in future chapters. The contrast resolution of the MWI technique is mainly based on the used reconstruction method. Regarding the spatial resolution, the numerical simulations confirmed the theoretical assumption of **half of wavelength** in medium of given relative permittivity. For brain phantom it reached approx. **2 cm**. Two inclusions at a distance of 2 cm were successfully reconstructed separately. However, after bringing two inclusions closer to 1 cm, the differentiation failed due to limitation of spatial resolution.

5 CHAPTER: DESIGN OF ANTENNA ELEMENTS AND MWI SYSTEMS

This chapter is based on following published papers.

[A1], [A2], [A8], [A5], [A6]

5.1 Introduction

5.1.1 Antenna elements

Since the human body can be considered as high permittivity and lossy medium, the design of antenna elements (AEs) differs rapidly from that for free-space operation. The MWI method is based on non-invasive measurements of dielectric properties of tissues. The contrast of dielectric parameters or the contrast between healthy and any pathological tissue, respectively, causes reflections of EW waves. A very good impedance matching between antennas and investigation domain must be achieved to detect scattered or transmitted signals.

A key parameter in antenna design is the so-called reflection coefficient S_{11} (dB). The goal is to reach values of magnitude of the reflection coefficient below -10 dB, which is equal to the fact that only 10 % of the power transmitted by the antenna through its feeding port is reflected to the generator.

Several types and shapes of AEs for microwave-based applications have been previously investigated. In principle, a distinction can be made between antennas implemented using waveguide technology and those implemented using printed circuit board (PCB) technology. Waveguided antennas have proven to have higher potential in microwave hyperthermia treatment than in MWI applications [37].

PCB antennas are more commonly used in the field of microwave-based head imaging. A detailed description of PCB antennas is summarised in [38].

Richly used antennas for microwave brain stroke monitoring are dipole antennas, most commonly the bow-tie antenna. This type of antenna was presented, for example in [39]. The great advantage of this antenna is its simplicity. The bow tie antenna could be relatively easily designed using a parametric numerical study. Another group of frequently used antennas are patch or microstrip antennas, respectively. Unlike dipole antennas, which are the most commonly fed directly by the SMA port (symmetric feeding must be guaranteed, for example, by balun), the patch antennas use a microstrip transmission line for its feeding as presented for example in [40]. The triangular patch antenna for brain stroke monitoring was designed by Trefna [41], where cutting a hole in the patch enhanced the bandwidth of the antenna [42]. In a study [43] a dipole semicircular patch antenna was presented to locate an object in a homogeneous medium.

Antenna elements are mostly designed with respect to the fact that a perfect contact between the antenna and the investigating domain is provided or the matching medium is used, respectively. A different approach was introduced in the study of [44]. A slim wideband antenna was designed to overcome the strong reflection of the air-sample interface. A great promise for the future can provide textile-based antenna elements, as presented in [45] and [46].

Several slot-loaded folded directional dipole UWB antennas were introduced by Mobashsher et al. [47]. The main goal of these studies was to design compact and lightweight antennas suitable for use in MWI systems. To reach a unidirectional operation of antennas, a ground plane was required, which however increased the weight of proposed antennas. Therefore, miniaturisation of antennas was very challenging to respect the requirements of the MWI system, while unidirectional radiation and impedance matching had to be preserved.

In the study [25], [35] a slot double layer antenna element was shown to be a promising antenna type for MWI of brain stroke. This antenna was designed and fabricated on the inspiration of [16]. Here, a one-layer slot antenna with a distorted bowtie slot shape was presented. The microstrip line feeding on the top side of the substrate and a slotted bowtie ground plane on the bottom side were used.

A newly designed double-layer slot antenna adopted the shape of the slot, but a new type of feeding by transmission line placed between two substrates was used. Thanks to it, a symmetrical feeding was obtained, and no balun had to be used. Also, the unidirectional radiating to the investigating domain was reached thanks to the ground plane.

In our opinion, the paradigm of antenna design for microwave-based head imaging must focus on the following antenna parameters:

(a) Choice of **optimal antenna bandwidth** regarding the trade-off between penetration depth of EM waves in the imaged area and spatial resolution, respectively. The study [28] showed that multi-frequency data (wideband) would not significantly improve the achievable results. Also, the narrow frequency band allows us to avoid the problem of modelling the frequency-dependent dielectric parameters of tissues and preserves low complexity of experimental setups, which rapidly speeds up data acquisition and processing.

(b) **Compactness** of antennas. Due to the fact that MWI systems should be portable, and several tens of antenna elements need to be placed on relatively small surface.

(c) **Antenna radiation and directivity**. One of the weak points of the MWI systems is the distortion of a useful signal by reflections of surrounding objects/people, RF devices, or mutual multipath crosstalk of antennas [48]. To avoid or reduce it, unidirectional antennas with suppressed backward radiation are desirable. Moreover, the symmetrical feeding ensures the elimination of backward current flow through antenna port back to generator, and thus directive antenna radiation can be obtained.

5.1.2 MWI systems for brain stroke detection/classification

Several research groups and start-ups all around the world deals with development of devices for early brain stroke detection and classification utilizing microwave imaging/tomography. Basically, the two approaches can be distinguished. First is focused on quantitative evaluation of dielectric properties distribution inside the brain and thus estimating the type, localization and size of stroke. Typically, this approach requires a priori information about scanning region, e.g. geometry, and is computationally costly. The second approach exploits machine learning algorithms to classify the type of stroke without any information about its position or size. Its advantage is rapid diagnosis, but the large set of training data needs to be addressed.

The first research group, led by **Prof. Semenov** in Vienna, Austria, focuses on developing microwave head-imaging systems (**BrainScanner EMTensor**©) able to reconstruct complete map of dielectric parameters distribution inside the brain. Already, three generations were introduced. The first generation advanced the technology from virtual brain imaging to imaging the normal human brain in volunteer studies, as detailed described in [49], [50], [51]. The first-generation system featured 160 ceramic-loaded waveguide antennas arranged in 5 rings with 32 antennas each and operated at 0.9-1.1 GHz. The imaging chamber, filled with a matching medium, utilized a nonlinear inversion solver, an iterative algorithm based on gradient inversion and Tikhonov regularization. Measurements required capturing an "empty" field (with matching medium only) and a "full" field (with the object). In the second generation, the number of antennas increased to 177 and in the third to 192. Clinical trials were conducted in Vienna and Linz, including testing stroke detection on a human phantom. In [52] it is reported that a reconstruction time is around 2 minutes using a parallel high-performance computer cluster with 4,096 cores for a 2-D image.

Another research group focused on MWI system design is led by **Prof. Amin Abbosh** at the University of Queensland, Brisbane, Australia. Their work mainly involves developing radar-based MWI systems and delay-and-sum reconstruction algorithms. The initial versions employed a single UWB antenna rotating around a head phantom [53], [54], [55]. The latest prototype uses 16 fixed antennas, operating at 1-2.4 GHz, which can be placed on a human head or phantom without the need of a matching medium [56]. The system was verified on realistic head phantom prepared using 3D printed molds and tissue-equivalent mixtures [57]. The similarities between the imaging of realistic head phantoms and the actual heads of volunteer were demonstrated. The study [58] also confirms the consistency of the imaging results across different sizes and shapes of the head.

The **Strokefinder MD100,** developed by the research group around **Prof. Mikael Persson** and Prof. Andreas Fhager (Medfield Diagnostics, Göteborg, Sweden), is the first portable microwave device for the classification of brain stroke [59]. It features eight antennas encased in gel-filled plastic bags to enhance signal coupling. The adjustable antennas ensure a perfect fit for different head shapes. The battery-powered device weighs approximately 6 kg, and each measurement takes around 3 minutes. In a clinical study with 20 patients having subdural haematoma, the MD100 demonstrated a classification accuracy with 100% sensitivity and 75% specificity compared to healthy subjects. Today, the next stage of clinical trial is ongoing in Australia. The Strokefinder is equipped inside the ambulances to provide scan and stroke classification during transport to the hospital.

Last but not least, the cooperation between the research group of **Prof. Francesca Vipiana** (Trento, Italy) and **Prof. Lorenzo Crocco** (National Research Council of Italy) brought a first prototype of a microwave imaging system dedicated to monitor brain stroke progression in the post-acute phase [31], [60], [61]. The developed helmet with 24 PCB-printed monopole antennas inside dielectric bricks operates at 0.8–1.2 GHz. Preliminary experiments and numerical analyses confirmed the system's ability to image strokes of approximately 1 cm in size inside the homogeneous liquid head phantom. The differential microwave imaging approach using the Born approximation reconstruction algorithm with regularization scheme by truncated singular value decomposition (TSVD) were employed. The second stage of experimental validation on human-like 3-D phantoms with the brain made of *ex-vivo* calf brains identified some crucial points, such as setting of optimal threshold for singular values or hardware limitations.

All mentioned MWI experimental setups and prototype devices fully proved the concept of brain stroke detection/classification. Quantitative as well as qualitative approaches with different antenna types and numbers, reconstruction methods, and testing scenarios were introduced. It is always **around 1GHz**. It proves that this centre frequency is the most suitable as a trade-off between penetration depth and spatial resolution.

5.2 Main aim of the chapter

The main aim of the chapter is to develop a new antenna element suitable for use in a new multichannel MWI system dedicated to the detection of brain stroke. Next, validate this MWI system in laboratory experiment to qualitatively and quantitatively evaluate its capability to detect stroke phantoms inside homogeneous head phantom. To reach this main goal, some subtasks were determined.

(i) Numerical analysis of different antenna types in terms of antenna sensitivity on dielectric contrast and inhomogeneity size.

(ii) Proposition of the method for the assessment of antenna near-field radiation

(iii) Development of a new compact antenna element on the basis of conducted numerical analysis and its experimental verification.

(iv) Design and methodical validation of multichannel MWI system on geometrically realistic homogeneous head phantom.

(v) Qualitative and quantitative evaluation of retrieved images.

5.3 Bow tie antenna and prototype of MWI system

In our initial experimental setup (2018) dedicated for testing of brain stroke detection we used 8 bow tie antennas (Figure 5.1) equidistantly positioned in one plane inside the 3D printed octagonal container as depicted in Figure 5.2. The cylindrical inclusion mimics in terms of dielectric properties hemorrhagic (HEM) as well ischemic (ISCH) stroke phantoms were positioned at different locations inside the liquid brain phantom. All phantoms were prepared from mixture of Isopropyl alcohol, salt and water.

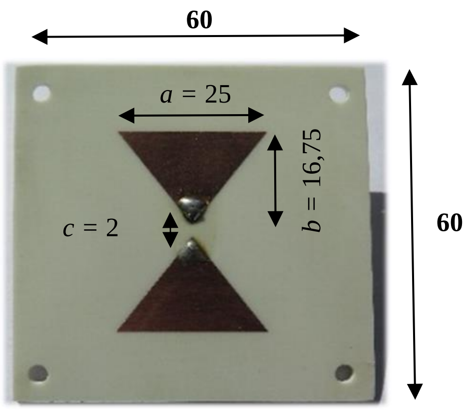

(a)

(b)

Figure 5.1 Manufactured bow tie antenna (mm), front view (a) and back view with SMA port (b).

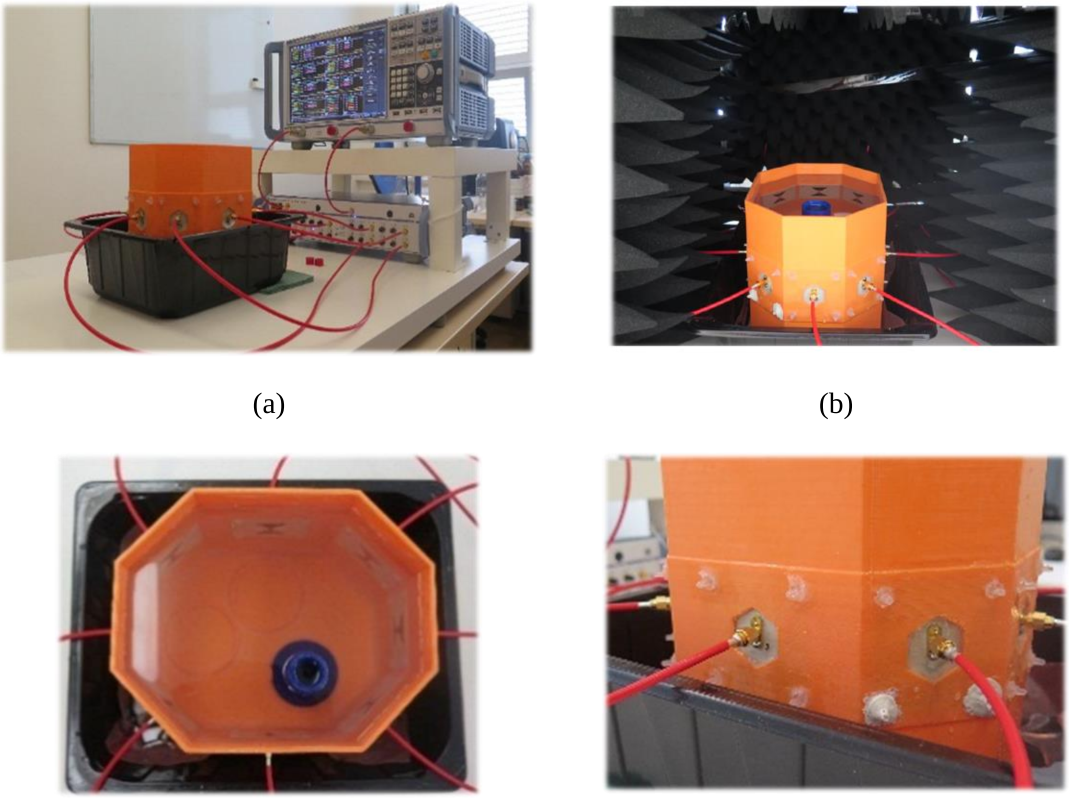

(a) (b)

(c) (d)

Figure 5.2 Experimental setup of MWI system with 8 bow tie antennas. (a) VNA R&S® ZNB 8, switching matrix R&S® ZN-Z84 (both Rohde&Schwarz GmbH, Germany) and MWI system, (b) absorbers placed around setup, (c) top view on the stroke phantom placed inside the liquid brain phantom and (c) detail on connected SMA ports of MWI system.

The measured S-matrices were processed using the already mentioned differential MWI algorithm based on Born approximation and regularization by TSVD as detailed explained in Chapter 3. The comparison of measured and reconstructed differential dielectric properties, relative permittivity, and conductivity are summarized in Table 5.1. The successful reconstructions are shown in Figure 5.3.

Table 5.1 Comparison of measured changes in dielectric parameters δ and reconstructed changes, green colour marks successful reconstruction, and N/A marks that it was not possible to determine which type of stroke phantom was placed in the MWI system. Relative error err (%) was calculated.

	Hem1	**Hem2**	**ISCH1**	**ISCH2**	**ISCH3**
$\boldsymbol{\delta\varepsilon_r}$ **(-)**	8	15	**-16**	**-21**	**-9**
$\boldsymbol{\delta\sigma}$ **(S/m)**	0,3	**0,6**	-0,1	-0,2	-0,1
$\boldsymbol{\Delta\varepsilon_r}$ **(-)**	N/A	N/A	**-11**	**-15**	**-10**
$\boldsymbol{\Delta\sigma}$ **(S/m)**	N/A	**0,5**	N/A	N/A	N/A
err (%)		**16**	**31**	**29**	**11**

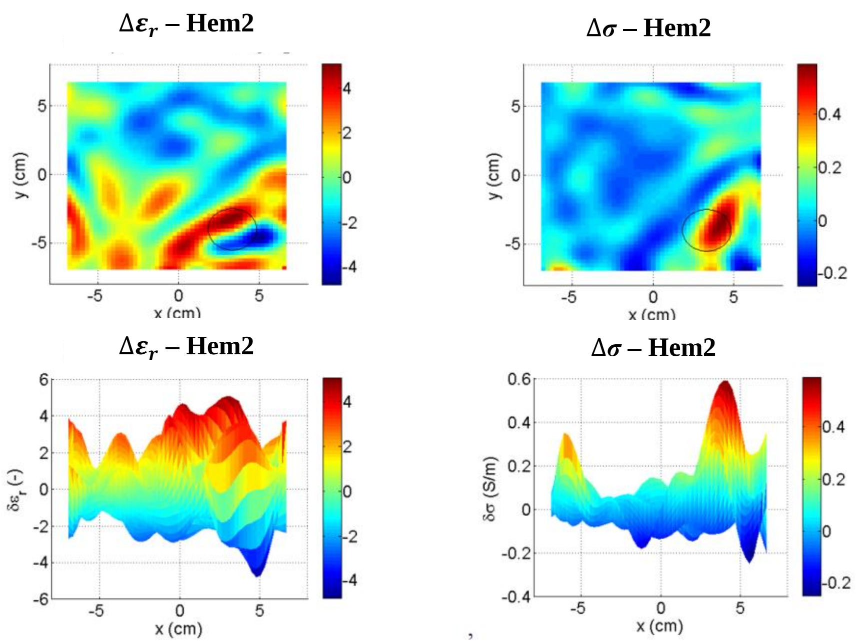

(a) (b)

Figure 5.3 Continued.

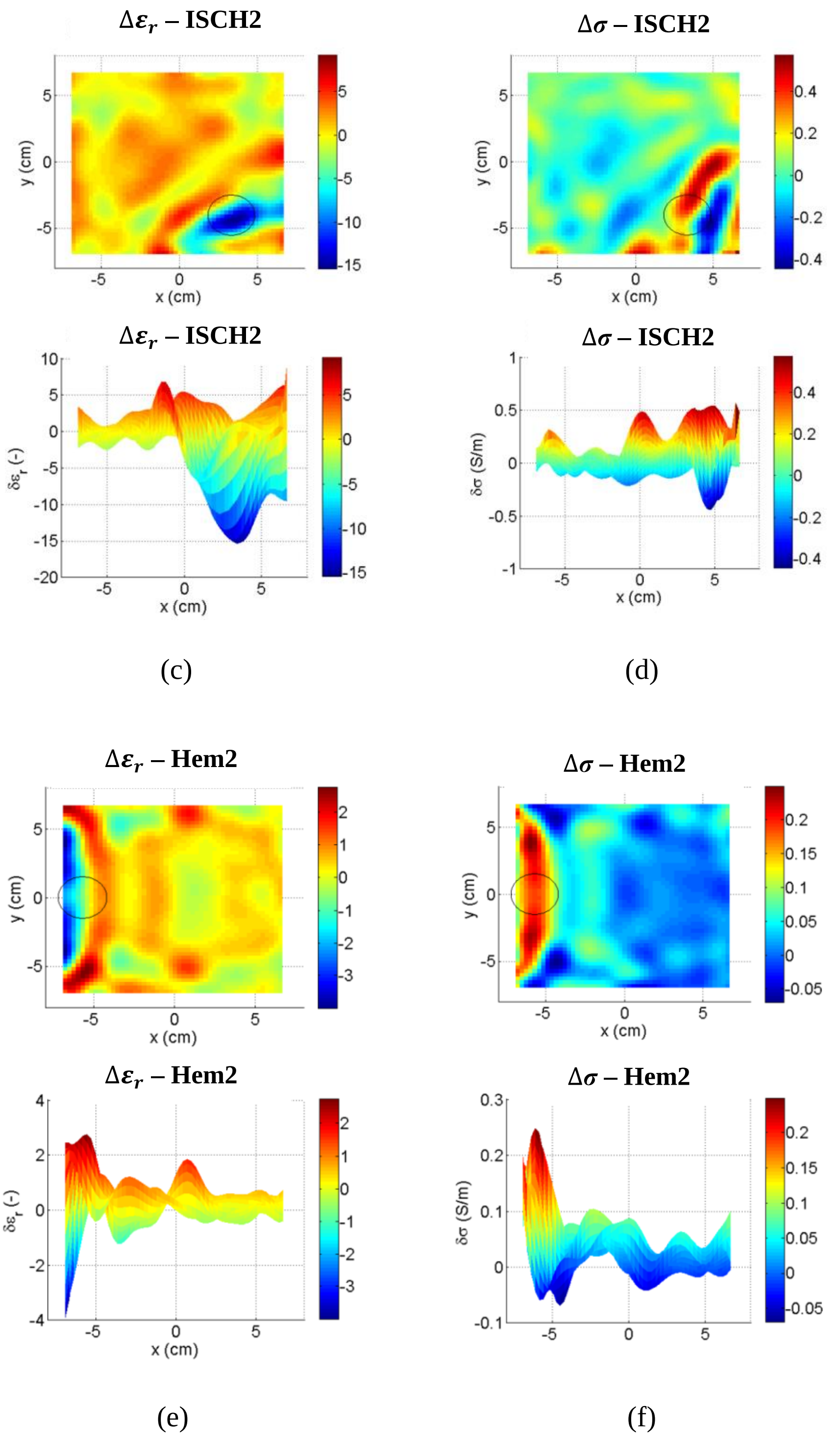

Figure 5.3 Reconstructed change in relative permittivity $\Delta\varepsilon_r$ (left) and electrical conductivity $\Delta\sigma$ (right) for stroke phantoms of one diameter and two positions. HEM2 (a) and (b), ISCH2 (c) and (d), and for HEM2 second position (e) and (f). The black circle marks the actual position of the stroke phantom.

5.4 Numerical analysis of various antenna elements

In the first step, we analysed by means of numerical simulations three standard antenna elements, i.e. a bow tie, slot, and rectangular waveguide-based antenna. Specifically, three different numerical analyses were carried out: (1) AEs sensitivity to stroke phantom type or dielectric properties change, respectively; (2) AEs sensitivity on stroke phantom diameter; and also (3) the antenna's ability to radiate dominantly only to the investigation front domain (i.e. antennas directivity) and antennas immunity against plane wave exposure (simulation of electromagnetic interference - EMI) were studied.

Two existing planar PCB antennas, i.e. bow tie (chapter 5.3) and slot [25] and purposely designed waveguide-based antenna for this study, were analysed. Both planar antennas were designed for an operating frequency of 1 GHz (average brain phantom) on a 60 x 60 mm Rogers R04003C RF substrate with a thickness of 1.5 mm (for slot antenna the two substrates were used). The antennas were fed by 50Ω coaxial line and panel SMA connector as shown in Figure 5.4. The rectangular waveguide-based antenna element was designed to operate in the TE_{10} mode based on analytical equations adopted from [62]. Deionized water (ε_r ~ 78 and σ ~ 0.2 S/m for 1 GHz and 22 °C [63]) was used to filled the inner space of the antenna to reduce waveguide dimensions. A numerical parametric study in COMSOL Multiphysics was carried out to determine the value of parameter *e* and *d*. A water bolus with a width of 1 cm was placed between the head phantom and the aperture of the waveguide element to ensure the proper coupling of the EM wave. The dimensions of the designed waveguide antenna together with its specifications are summarized in Table 5.2 and its image and reflection coefficient are shown in Figure 5.5.

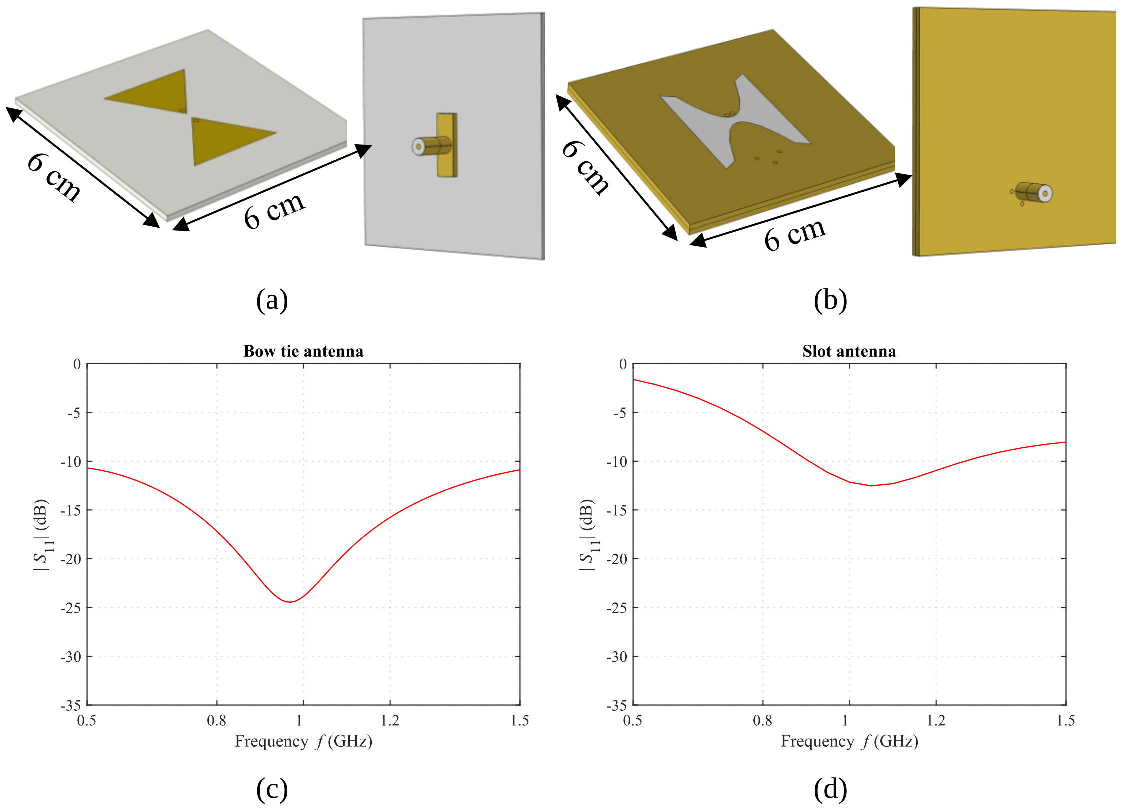

Figure 5.4 Models of considered antenna elements and feeding structure, bow tie antenna (a) and slot antenna (b). The metal parts are coloured yellow, while the RF substrate and teflon are grey. The reflection coefficients of the antennas are shown in (c) and (d).

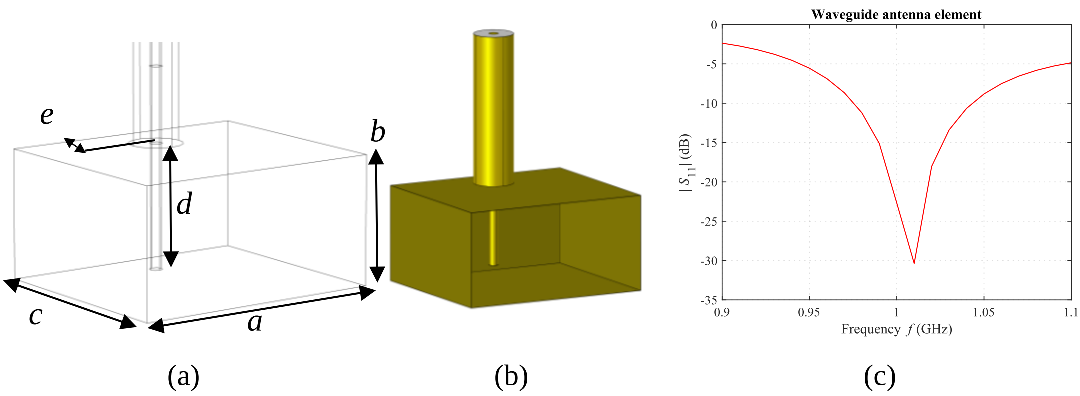

Figure 5.5 The model of designed waveguide-based antenna element with its parameters (a), yellow-marked metal parts, grey-marked teflon (b) and its reflection coefficient (c).

Table 5.2 Dimensions of the designed waveguide-based antenna element and its specifications. f_c (MHz) is the cut-off frequency and λ_g (mm) is the guided wavelength inside water-filled waveguide.

Dimensions (mm)	*a*	25.50
	b	12.75
	c	22
	d	10.95
	e	5
f_c (MHz)	666	
λ_g (mm)	45	

5.4.1 Antenna's sensitivity to contrast of dielectric properties

We compared the sensitivity of transmission coefficients to the contrast of the dielectric properties of the antennas introduced above. A simplified rectangular model/phantom of a human head with respect to real dimensions of a human head on the *x*-axis = 16 cm, the *y*-axis = 20 cm, and the *z*-axis = 16 cm was modelled in COMSOL Multiphysics. The dimensions of the model were adopted from MRI scans originating from IT´IS database [64]. In the middle of the head phantom, a spherical stroke phantom of different dielectric parameters with a diameter of d_2 = 20 mm was placed virtually. This diameter was chosen with respect to the theoretical λ/2 spatial resolution limit of the MWI method (i.e. diffraction limit [8]) inside the head phantom of the relative permittivity of 41.8 at frequency 1 GHz.

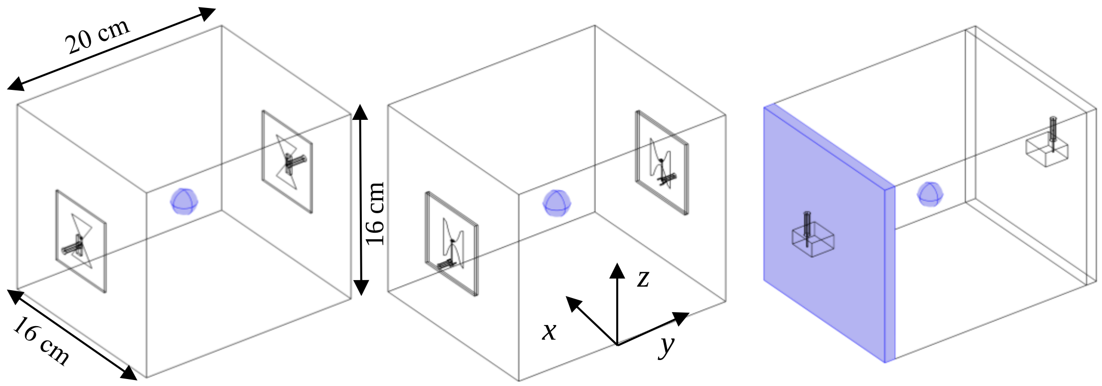

(a) (b) (c)

Figure 5.6 The numerical models for the evaluation of the sensitivity of the transmission coefficient to the change of the dielectric parameters of the stroke phantom and its diameter. Bow tie (a), slot (b) and rectangular waveguide-based antenna (c) where *x* = 16 cm, y = 20 cm and z = 16 cm. The stroke phantom and the water bolus are marked in blue.

The dielectric parameters of stroke phantom were increased (HEM - haemorrhagic stroke) as well as decreased (ISCH - ischemic stroke) by approx. 20 % compared to the dielectric parameters of the head phantom, as summarized in Table 5.3. The magnitudes and phases of transmission coefficients for the scenario without stroke phantom inside the head phantom and with a HEM/ISCH stroke phantom of diameter 20 mm for each of considered antennas were computed and are plotted in Figure 5.7. The absolute differences Δ of the magnitude and phase of the transmission coefficients for each antenna are shown in Figure 5.8. The simulations were computed for a single frequency of 1 GHz.

Table 5.3 Dielectric parameters of head phantom and HEM and ISCH stroke phantoms which were calculated as 20% increase/decrease of dielectric parameters of the head phantom.

	Head phantom	**HEM phantom**	**ISCH phantom**
ε_r **(-)**	41.8	50.16	33.44
σ **(S/m)**	0.97	1.16	0.77

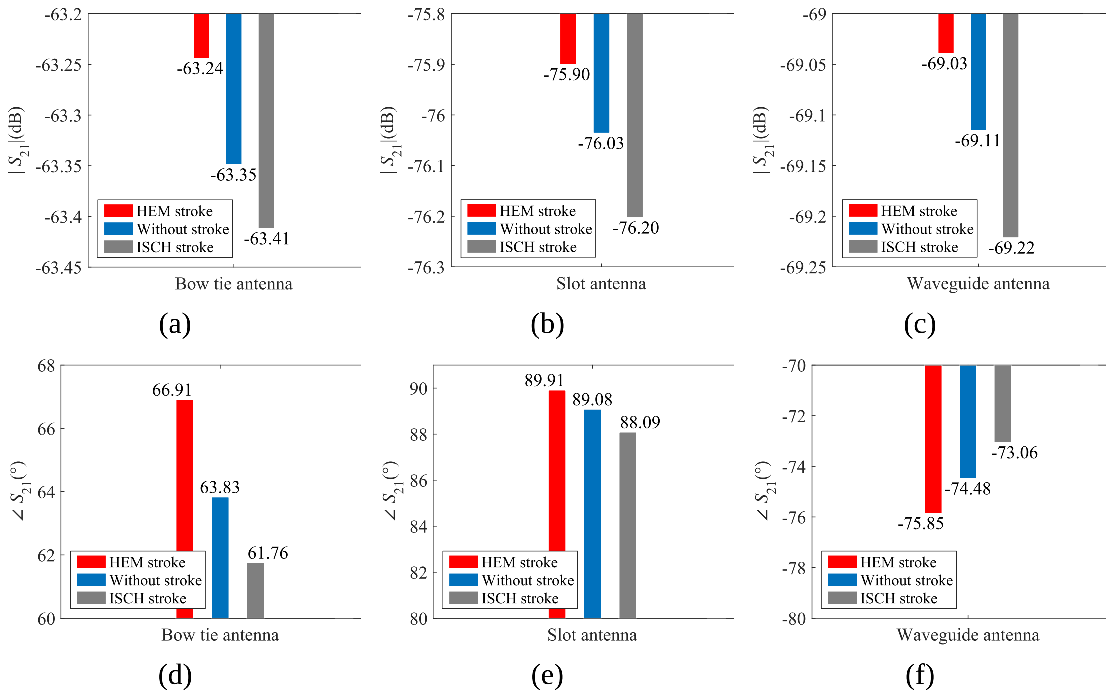

Figure 5.7 The magnitudes and phases of transmission coefficient S_{21} of bow tie antenna (a) and (d), slot antenna (b) and (e) and waveguide-based antenna (c) and (f) for the scenario without stroke phantom placed inside the head phantom and with Ø20mm HEM/ISCH stroke phantom. The single frequency of 1 GHz was considered.

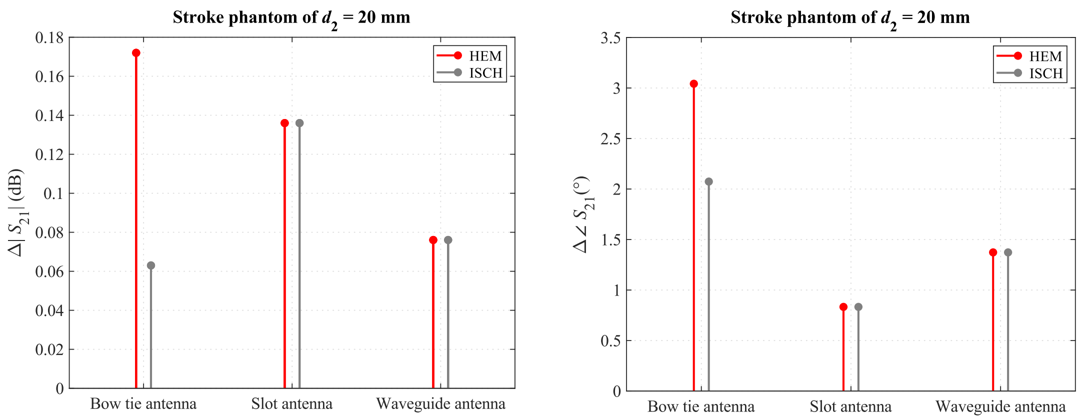

(a) (b)

Figure 5.8 The absolute differences of $\Delta|S_{21}|$ (dB) between scenario without stroke phantom placed in head phantom and with HEM/ISCH stroke phantom placed in head phantom (a) and ΔS_{21} (°) (b) for considered antennae and frequency of 1 GHz.

5.4.2 Antennas sensitivity to stroke phantom diameter

HEM stroke phantoms with six different diameters d_1 - d_6 = 10 – 60 mm were placed in the centre of the head phantom. The numerical differences of magnitude and phase of transmission coefficients at 1 GHz were fitted by 2nd order polynomial curve and Pearson's correlation coefficient R^2 in the 95% confidence interval was calculated. These results for each antenna type are shown in Figure 5.9.

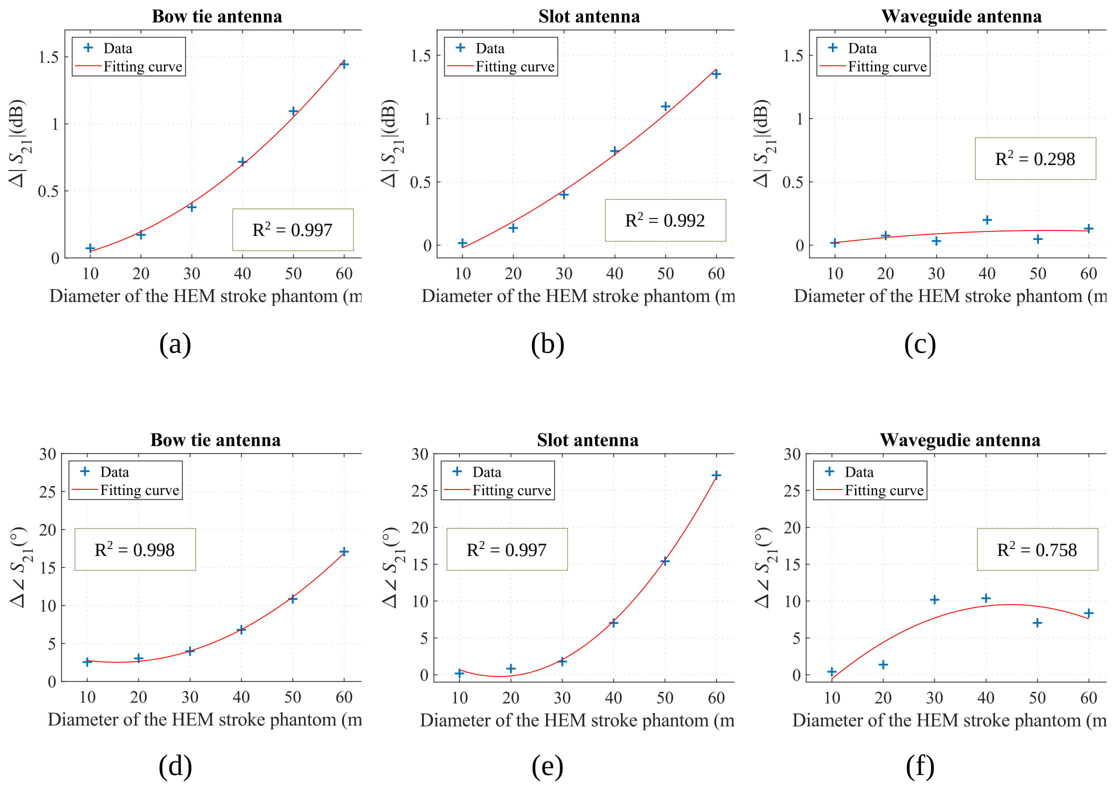

Figure 5.9 The absolute differences $\Delta|S_{21}|$ (dB) and $\Delta\angle S_{21}$ (°) between scenario without stroke phantom placed in head phantom and with HEM stroke phantom of diameters going from 10 to 60 mm for the bow tie antenna (a) and (d), for the slot antenna (b) and (e) and for the waveguide-based antenna (c) and (f). Obtained results were fitted by 2nd order polynomial function and Pearson´s correlation coefficient R^2 on 95% confidence interval were calculated.

5.4.3 Antennas radiation and immunity of plane wave exposure

The standard method for determining antenna radiation is to calculate the radiation pattern. With respect to antenna theory, the radiation pattern is defined in the far-field region, and it is hardly applicable for antennae used in the near-field region such as MWI applications. The distance of the far-field region can be calculated as the so-called Fraunhofer distance d_F (5.1). In this study, we determined the antenna radiation intensity to back domain (air) compared to radiation into lossy medium and we also determined antenna immunity against a plane wave exposure.

$$d_F = \frac{2D^2}{\lambda}, \tag{5.1}$$

where D (m) is the largest linear dimension of radiator and λ (m) the wavelength in the given medium.

At the same time, the Fraunhofer distance must be much greater than the largest radiator dimension D and D must be much greater compared to wavelength [17]. Introduced antennae operate in MWI systems in distances of up to 20 cm, which is an average front-back dimension of a human head [34]. Also, for radiation pattern evaluation, the lossless medium needs to be considered. However, in the MWI application, typically the lossy medium (e.g. human head) is placed in front of the antenna whereas the air is behind the antenna.

To overcome this limitation, we suggested a new methodology for estimating near-field antenna radiation. The sphere with a diameter of 20 cm surrounding each of antenna where the front domain (hemisphere) is defined as lossy medium (head phantom) of relative permittivity 41.8 and electrical conductivity 0.97 S/m, and the back domain is specified as air. The numerical model is shown in Figure 5.10. The magnitude of the intensity of the electric field $|\boldsymbol{E}|$(V/m) excited by each antenna element depending on the angle (°) in *xz* and *yz* plane (H- and E-plane) for the front (main lobe) as well as the back (back lobe) domain was evaluated and is presented in Figure 5.11. The electric field intensities were computed along the blue-marked edges displayed in Figure 5.10. In each plane, the angle was evaluated from -90 to 90 ° regarding the antenna position (top and bottom of the hemisphere stand for angle 0°).

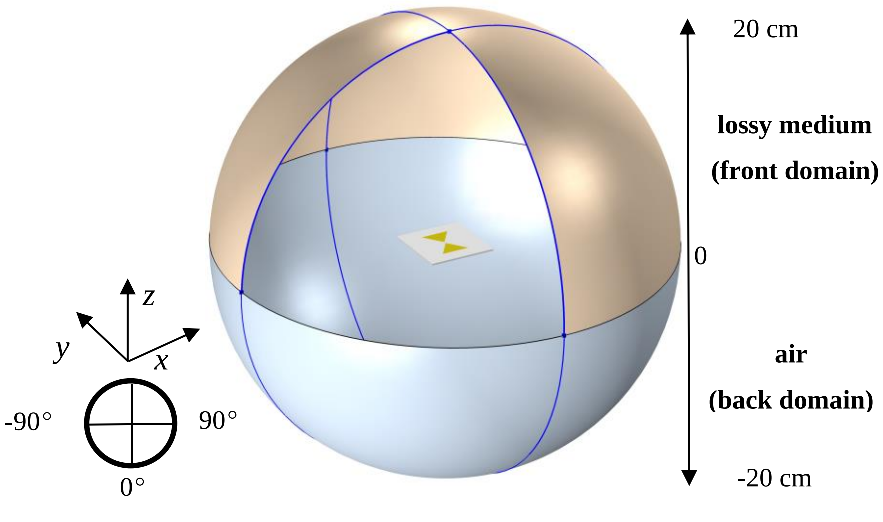

Figure 5.10 The example of the numerical model of a sphere with a radius of 20 cm surrounding the bow tie antenna element. The position of all antennae regarding the axis orientation was equal with respect to antennae polarization. The blue edges mark where $|\boldsymbol{E}|$ (V/m) depended on agle was evaluated.

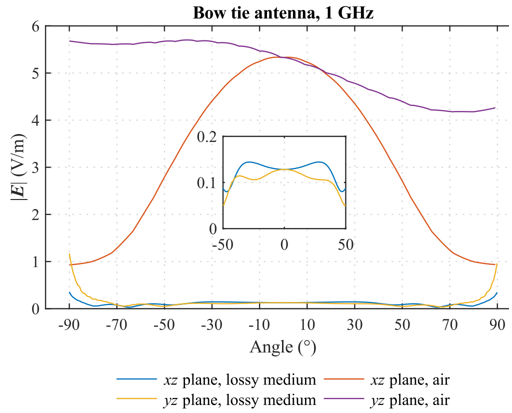

(a)

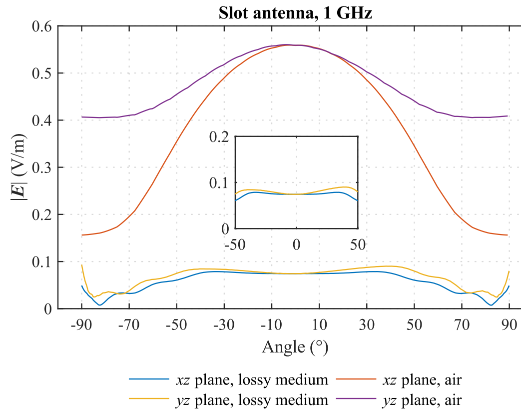

(b)

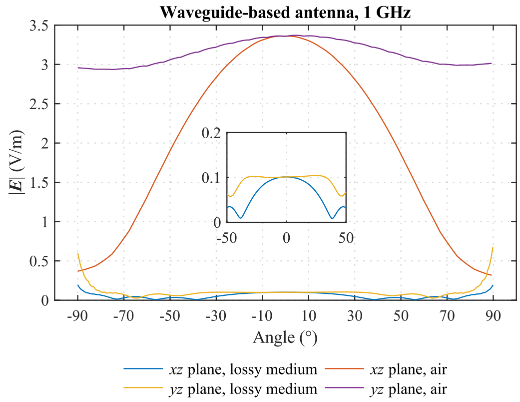

(c)

Figure 5.11 The computed magnitudes of the intensity of the electric field $|\boldsymbol{E}|$ (V/m) depended on angle (°), medium (lossy medium vs. air) and observation plane for bow tie antenna (a), slot antenna (b) and waveguide-based antenna (c).

Table 5.4 Calculated ratio $\boldsymbol{E}_{ratio}$ (-) between maximal electric field intensity (angle 0°) of the given antenna in the air (back lobe - back domain) and maximal electric field intensity in the lossy medium (main lobe - front domain). Also, the maximal values of intensity of electric field in lossy medium max $|\boldsymbol{E}_{lossy}|$ (V/m) are summarized.

	Bow tie antenna	**Slot antenna**	**Waveguide antenna**
$\sim\boldsymbol{E}_{ratio}$ (-)	40	8	32
max $\lvert\boldsymbol{E}_{lossy}\rvert$ (V/m)	0.13	0.07	0.1

To support the results of antennae radiation we evaluated antennae immunity against plane wave exposure. From the principle of reciprocity, the antenna with the lowest backward radiation should also prove highest immunity against planar wave exposure. The rectangular model combining the lossy medium (front domain) and air (back domain) was modelled as shown in Figure 5.12a. The user-defined Port 2 as a source of the plane wave of $|\boldsymbol{E}_z|$ = 1 V/m with propagation constant (m^{-1}) was excitated by frequency of 1 GHz while the Port 1 was set as 50Ω coaxial receiving port. The result of the numerical study was magnitudes of transmission coefficient $|S_{12}|$ (dB) of each of the examined antennae which are compared in Figure 5.12b.

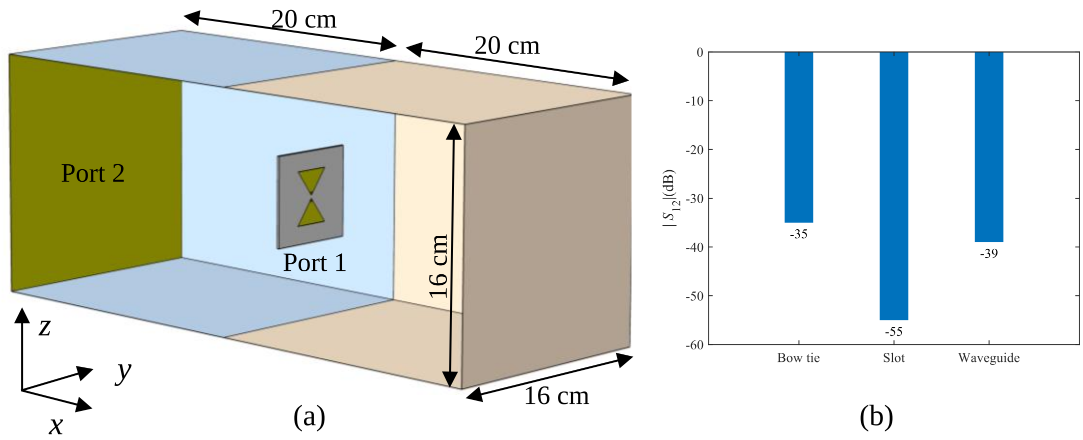

Figure 5.12 The model for evaluation of antenna immunity against the plane wave exposure (a) where the lossy medium is a light orange coloured and the air is a light blue. Comparison of magnitudes of transmission coefficients $|S_{12}|$ (dB) of each model with the corresponding antenna (b).

5.5 H-slot antenna design and experimental validation

The main aim of this subchapter is to introduce the process of developing a new compact antenna element suitable for a multichannel (> 20 antennae) MWI system for the detection of brain strokes. The antenna requirements as a reasonable sensitivity of transmission coefficient due to dielectric contrast, small dimensions, symmetrical feeding, and unidirectional radiation were determined. In addition, based on results of numerical analysis presented in previous subchapter and with respect to the concept of slot antenna introduced in [25], the new H-slot antenna was designed, fabricated, and experimentally verified using for this purpose constructed 2-port test system.

First, the shape of the H was parametrised in COMSOL Multiphysics, and the parametric study was conducted to obtain a sufficiently low antenna reflection coefficient for the resonance frequency of 1 GHz. The phantom of the human head was carried out as shown in Figure 5.13.

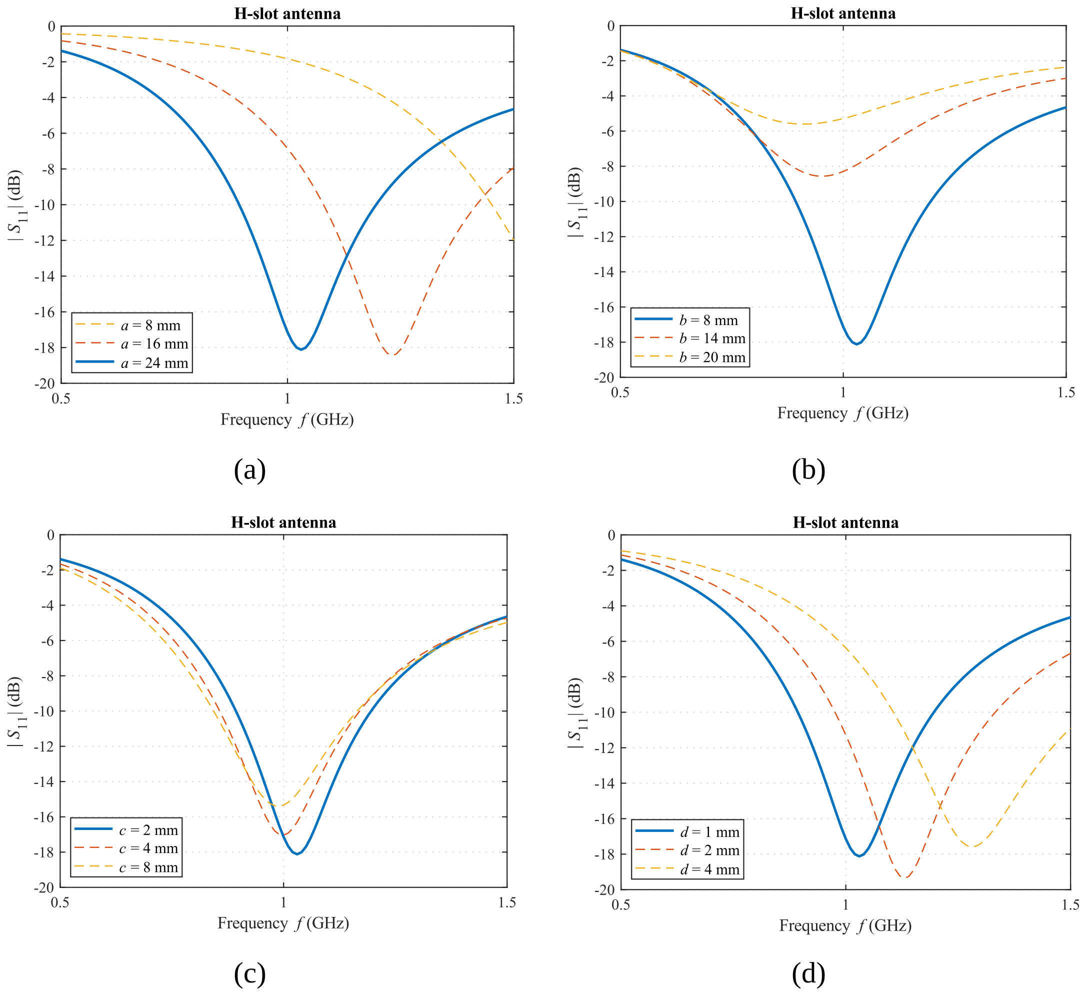

Figure 5.13 The magnitude of $|S_{11}|$ (dB) obtained by parametric study for different dimensions of H slot. The blue curve corresponds to $|S_{11}|$ of antenna with final dimensions.

The double-layered structure (two substrates with a thickness of 1.5 mm) with a ground plane was considered. A microstrip line to feed the antenna was placed between the substrates, as illustrated in Figure 5.14c, e. The microstrip line was directly connected to the 50Ω coaxial line and two Ø1,3mm vias on one side of H slot. Therefore, the symmetric feeding was reached without the need of a balun. Other three 1mm vias connected the ground plane with the antenna slot plane are depicted in Figure 5.14e, f.

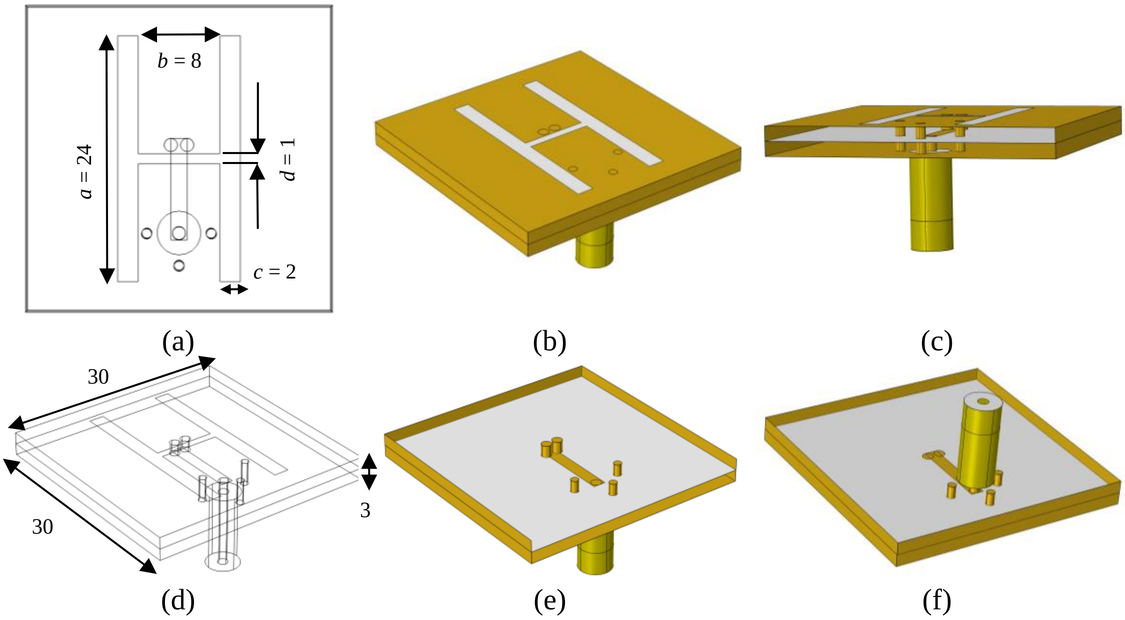

Figure 5.14 Designed H-slot antenna with its final dimensions (mm) from a top view (a), from perspective view (b) and (d) where metal parts of the antenna are yellow coloured and substrate parts together with teflon are grey coloured. In (c) the connection of coaxial line to microstrip is shown as well as vias. In (e) and (f) the top view on vias and microstrip and the bottom view is displayed.

The magnitude of the intensity of the electric field (V/m) depended on an angle (°) in *xz* and *yz* plane (H- and E-plane) for the front as well as the back domain was computed also for H-slot antenna and is presented in Figure 5.15a. The immunity of H-slot antenna against the plane wave exposure was compared with results introduced in subchapter 5.4.3 and is shown in Figure 5.15b.

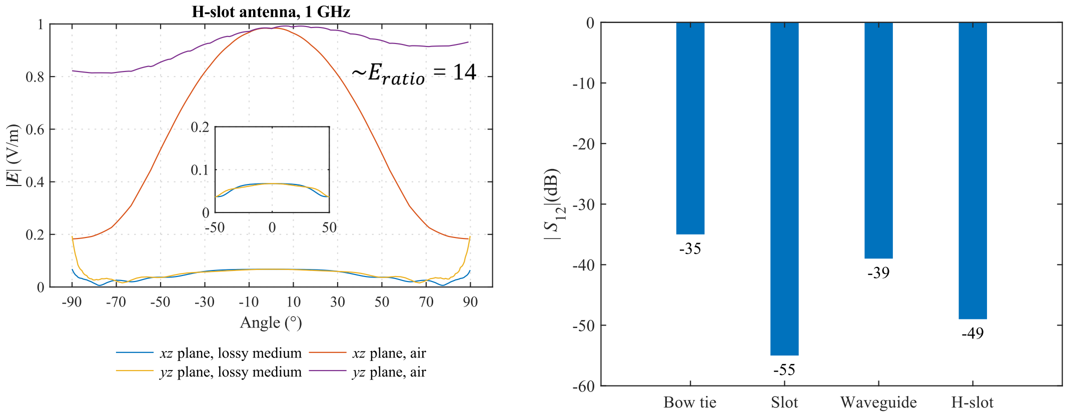

(a) (b)

Figure 5.15 The magnitudes of the intensity of the electric field $|\boldsymbol{E}|$ (V/m) depended on angle (°), medium (lossy medium vs. air) and observation plane (a) and magnitudes of transmission coefficients $|S_{12}|$ (dB) of H-slot antenna regarding plane wave exposure immunity compared with other investigated antennae in (b).

In addition, to show the symmetrical antenna E-field radiation the normalized magnitude of intensity of electric field of slot of the proposed antenna together with the vectors in *x* and *y* directions are shown in Figure 5.16.

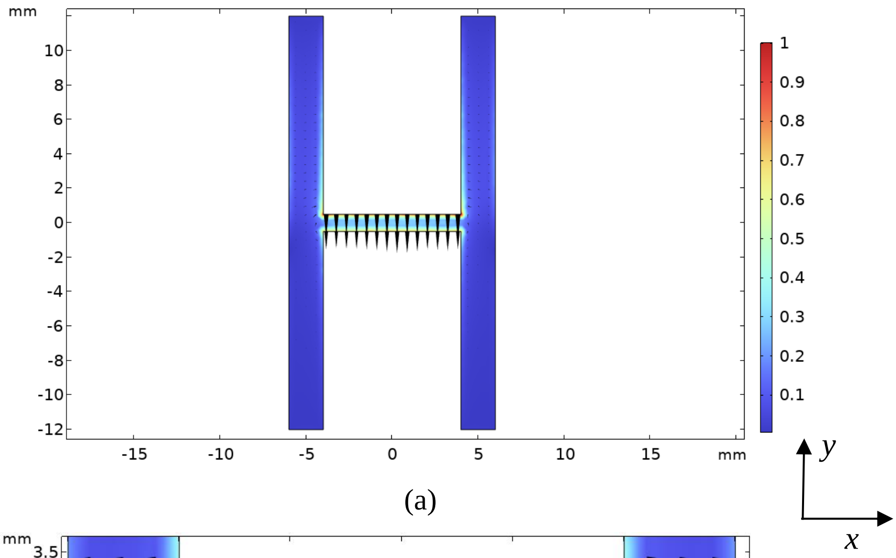

(a)

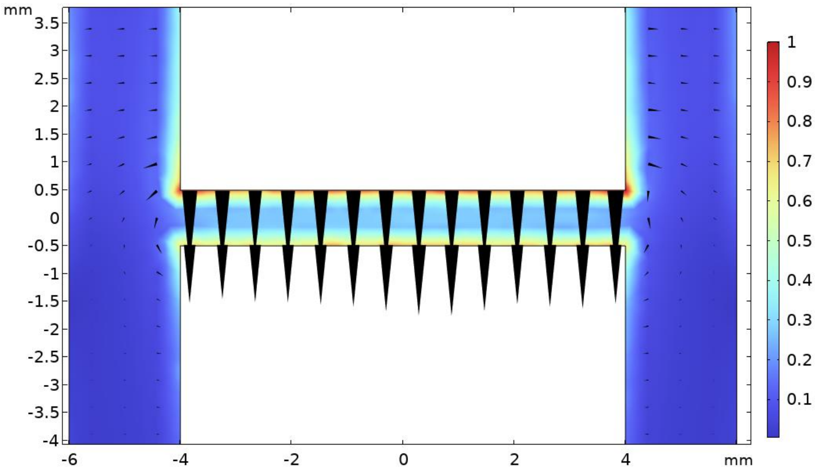

(b)

Figure 5.16 Normalized magnitude of E-field intensity inside the slot of proposed antenna (a) and detail on slot in (b). The black cones show the vectors of E-field intensity in *x* and *y* direction.

RF substrates Rogers R04003C of size 30 by 30 mm and thickness of 1.5 mm (ε_r =3.55, σ = 0.0004 S/m) covered with 18 Cu layer were used for antenna fabrication. Considering the complex structure of H-slot antennas, the fabrication process was realised by a Pragoboard s.r.o. company (Prague, Czech Republic) based on Gerber format files exported from software EAGLE (Autodesk, USA). The image of the fabricated antenna is shown in Figure 5.17a, and b. The high-precision SMA connectors Rosenberg 32K 10A-40M L5 were soldered to antennas by a hot air soldering station. The accurate position of the SMA connector was secured by a cuprextit plate fabricated in-house on a CNC cutter, see Figure 5.17c.

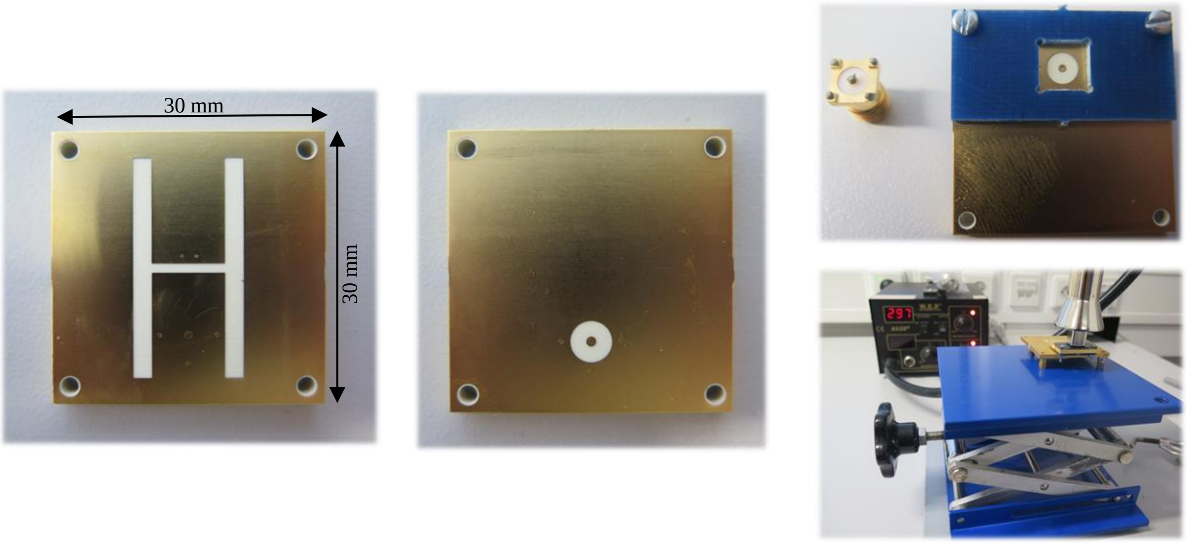

(a) (b) (c)

Figure 5.17 Fabricated H-slot antenna element from a top view (a) and bottom view (b). The cuprextit plate, SMA connector and process of soldering by hot air in (c).

For experimental validation, the rectangular box and the 20mm spherical stroke phantom were printed on the Prusa i3 MK2S 3D printer (Prusa Research s.r.o., Czech Republic). The two H-slot antennas were mounted on the box using plastic screws as illustrated in Figure 5.20. The box was filled with the liquid head phantom which was prepared mixing of propylene glycol, water and salt [65] as summarized in Table 5.5. The HEM stroke phantom was prepared by adding water and salt to the head phantom to reach dielectric parameters around 20 % higher. Dielectric parameters of the phantoms were measured using the DAK-12 probe in the frequency range 10 MHz – 3 GHz and supplemented with an extended uncertainty of type C with a coverage factor equal to 2 (Figure 5.18). Subsequently we fitted the second order polynomial curve and Pearson’s correlation coefficient R^2 was calculated on a 95% confidence interval to obtain a realistic function of the dielectric properties based on frequency for numerical simulations. The functions are reported in Figure 5.19.

Table 5.5 Weight percentages of substances used for the preparation of the human head phantom and expected target dielectric parameters, relative permittivity and electrical conductivity σ, as well as measured dielectric parameters of head and HEM stroke phantom for the frequency of 1 GHz supplemented with extended uncertainty of type C.

	Propylene glycol	**NaCl**	**Water***
w%	64.81	0.79	34.40
Head phantom			
Target ε_r (-)	41.80		
Target σ (S/m)	0.97		
Measured ε_r (-)	41.73 ± 0.82		
Measured σ (S/m)	0.97 ± 0.029		
HEM stroke phantom			
Target ε_r (-)	50.16		
Target σ (S/m)	1.16		
Measured ε_r (-)	50.21 ± 2.80		
Measured σ (S/m)	1.07 ± 0.061		

*distilled water

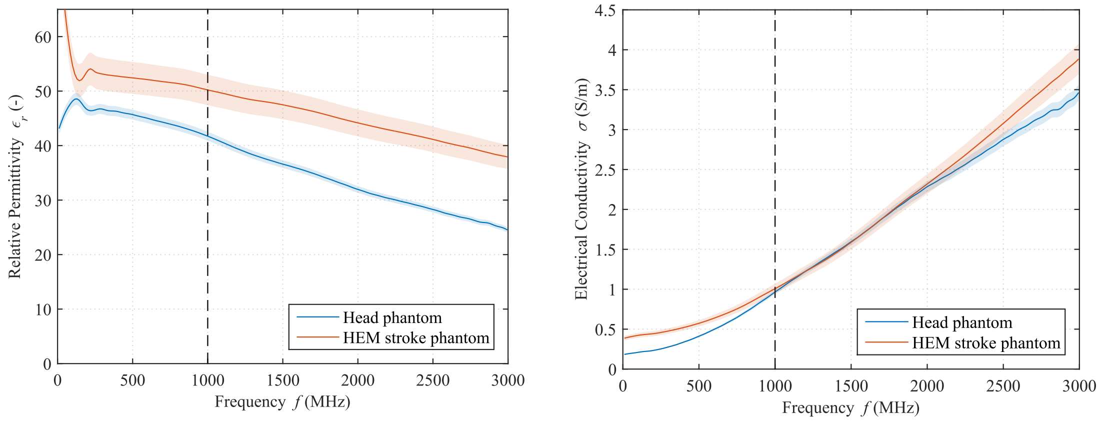

(a) (b)

Figure 5.18 Measured dielectric parameters of the average human head phantom with extended uncertainty of type C displayed as a light shadow, relative permittivity (a) and electrical conductivity (b). The frequency of 1 GHz is marked by a black dashed line.

$\varepsilon_r(f) = -2.3 \cdot 10^{-6} \cdot f^2 - 4.9 \cdot 10^{-3} \cdot f + 48.8$ $\quad\quad$ $\sigma\,(f) = 1.4 \cdot 10^{-7} \cdot f^2 + 9.5 \cdot 10^{-4} \cdot f - 0.13$

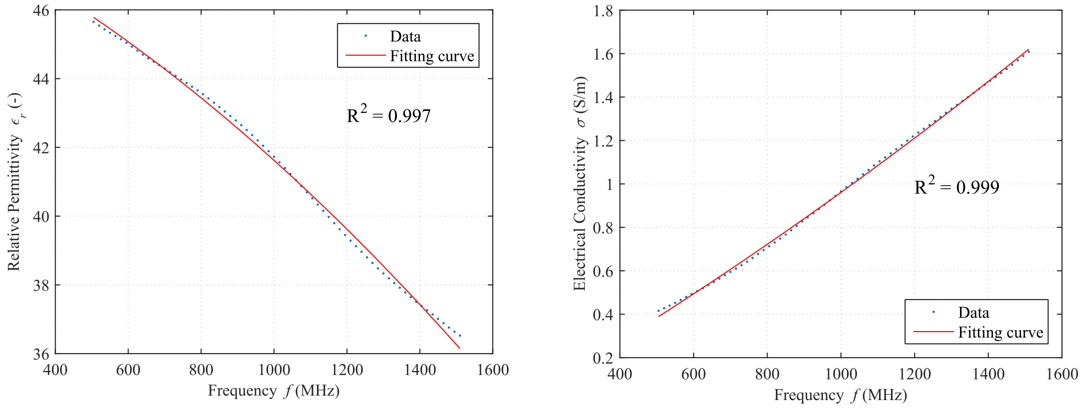

(a) $\quad\quad$ (b)

Figure 5.19 Measured relative permittivity (a) and electrical conductivity (b) of the head phantom in the frequency range 500 – 1500 MHz fitted by 2nd order polynomial curve and calculated correlation coefficient R^2 on a 95% confidence interval.

The two-port VNA R&S® ZNB 8 (Rohde & Schwarz GmbH, Germany) with dynamic range >120 dB operating up to frequency 8.5 GHz was used to measure reflection as well as transmission coefficients of a couple of H-slot antennas attached to a 3D printed box. Calibration of the VNA ports was performed using the automatic 6-port calibration kit R&S® ZN-Z152 (Rohde & Schwarz GmbH, Germany). The S parameters of the system were measured in the frequency range from 0.5 to 1.5 GHz with an intermediate frequency bandwidth of 10 Hz and a VNA output power of 10 dBm. The results of the measurements were compared with the numerical results and are shown in Figure 5.21. In addition, a comparison of the measured magnitudes and phases of transmission coefficients of the system without and with the placed 20mm HEM stroke phantom was made and is shown in Figure 5.22. The standard deviation of all measurements moved in order of 10^{-6} dB. Last but not least we compared the measured magnitudes and phases of transmission coefficients with numerically obtained ones for the H-slot antenna and the previously introduced slot antenna, as demonstrated in Figure 5.23.

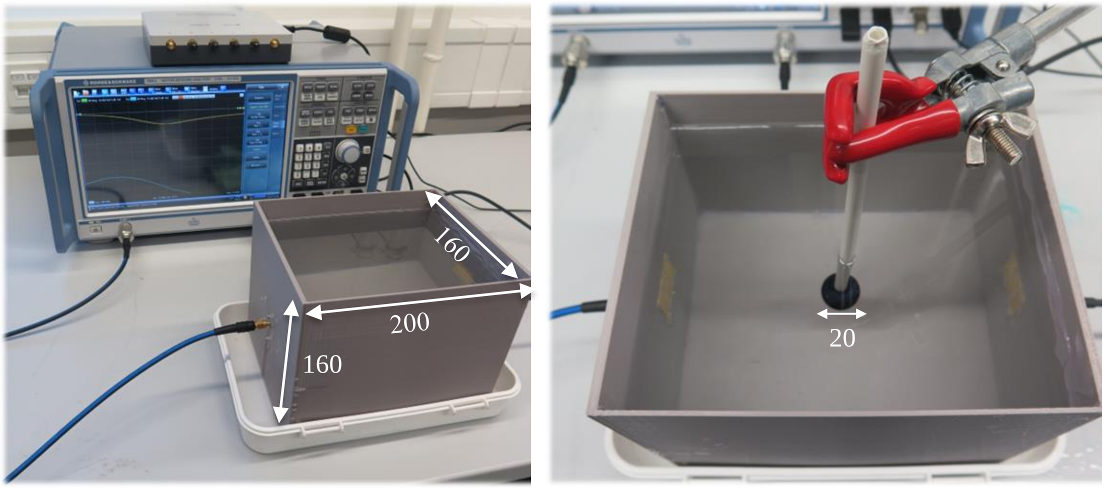

(a) (b)

Figure 5.20 The experimental configuration for H-slot antenna validation consisting of 3D printed box with dimensions (mm), liquid head phantom, VNA and calibration kit (a). Detail of positioning of HEM stroke phantom with the diameter of 20 mm to the middle of the system (b).

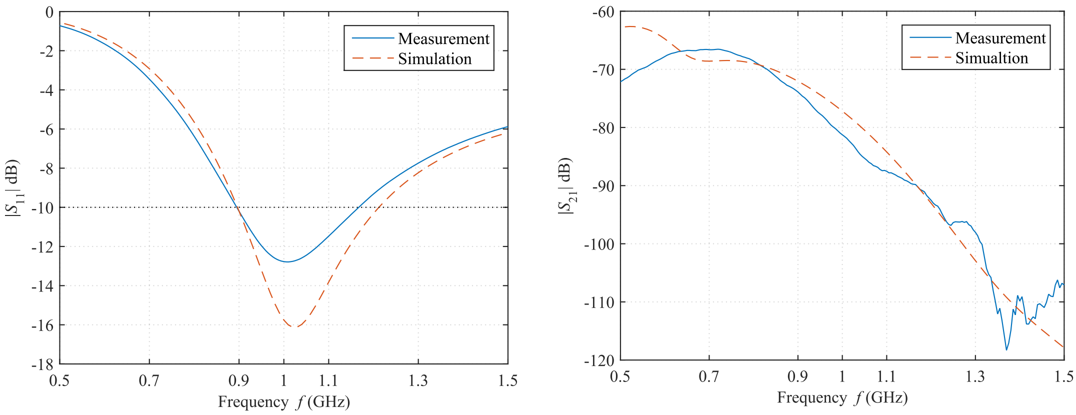

(a) (b)

Figure 5.21 Comparison of measured and numerically computed magnitudes of reflection coefficient (a) and transmission coefficient (b) of a couple of H-slot antennas mounted in the experimental system. The level of -10 dB is marked in (a) by the black dotted line.

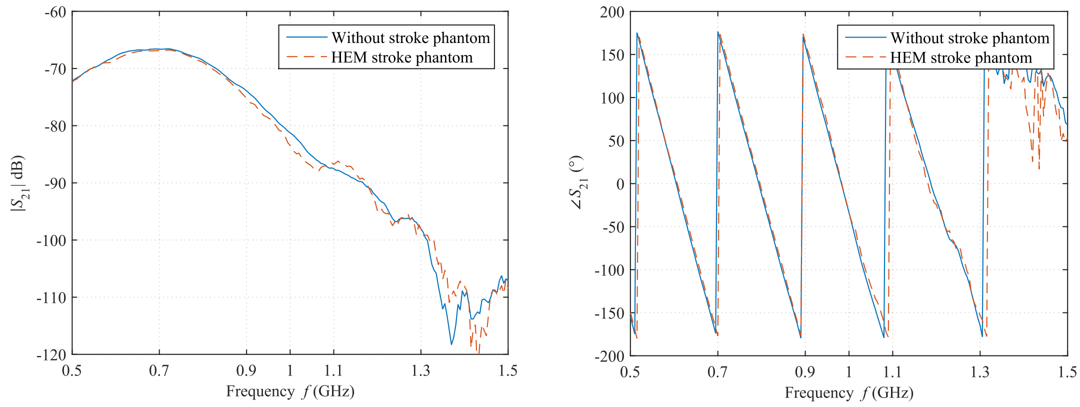

(a) (b)

Figure 5.22 Comparison of measured magnitude (a) and phase (b) of the transmission coefficient of H-slot antennas for the case without and with the 20mm HEM stroke phantom placed inside the 2-port system.

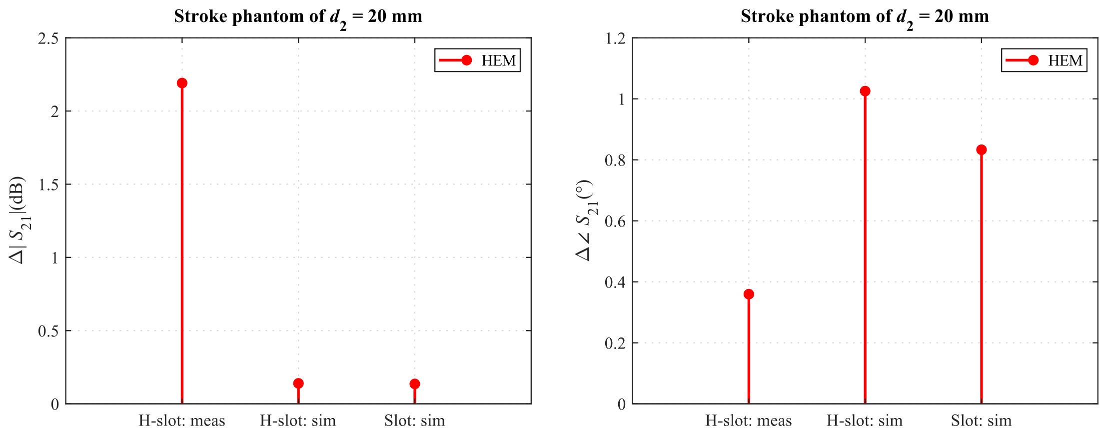

(a) (b)

Figure 5.23 Comparison of measured (meas) differences of magnitudes (a) and phases (b) of transmission coefficients with numerically obtained (sim) of H-slot and slot antenna for frequency of 1 GHz and considered HEM stroke phantom inside the 2-port system.

5.6 Multilevel 24-port MWI system

Previously introduced single-plane (antennas positioned in one level) MWI systems [25], [66] proved promising potential for methodical testing of brain stroke follow-up. Scanning with these systems was possible only for liquid or 2,5D phantoms of the human head. The various convexities of human skulls require a new approach to the development of MWI systems. More emphasis should be placed on increasing the number of antennas and their layout to cover the whole skull geometry. In addition, the adaptability of MWI systems due to different skull shapes must be considered. The increased number of antennas in the MWI system should also provide a higher optical image resolution, but the compactness and portability of the MWI system must be preserved. On the other hand, the higher risk of distortion of useful signal due to antenna coupling is obvious. Therefore, lossy coupling mediums or small, compact antennas with dominant unidirectional radiation and ground plane are desirable to use in such multichannel systems.

The newly developed H-slot antenna proposed in previous Chapter 5.5 is suitable to be used in multilevel 24-port MWI system. The number of 24 elements was identified based on analysis performed in [67], [68]. In addition, the hardware (switching matrix) available in the laboratories of BioEM group at FBME CTU in Prague allows to connect at maximum 24-port devices.

5.6.1 Numerical study

We suggested antenna layout in three levels (bottom – 12 AEs, middle – 10 AEs, and top – 2 AEs) equidistantly spaced around average realistic human head geometry as shown in Figure 5.24. The geometry (the upper part of the human head from the beginning of the forehead to top of the head:(x = 20 cm, y = 16 cm, z = 12 cm) was based on MRI-derived data of human head tissues available from The Population Head Model V1.0 of the IT’IS Foundation database [34].The numerical model was extended by 2 mm layer of PLA plastic material due to future experimental measurements on homogeneous liquid-filled 3D printed head phantom.

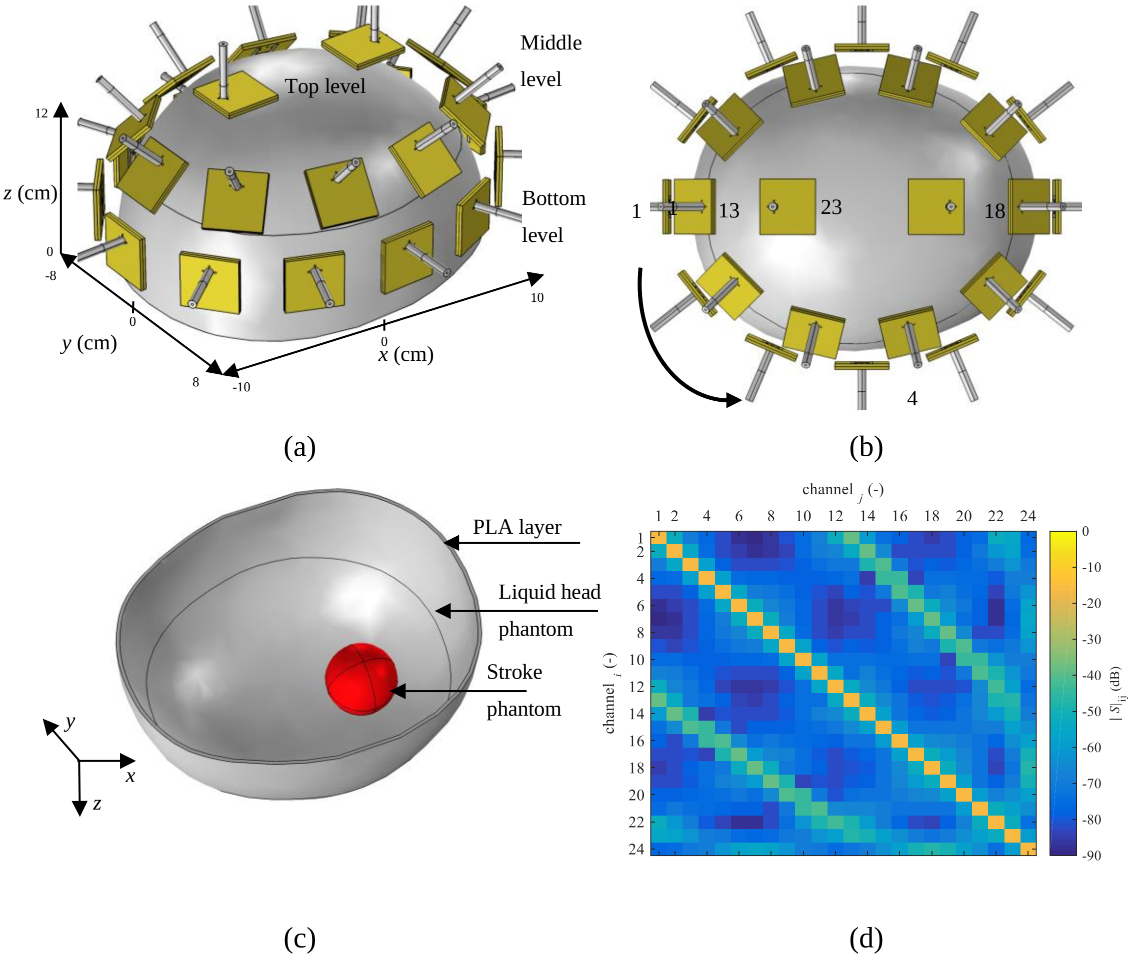

Figure 5.24 The H-slot antenna layout of 24-port MWI system from perspective view (a) where the individual levels are marked and from the top view (b) where ports are numbered. The matching medium between antennas and the head phantom is not displayed here for the sake of clarity. In (c) detail on numerical model of head and stroke phantom. (d) numerical S-matrix with corresponding pairs of transmission and reflection coefficients.

To validate the 24-port MWI system on synthetic numerical data a full-wave electromagnetic field simulations were performed. The two different types of stroke phantoms were considered by means of its dielectric parameters, as well as different diameters and positions. Based on previous results related to the spatial resolution of the 2D MWI system, Chapter 4.4, the diameters of stroke phantoms were set to 10, 20 and 40 mm. The values of the dielectric parameters of stroke phantoms were calculated as 10, 20% decrease (ISCH) or increase (HEM) against the parameters of the head phantom [36], respectively, summarized in Table 5.6.

Table 5.6 Dielectric parameters of considered phantoms and the rounded differences δ of relative permittivity and electrical conductivity of HEM and ISCH stroke phantoms and brain phantom.

Diel. Param.	**Phantoms**				
	Head	**HEM10**	**HEM20**	**ISCH10**	**ISCH20**
$\boldsymbol{\varepsilon_r}$ **(-)**	41.8	46.0	50.2	37.6	33.4
σ (S/m)	0.97	1.1	1.2	0.9	0,77
δ $\boldsymbol{\varepsilon_r}$ **(-)**		+4.2	+8.4	-4.2	-8.4
δ **σ (S/m)**		+0.13	+0.23	-0.07	-0.2

The numerical S-matrices and intensities of electric field each of antenna port in *x*, *y*, and *z* direction for frequency of 1 GHz and different scenarios were computed. The differential microwave imaging approach was applied employing again the Born approximation and regularization by TSVD (Chapter 3). The differential relative permittivity and conductivity profiles obtained by reconstruction of synthetic numerical data in a plane through the middle of spherical stroke phantoms are presented in Figure 5.25.

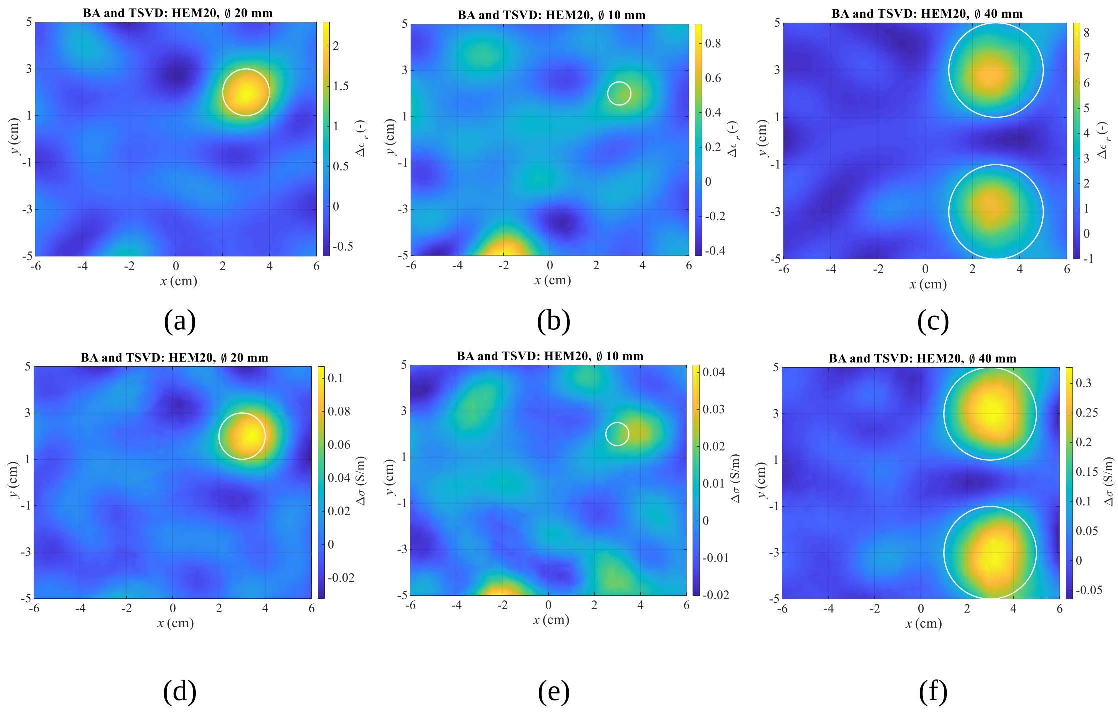

Figure 5.25 Continued.

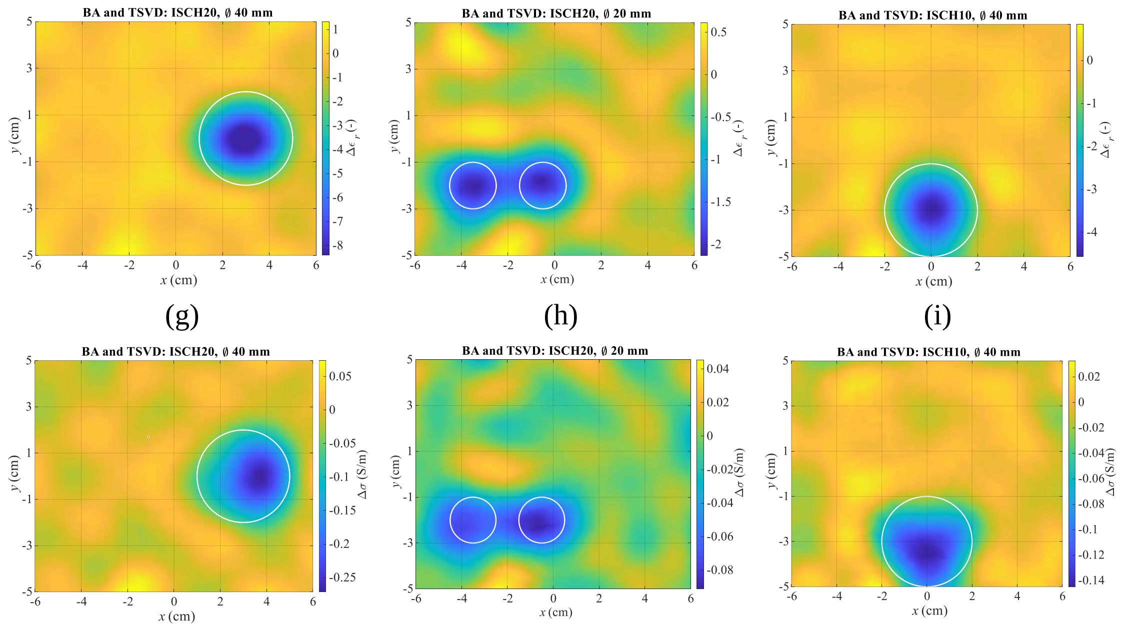

(g) (h) (i)

(j) (k) (l)

Figure 5.25 Reconstructed profiles of differential relative permittivity and conductivity Δ (a-f) for HEM stroke phantoms and for ISCH phantoms (g-l) based on numerical synthetic data obtained by 24-port multilevel MWI system.

5.6.2 Experimental validation

The validation was focused on ability of MWI system to determinate the type of stroke phantom based on increase/decrease of local dielectric contrast. Also, on the qualitative and quantitative parameters of retrieved dielectric contrast in comparison with actual (measured) contrast between head phantom and stroke phantoms. The suggested antennas layout was in previous chapter used as a pattern for modelling a helmet-similar antennas holder with dimensions as presented in Figure 5.26.

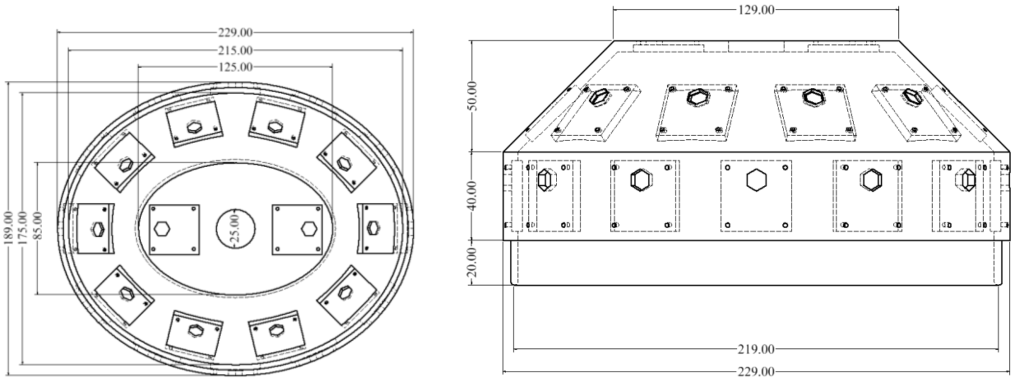

Figure 5.26 Scheme of designed holder for antennas layout with dimensions in (mm).

The model was 3D printed and assembled with 24 H-slot antennas as depicted in Figure 5.27a. The helmet was suitable for fitting on an average 3D printed head model allowing to be filled with homogeneous liquid head phantom as well as on the 3D realistic head phantom. The liquid stroke phantoms were imitated by inflatable plastic balloon put on plastic loading tube which was possible to place in different positions in axis *x*, *y* and *z*-axis (Figure 5.28). The movement in *z*-axis was determined based on antenna levels (Figure 5.24). The middle level was equal to 0 mm, while bottom level to -20 mm and top level to +20 mm as illustrated in Figure 5.28. The space between helmet and head model was filled with a matching medium equal in terms of dielectric properties to the average head phantom. For this purpose, the swim cap was used (Figure 5.27b).

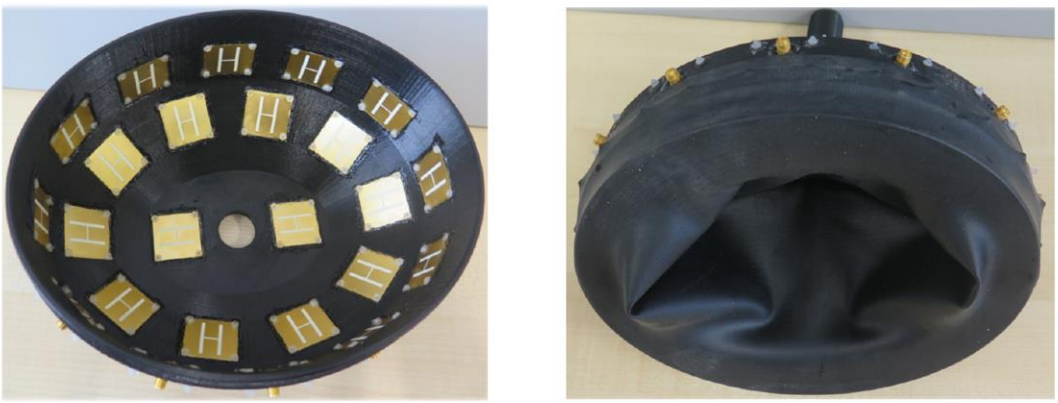

(a) (b)

Figure 5.27 H-slot antennas assembled inside the 3D printed helmet-based holder/multilevel MWI system (a), used swim cap to ensure proper contact of antennas and head model through matching medium filled inside the system (b).

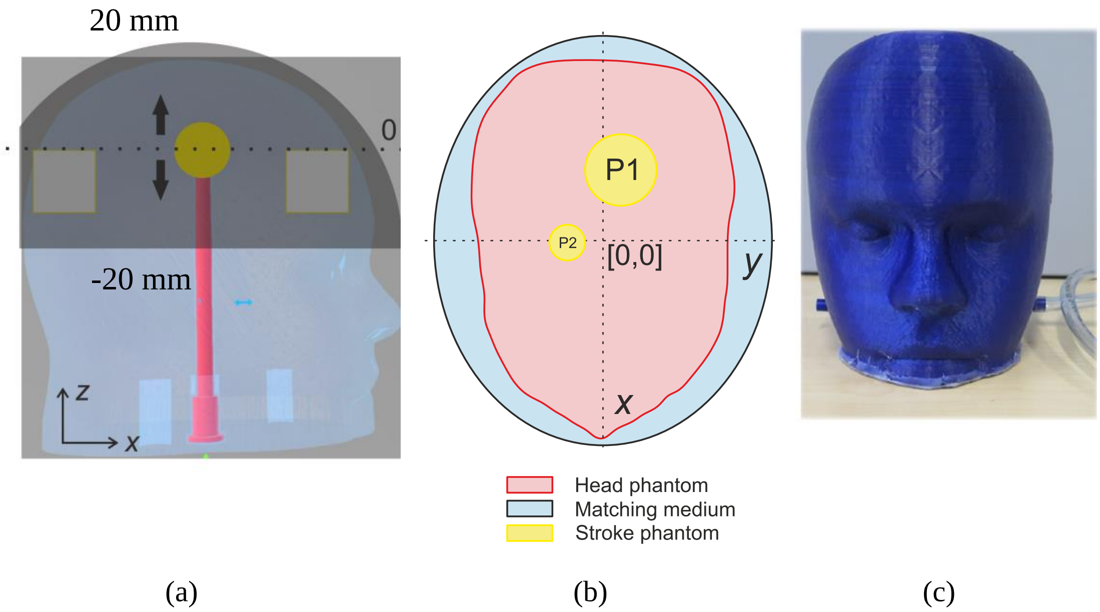

Figure 5.28 The head model from sagittal view (a) where MWI system is marked transparent black, antennas grey and spherical stroke phantom with loading tube yellow/red. Transversal schematic cut (b) with marked stroke phantom positions P1, P2 and 3D printed head model (c).

Table 5.7 Coordinates of considered positions P1, P2 of spherical stroke phantoms as well as diameters D or volumes V, respectively.

	x (mm)	y (mm)	z (mm)	D (mm)/V (ml)
P1	40	10	-20	20|40/5|33
P2	0	-20	20	20|40/5|33

For the purpose the position of stroke phantom in z-axis were chosen bellow the bottom antennas level (-20 mm) and to the top of MWI system where the antennas cumulation is the highest. The performance of the designed 24-port MWI system was verified by experimental measurements as shown in Figure 5.29. The stroke phantom (balloon) was filled using standard syringe. The VNA R&S® ZNB 4, switching matrix R&S® ZN-Z84 (both Rohde&Schwarz GmbH, Germany) were employed to acquire data. The real dynamic range of matrix is 95 dB. The input power of VNA was set to maximal 13 dBm, intermediate frequency (IF) bandwidth filter to minimal 10 Hz. One dataset with no stroke phantom inside the head phantom – $\boldsymbol{t_0}$ and second in $\boldsymbol{t_n}$ when stroke phantom was present. Differential data were processed using BA and TSVD.

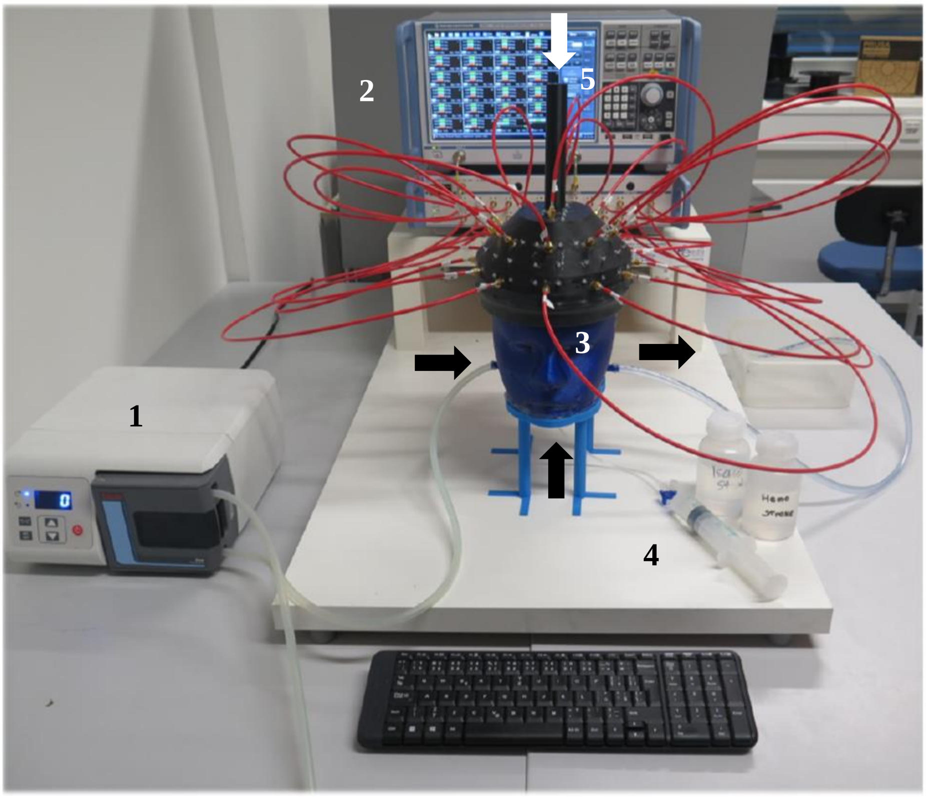

Figure 5.29 Experimental setup for 24-port multilevel MWI system validation on 3D printed head model filled with average homogeneous liquid phantom and stroke phantom. **1**-peristaltic pump and inlet/outlet for liquid head phantom, **2**-VNA+switching matrix, **3**-MWI system+head model, **4**-syringe used to fill balloon inside head representing stroke phantom, **5**-inlet for matching medium.

To objectively quantify and qualify the capability of MWI system to detect stroke position, size as well as its type we suggested and calculated a several metrics. For the verification of stroke phantom location (qualitative information) the **sensitivity**, **specificity** and **accuracy** of method was evaluated. We considered the classification of each pixel of reconstructed imaged to identified it true or false. In addition, we compared reconstructed target with actual one in terms of its area – **area ratio** as well as absolute difference of centre of gravity between reconstructed target and actual - **localization error.**

Quantitative information i.e. maximal differential dielectric contrast of reconstructed target vs. actual target was compared using standard **relative error**. For the application of brain stroke detection, the absolute value of reconstructed contrast vs actual is not the main criteria of successful stroke type identification. Rather ratio between peak retrieved contrast value and background noise. Therefore, we calculated peak signal-to-noise ratio **PSNR** as

$$PSNR = 20 \cdot log_{10} \left(\frac{\theta_{MAX}}{\sqrt{MSE}} \right), \tag{5.2}$$

where θ_{MAX} is the maximal pixel value of retrieved image and **MSE** is mean squared error defined as follows

$$MSE = \frac{\sum_{n=1}^{N} (\Delta(r) - \delta(r))^2}{N}, \tag{5.3}$$

where N is number of samples r of the discretized domain, Δ retrieved differential contrast and δ actual contrast.

The whole process of image evaluation strongly depends on the choice of threshold for initial reconstructed image segmentation. By the thresholding of the normalized reconstructed image the binary mask is created where 1 is assigned to every pixel with higher value then the threshold and 0 to remaining pixels. Observing our normalized reconstructed images, we determined the threshold to be **0,5/-6 dB** or **0,7/-3 dB,** respectively, depending on stroke phantom diameter and relative permittivity/conductivity. These values correspond well with the ROI (target).

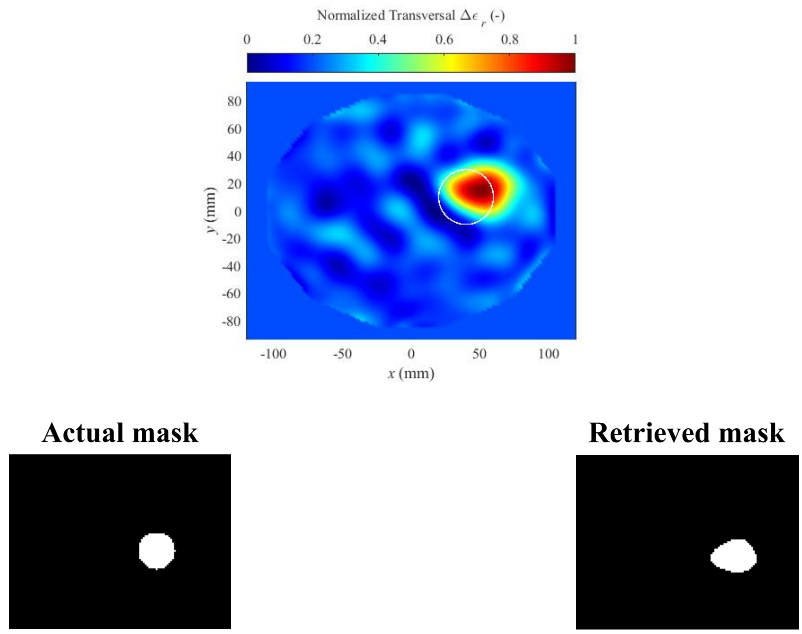

Figure 5.30 Example of retrieved normalized differential contrast of relative permittivity, retrieved binary mask and actual binary mask for threshold of –6 dB.

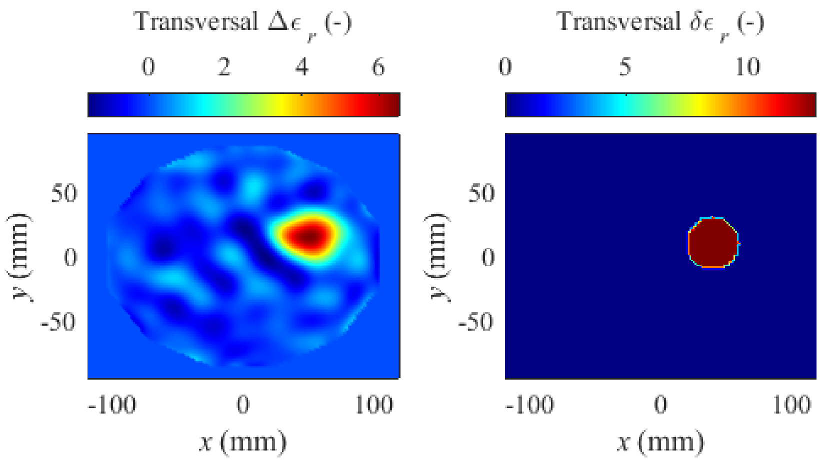

Figure 5.31 Comparison of retrieved differential contrast of relative permittivity on the left and actual contrast on the right used for quantitative images evaluation.

The head as well as stroke phantoms (ischemic **ISCH20** – decrease of dielectric properties around 20 % [36] and haemorrhagic **HEM** – phantom of blood were prepared as mixture of Isopropyl alcohol (IPA), distilled water, salt and its dielectric parameters were measured in frequency range from 500 to 3000 MHz using conventional open-ended coaxial probe DAK 3.5 (Schmid & Partner Engineering AG, Switzerland). The measured data were statistically evaluated by extended uncertainty of type C in a 95% confidential interval with coverage factor k = 2.

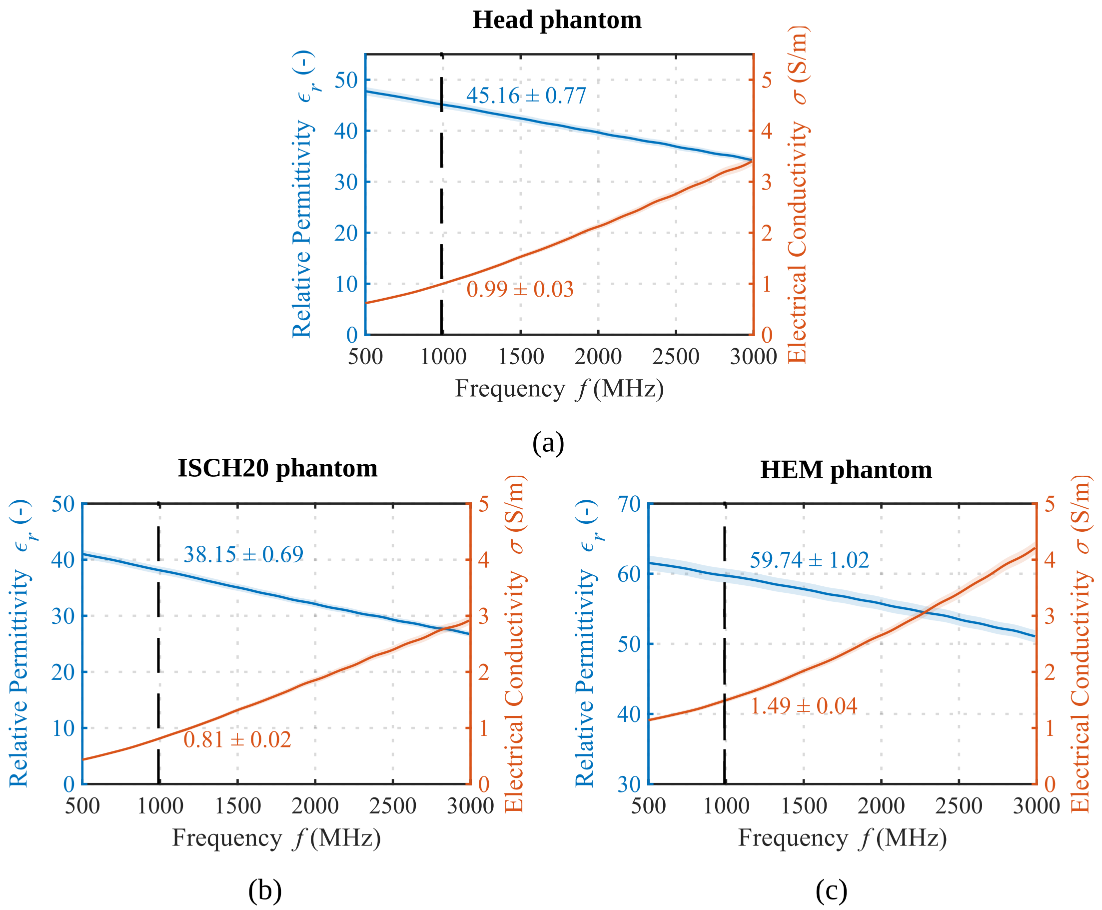

Figure 5.32 Measured dielectric parameters of head phantom (a), ISCH20 stroke phantom (b) and HEM stroke phantom (c). The exact parameters for frequency of 1 GHz with extended uncertainty of type C are plotted. The type C uncertainty is also displayed by shading in whole frequency spectrum.

The reconstructed differential dielectric profiles $\Delta\varepsilon_r$ (-) and $\Delta\sigma$ (S/m) in anatomical planes for various stroke phantom types, positions and diameters.

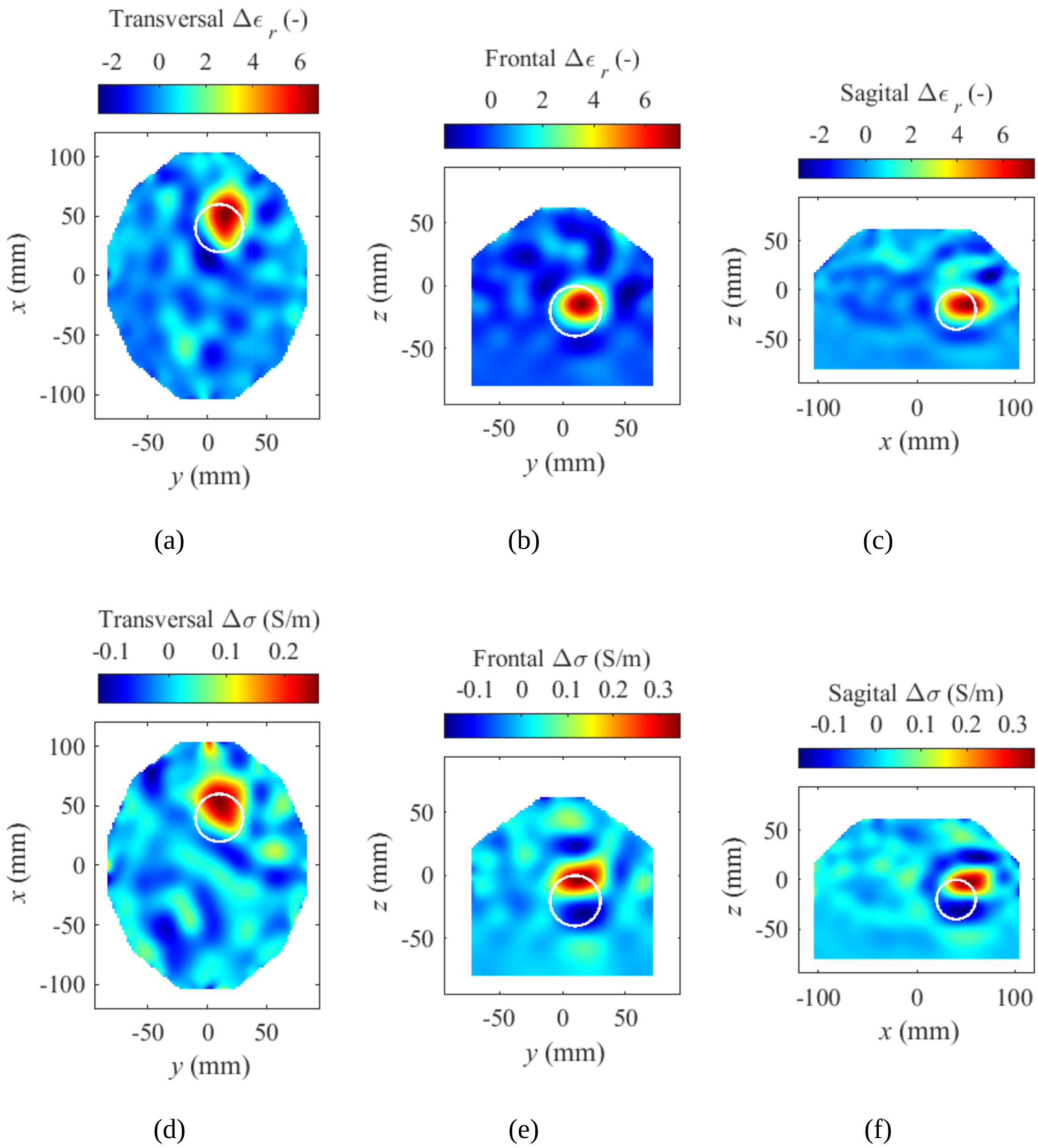

Figure 5.33 Reconstructed differential relative permittivity $\Delta\varepsilon_r$ (-) in (a)-(c) and conductivity $\Delta\sigma$ (S/m) in (d)-(f) for **HEM** stroke phantom on position **P1** with diameter **40 mm**. The slices in anatomical planes leads through maximal detected dielectric contrast. The white circle indicates the expected stroke phantom position. Maximal truncation level $\boldsymbol{N_T}$ **= 300**.

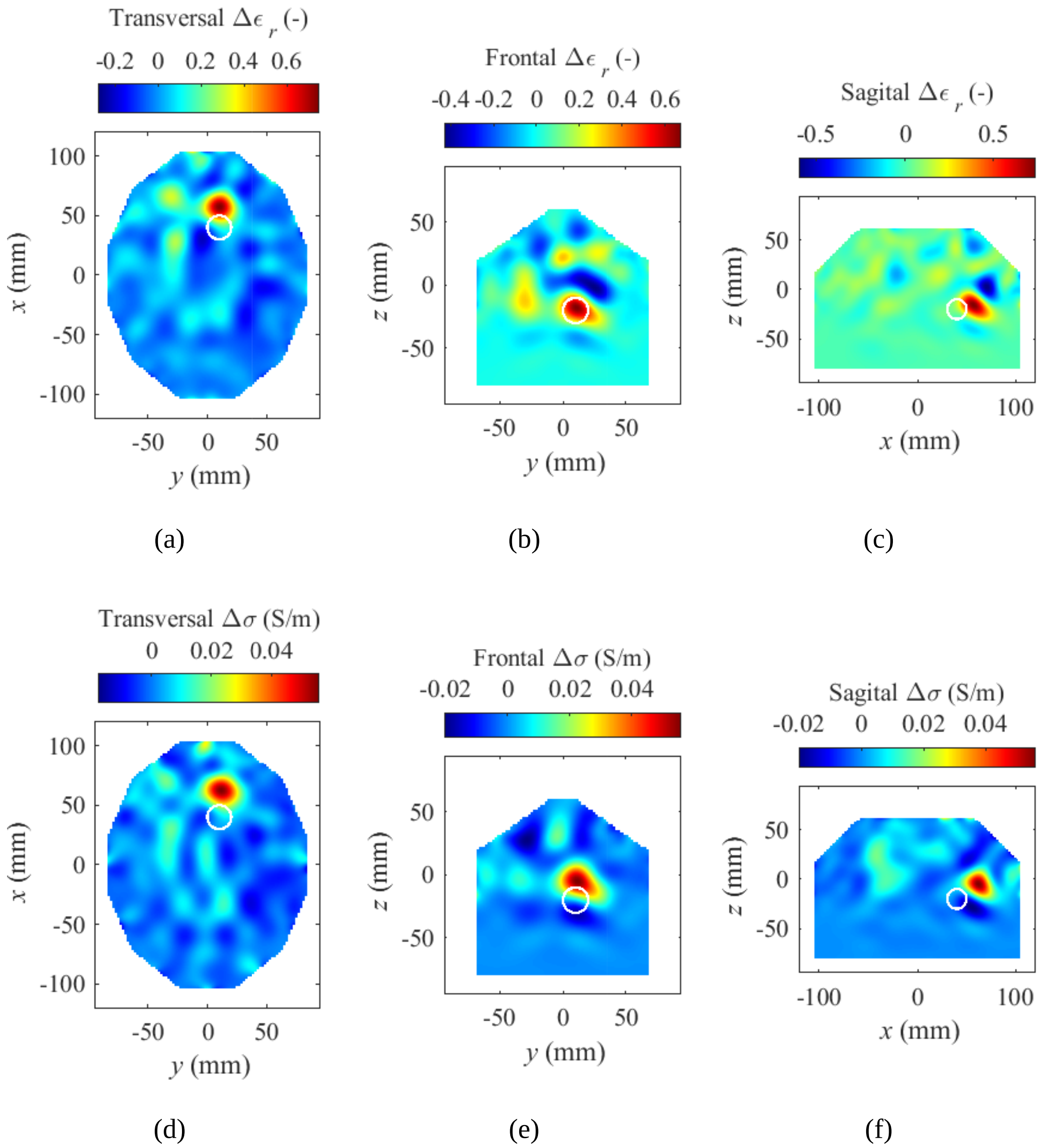

Figure 5.34 Reconstructed differential relative permittivity $\Delta\varepsilon_r$ (-) in (a)-(c) and conductivity $\Delta\sigma$ (S/m) in (d)-(f) for **HEM** stroke phantom on position **P1** with diameter **20 mm**. The slices in anatomical planes leads through maximal detected dielectric contrast. The white circle indicates the expected stroke phantom position. Truncation level $\boldsymbol{N_T}$ **= 200**.

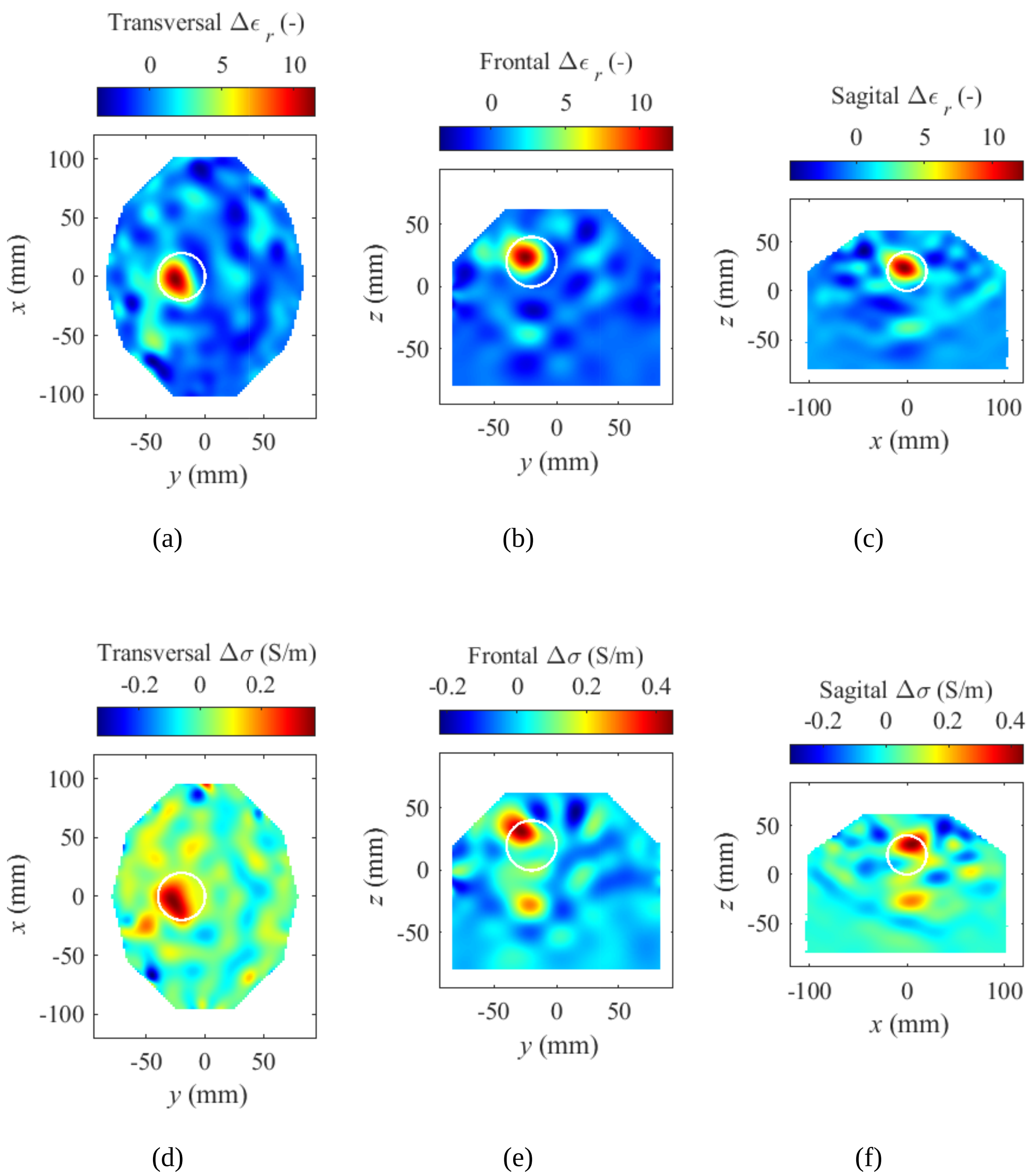

Figure 5.35 Reconstructed differential relative permittivity $\Delta\varepsilon_r$ (-) in (a)-(c) and conductivity $\Delta\sigma$ (S/m) in (d)-(f) for **HEM** stroke phantom on position **P2** with diameter **40 mm**. The slices in anatomical planes leads through maximal detected dielectric contrast. The white circle indicates the expected stroke phantom position. Maximal truncation level $\boldsymbol{N_T} = \mathbf{300}$.

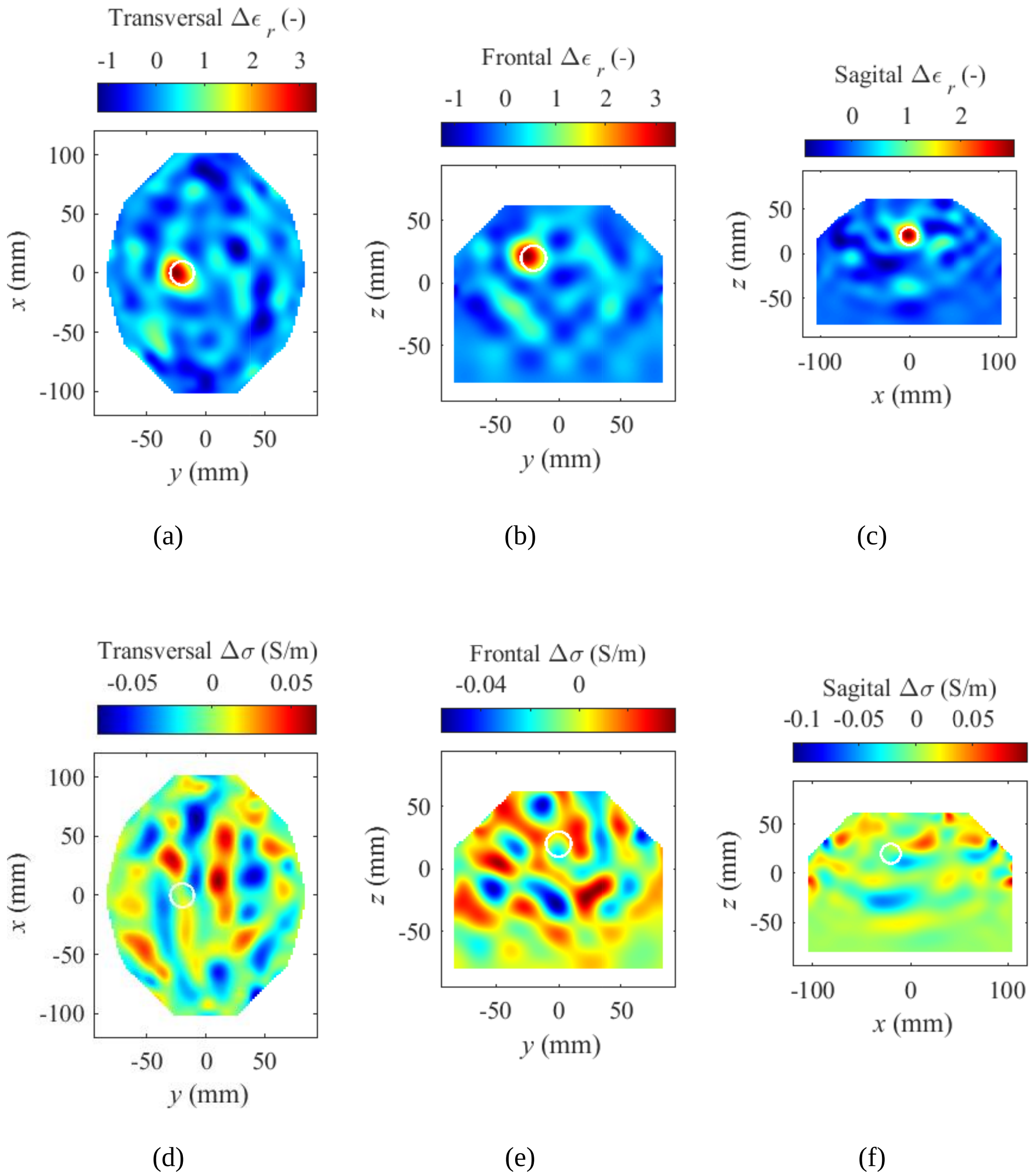

Figure 5.36 Reconstructed differential relative permittivity $\Delta\varepsilon_r$ (-) in (a)-(c) and conductivity $\Delta\sigma$ (S/m) in (d)-(f) for **HEM** stroke phantom on position **P2** with diameter **20 mm**. The slices in anatomical planes leads through maximal detected dielectric contrast. The white circle indicates the expected stroke phantom position. Maximal truncation level $\boldsymbol{N_T}$ **= 300**.

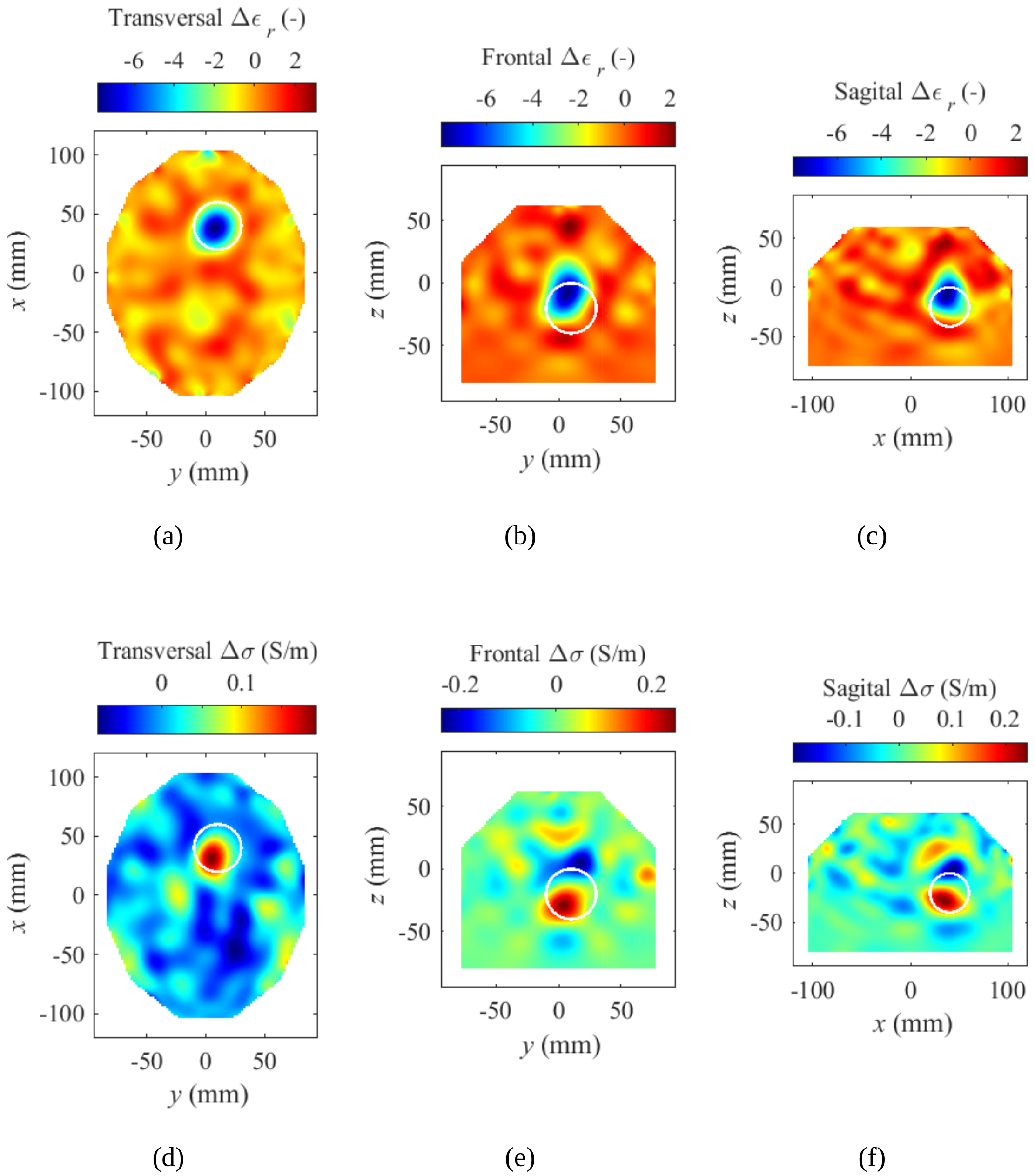

Figure 5.37 Reconstructed differential relative permittivity $\Delta\varepsilon_r$ (-) in (a)-(c) and conductivity $\Delta\sigma$ (S/m) in (d)-(f) for **ISCH20** stroke phantom on position **P1** with diameter **40 mm**. The slices in anatomical planes leads through maximal detected dielectric contrast. The white circle indicates the expected stroke phantom position. Maximal truncation level $\boldsymbol{N_T}$ **= 300**.

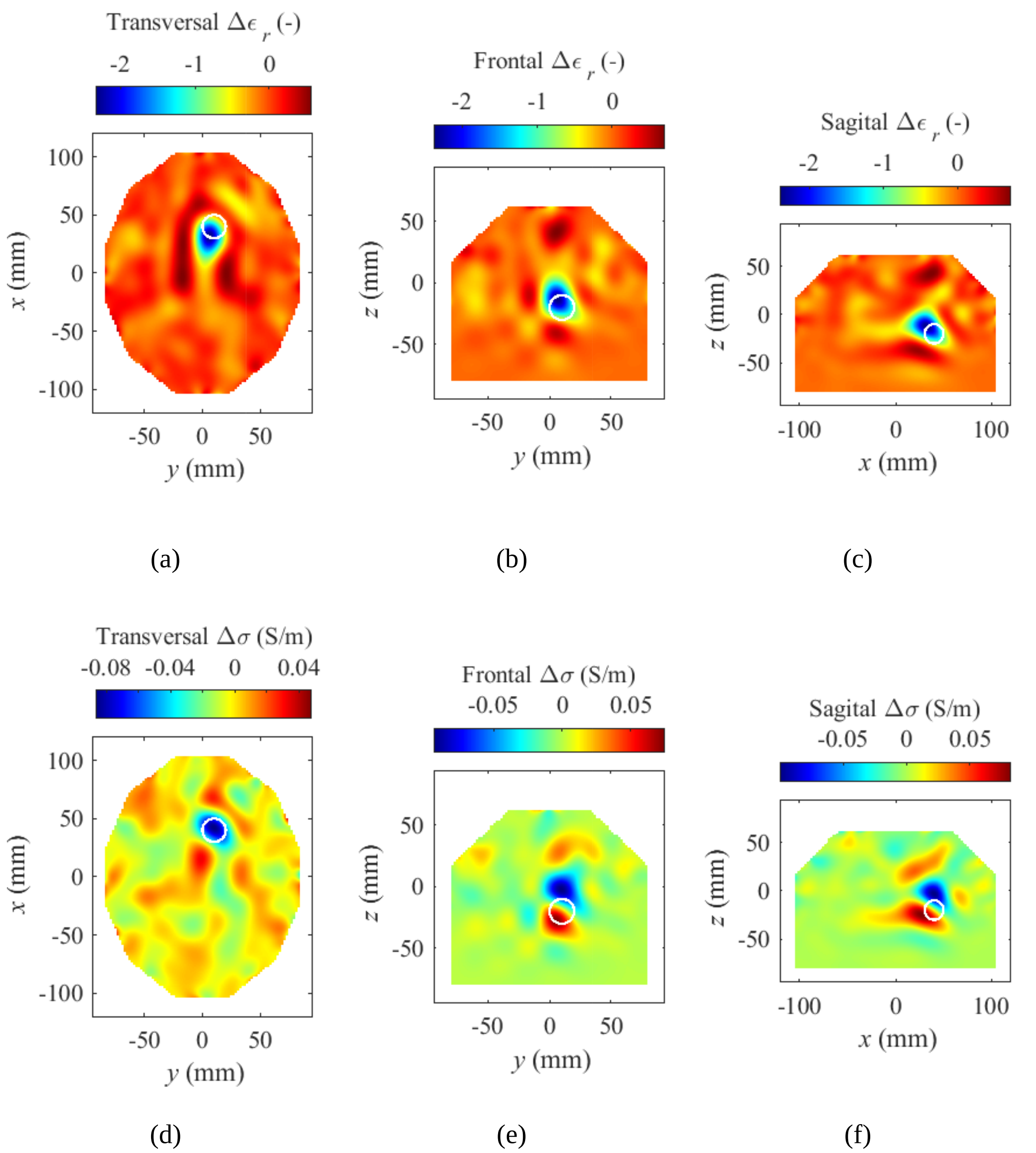

Figure 5.38 Reconstructed differential relative permittivity $\Delta\varepsilon_r$ (-) in (a)-(c) and conductivity $\Delta\sigma$ (S/m) in (d)-(f) for **ISCH20** stroke phantom on position **P1** with diameter **20 mm**. The slices in anatomical planes leads through maximal detected dielectric contrast. The white circle indicates the expected stroke phantom position. Truncation level $\boldsymbol{N_T}$ **= 265**.

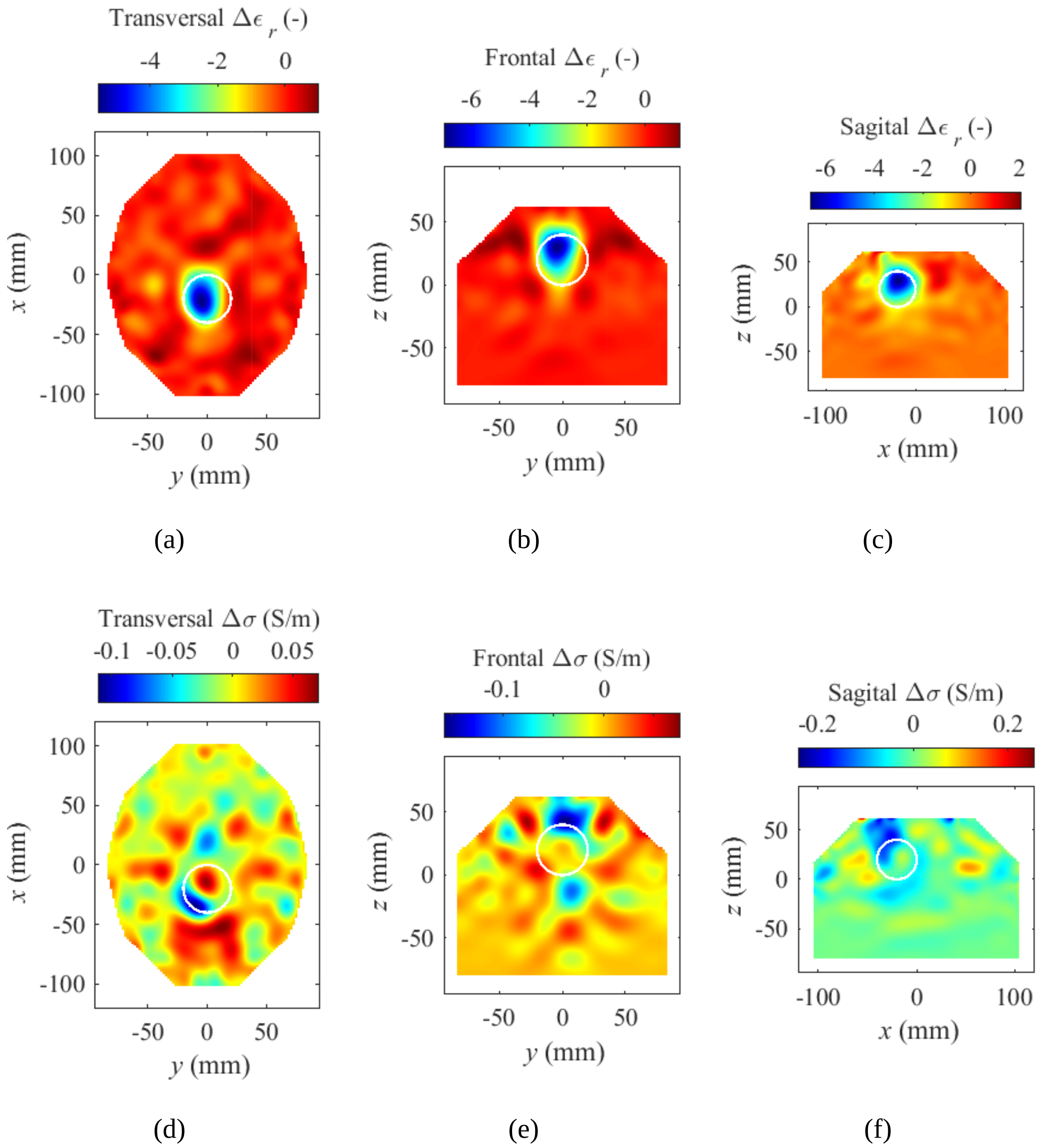

Figure 5.39 Reconstructed differential relative permittivity $\Delta\varepsilon_r$ (-) in (a)-(c) and conductivity $\Delta\sigma$ (S/m) in (d)-(f) for **ISCH20** stroke phantom on position **P2** with diameter **40 mm**. The slices in anatomical planes leads through maximal detected dielectric contrast. The white circle indicates the expected stroke phantom position. Truncation level $\boldsymbol{N_T}$ **= 200**.

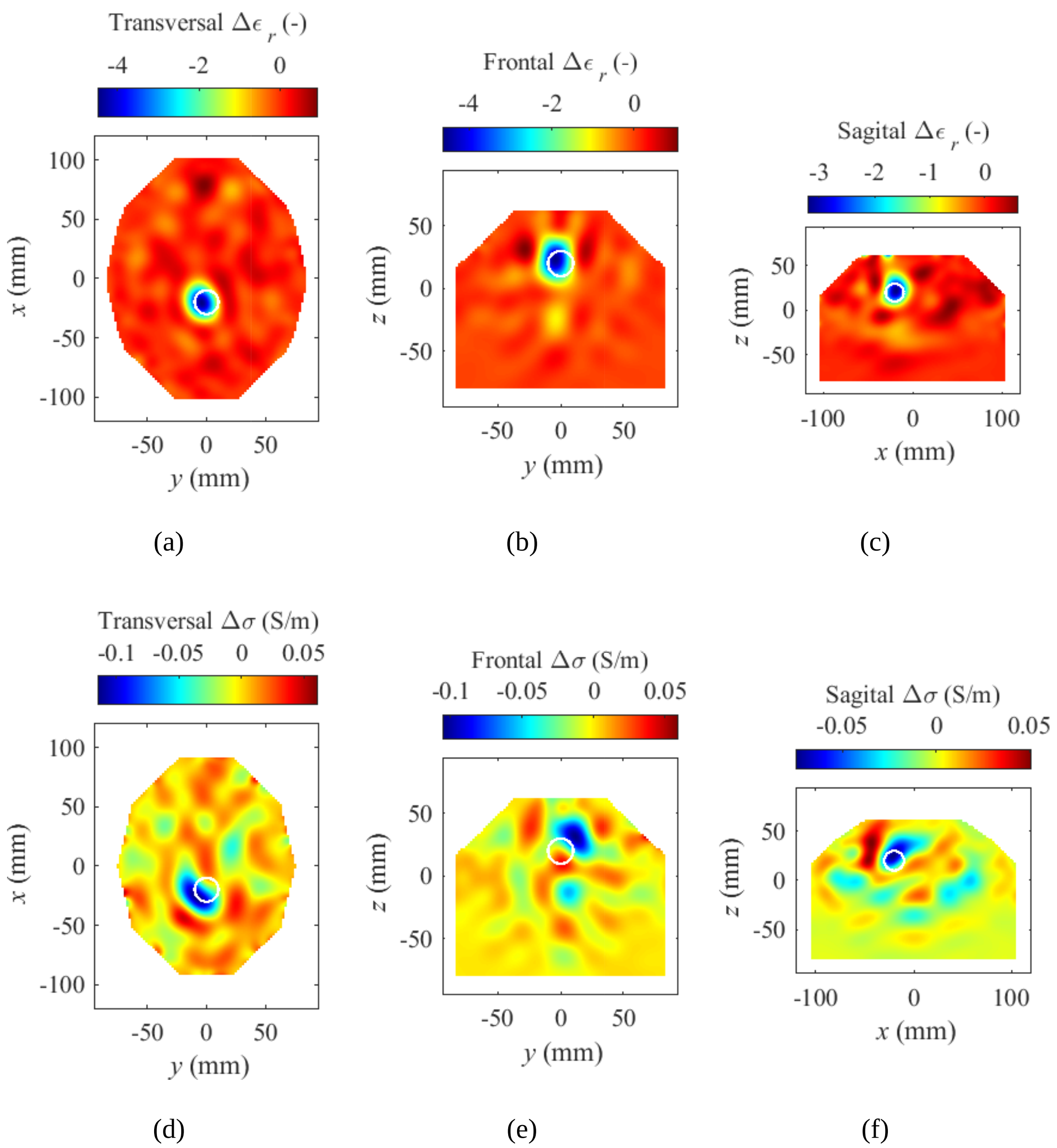

Figure 5.40 Reconstructed differential relative permittivity $\Delta\varepsilon_r$ (-) in (a)-(c) and conductivity $\Delta\sigma$ (S/m) in (d)-(f) for **ISCH20** stroke phantom on position **P2** with diameter **20 mm**. The slices in anatomical planes leads through maximal detected dielectric contrast. The white circle indicates the expected stroke phantom position. Truncation level $\boldsymbol{N_T}$ **= 265**.

Table 5.8 Actual differential dielectric properties δ (measured by coaxial probe) calculated as differences between head phantom and stroke phantoms vs retrieved maximal differential diel. properties Δ using 24-port MWI system.

Type	**HEM**				**ISCH20**			
$\boldsymbol{\delta\varepsilon_r}$ **(-)**	+14,6				-8			
$\boldsymbol{\delta\sigma}$ **(S/m)**	+0,5				-0,2			
Pos.	**P1**		**P2**		**P1**		**P2**	
$\boldsymbol{D}$ **(mm)**	40	20	40	20	40	20	40	20
$\boldsymbol{\Delta\varepsilon_r}$ **(-)**	+7,9	+0,95	+12	+3,3	-8	-2,3	-10	-4,6
$\boldsymbol{\Delta\sigma}$ **(S/m)**	+0,35	+0,07	+0,43	N/A	N/A	N/A	N/A	-0,1

Evaluation of retrieved images

The following tables represents qualitative as well as quantitative parameters of obtained dielectric contrast for different scenarios. Specificity and accuracy are not displayed here as irrelevant parameters regarding the fact that in all images the number of true negative (TN) is always very small (thresholding is limiting the binary mask only on target and input data are without any false targets). In all scenarios the average values of evaluated parameters through all three anatomical planes (transversal, sagittal and frontal) are summarized.

Table 5.9 Qualitative and quantitative evaluation of reconstructed images for HEM stroke phantom type, diameter od 40/20 mm and positions P1 and P2. All presented values are average values from 3 anatomical planes (transversal, sagittal and frontal).

HEM 40mm		Threshold (dB)	Sensitivity (%)	Rel. error (%)	Loc. error (mm)	Area ratio (%)	PSNR (dB)
P1	$\Delta\varepsilon_r$	-6	58	45	[3, 4, 3]	102	12
	$\Delta\sigma$	-6	45	30	[8, 4, 20]	126	11
P2	$\Delta\varepsilon_r$	-6	75	18	[3, 3, 3]	68	16
	$\Delta\sigma$	-3	38	14	[2, 3, 10]	58	-15

HEM 20mm		Threshold (dB)	Sensitivity (%)	Rel. error(%)	Loc. error (mm)	Area ratio (%)	PSNR (dB)
P1	$\Delta\varepsilon_r$	-3	56	93	[10, 1, 2]	127	-4
	$\Delta\sigma$	-3	4	86	[20, 1, 10]	115	2,5
P2	$\Delta\varepsilon_r$	-6	98	77	[2, 2, 1]	214	10,5
	$\Delta\sigma$	N/A	N/A	N/A	N/A	N/A	N/A

Table 5.10 Qualitative and quantitative evaluation of reconstructed images for ISCH20 stroke phantom type, diameter of 40/20 mm and positions P1 and P2. All presented values are average values from 3 anatomical planes (transversal, sagittal and frontal).

ISCH20 40mm		Threshold (dB)	Sensitivity (%)	Rel. error(%)	Loc. error (mm)	Area ratio (%)	PSNR (dB)
P1	$\boldsymbol{\Delta\varepsilon_r}$	-6	47	0	[2, 1, 10]	96	17
	$\boldsymbol{\Delta\sigma}$	N/A	N/A	N/A	N/A	N/A	N/A
P2	$\boldsymbol{\Delta\varepsilon_r}$	-6	76	25	[1, 3, 5]	82	22
	$\boldsymbol{\Delta\sigma}$	N/A	N/A	N/A	N/A	N/A	N/A

ISCH20 20mm		Threshold (dB)	Sensitivity (%)	Rel. error(%)	Loc. error (mm)	Area ratio (%)	PSNR (dB)
P1	$\boldsymbol{\Delta\varepsilon_r}$	-6	83	71	[10, 2, 10]	230	13
	$\boldsymbol{\Delta\sigma}$	N/A	N/A	N/A	N/A	N/A	N/A
P2	$\boldsymbol{\Delta\varepsilon_r}$	-6	92	42	[2, 5, 1]	227	20
	$\boldsymbol{\Delta\sigma}$	-3	38	50	[3, 10, 7]	159	3

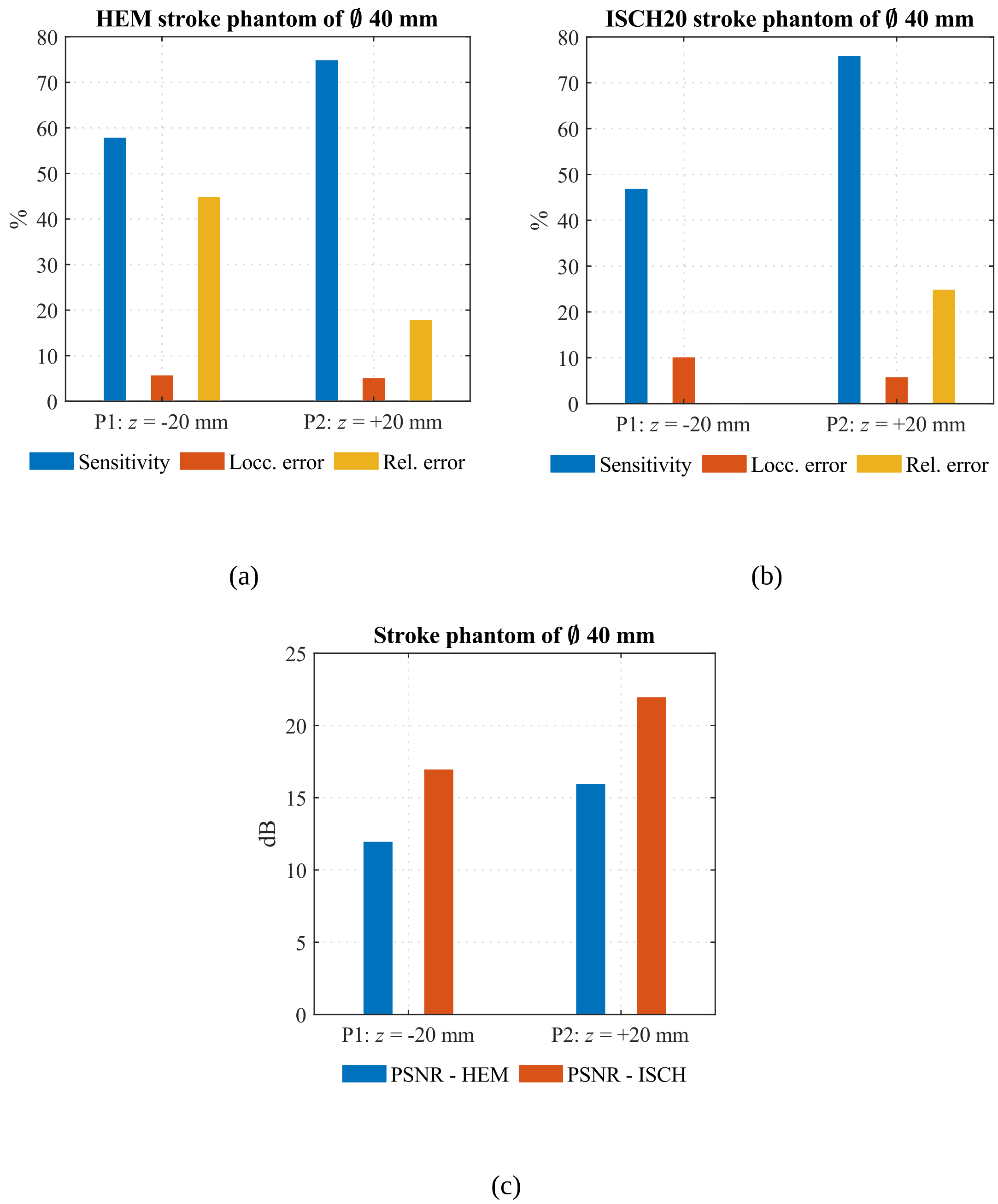

Figure 5.41 Calculated qualitative (sensitivity, localization error) and quantitative parameters (relative error and PSNR) from retrieved differential dielectric contrast of HEM a ISCH20 stroke phantoms at positions P1 and P2 inside MWI system or head phantom, respectively.

Truncation level analysis

It may be noticed that reconstructed differential dielectric profiles presented above were obtained for different values of N_T – truncation level (number of singular values). As described detailed further in Chapter 3, subchapter 3.3.1 – **Truncation level** is the parameter which can significantly influence reconstruction algorithm performance in terms of its accuracy vs stability. Typically, its value is determined individually. Its limited by maximal number of independent S-parameters which can be calculated as $(N+1)\ N/2$ where N is number of antennas in MWI system. The highest number results in achieving the finest retrieved details (contrast). However, the higher level of truncation the lower magnitude (dB) of singular values and it can be affected by measurement noise.

Therefore, we performed the analysis of truncation level based on singular values of retrieved differential object matrix for HEM/ISCH20 stroke phantom of diameter of 40 and 20 mm and position P1, P2. We plotted differential dielectric contrast for relative permittivity, conductivity and magnitude of complex primitivity (Figure 5.43). The truncation levels were determined based on slope change of curve of singular values magnitude (Figure 5.42) [31].

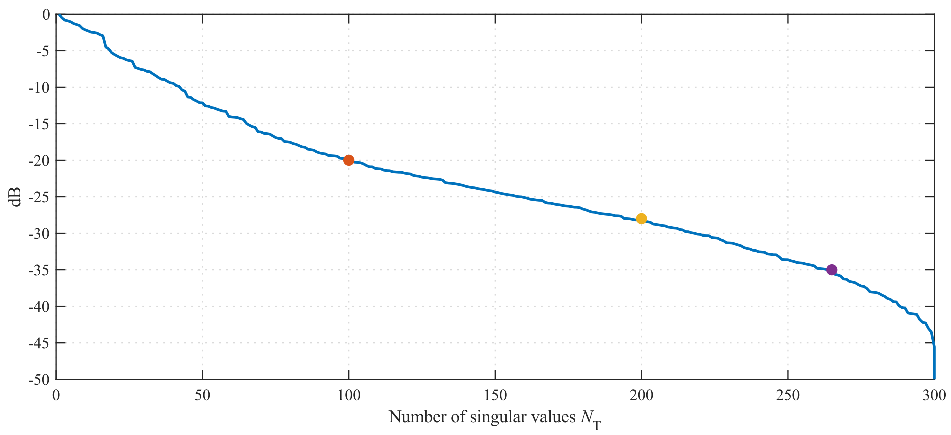

Figure 5.42 Magnitude of singular values (dB) depending on number of singular values N_T

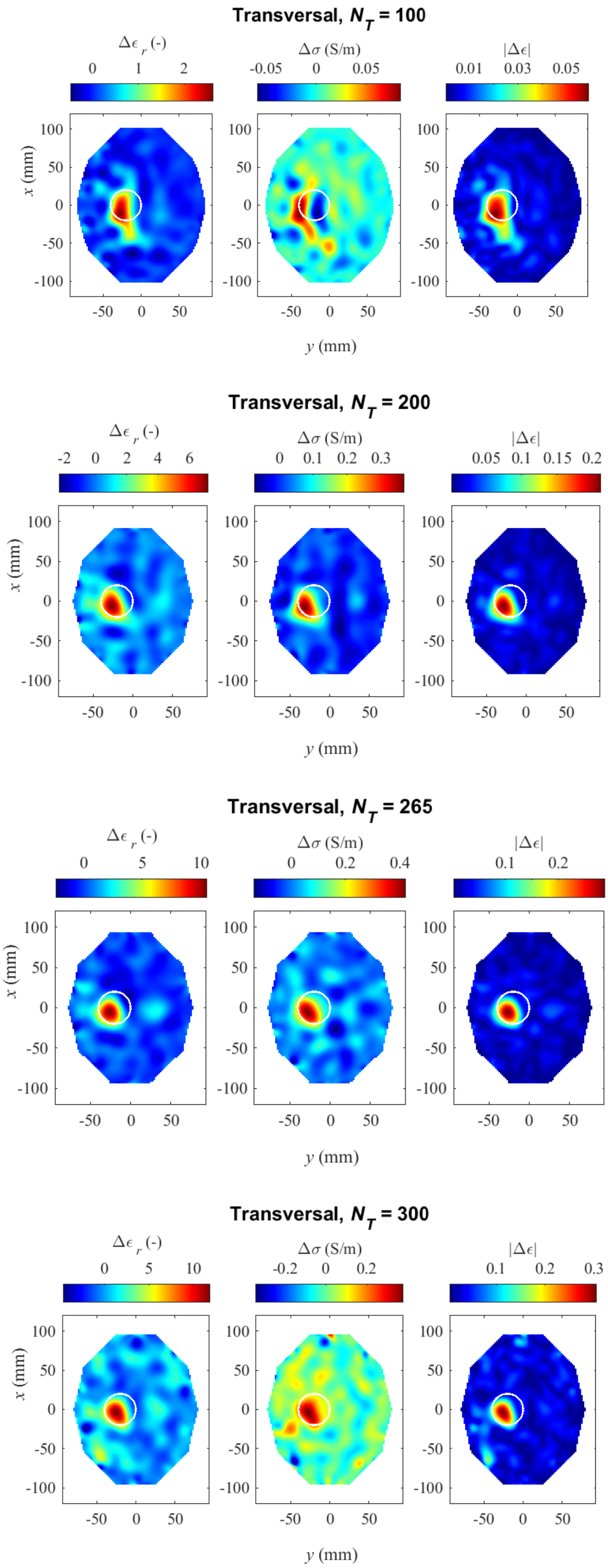

Figure 5.43 Truncation level N_T analysis for 40mm HEM stroke phantom, P2.

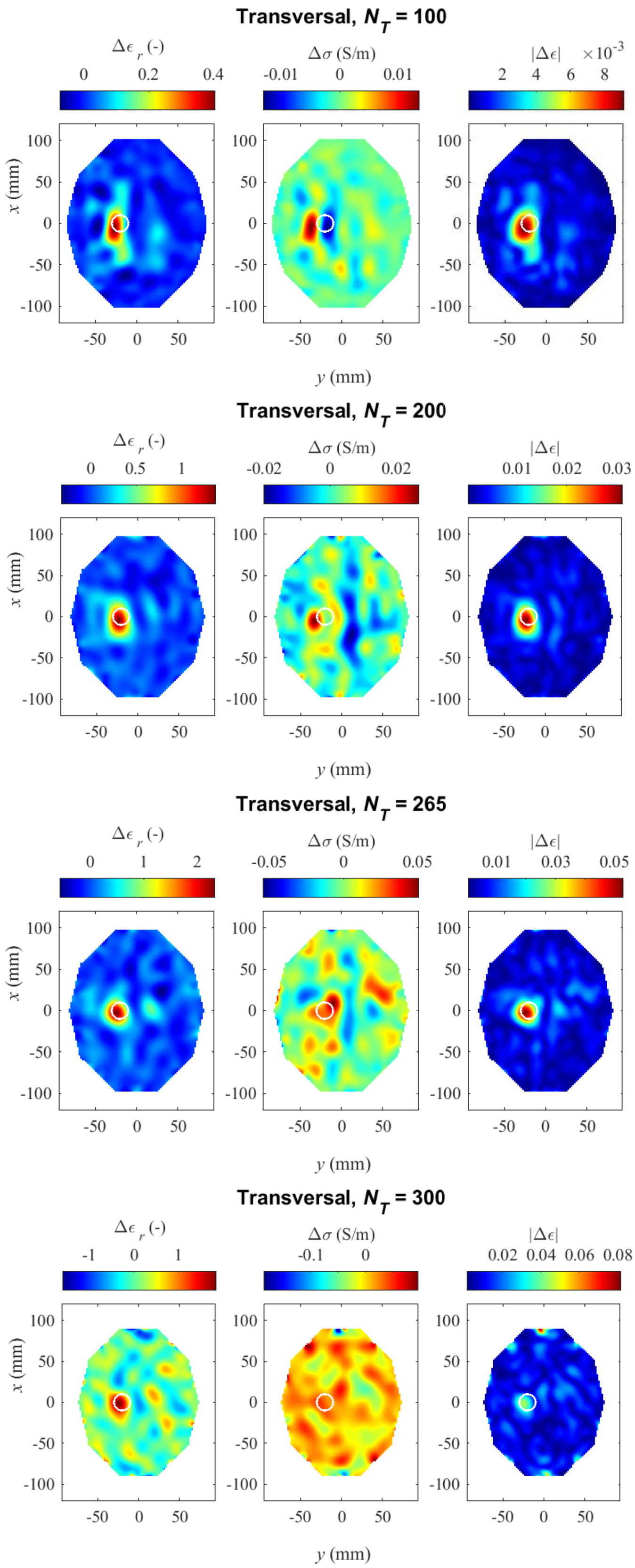

Figure 5.44 Truncation level N_T analysis for 20mm HEM stroke phantom, P2.

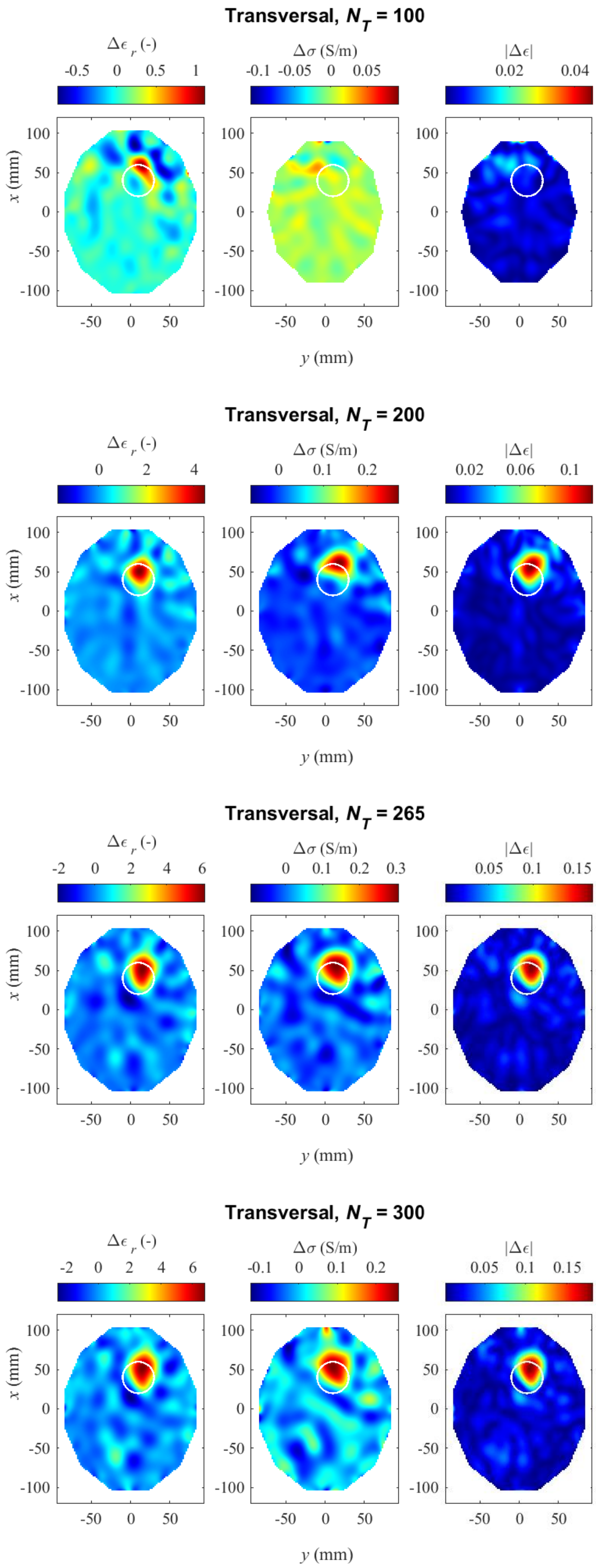

Figure 5.45 Truncation level N_T analysis for 40mm HEM stroke phantom, P1.

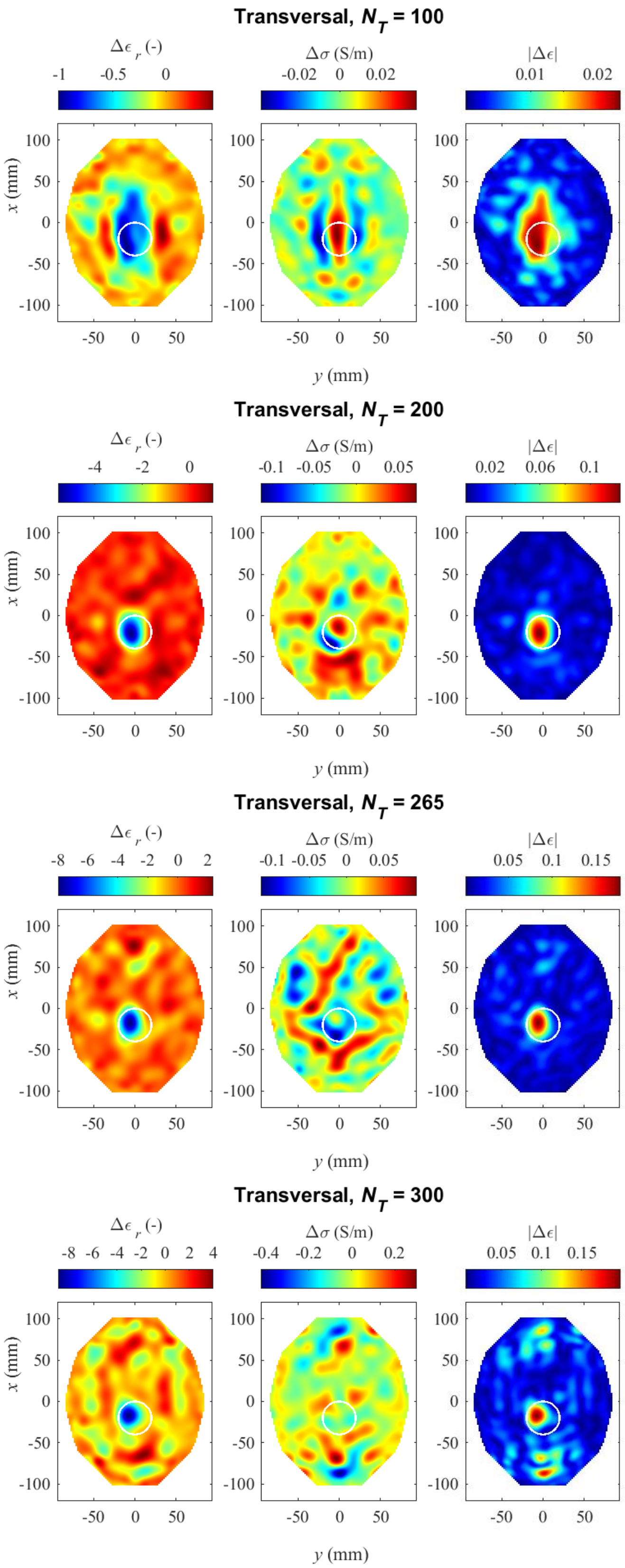

Figure 5.46 Truncation level N_T analysis for 40mm ISCH20 stroke phantom, P2.

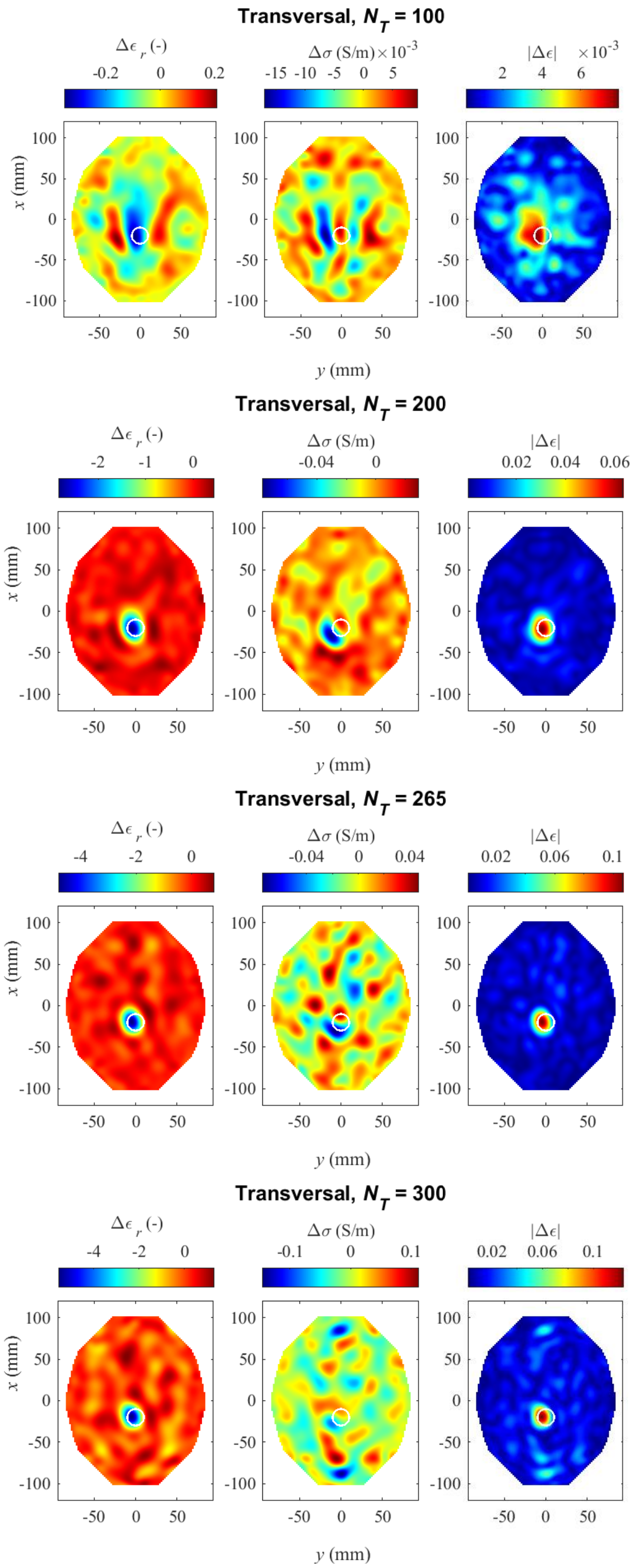

Figure 5.47 Truncation level N_T analysis for 20mm ISCH20 stroke phantom, P2.

From retrieved dielectric contrast for different levels of truncation is obvious that with higher value of N_T the finer contrast is obtained and also the qualitative parameters of the target of interest like size and shape are improved. This correlates with expectation. However, the maximal truncation level 300 for differential relative permittivity images subjectively brings some additional noise (for instance Figure 5.43). In our opinion just the ratio between power of peak contrast and power of background noise is crucial parameter for reliable differentiation of stroke type rather than relative error of retrieved and actual dielectric contrast. For that reason, we also analysed the peak signal-to-noise ratio (PSNR) for different truncation levels. Its values are summarized in Table 5.11.

Table 5.11 Values of PSNR (dB) for different truncation levels N_T of reconstructed differential relative permittivity of 40mm HEM stroke phantom at position P2.

Truncation level N_T	100	200	265	300
PSNR (dB)	2	11,2	14,5	15,3

5.7 Hybrid MWI approach for medical diagnostic and monitoring applications

As mentioned before the microwave tomography (MWT) method uses signal processing in the frequency domain and applies methods capable of estimating the dielectric profile of the scanned region – quantitative images. The radar-based imaging methods process signals in the time domain and can locate dielectric inhomogeneity (scatterers) within a tissue, without the ability to reconstruct the dielectric profile – qualitative images. Radar-based reconstruction algorithms are usually significantly less demanding on computation and time. The basic principle is to transmit ultrawideband (UWB) signals, providing high imaging resolution. The transmitted signal can be formed by short periodically repeated pulses, pseudorandom binary sequences, and so on. Such radar-based systems for biomedical imaging are presented in [69], [70].

By combining these two principles, i.e., the MWT and radar-based imaging, so-called hybrid approach, the **new concept** has been introduced in [71] and is described in this chapter. Hybrid approach can bring significant advantages to the area of microwave imaging-based medical diagnostics, e.g. brain stroke detection or thermometry. Thanks to rapid localization of ROI using radar signals (qualitative information) the area to be imaged can be reduce to less voluminous. This results in two crucial consequences.

(i) First, the precision of quantitative information obtained by linear reconstruction algorithms such as previously used Born/Distorted Born approximation (BA/DBA) can be significantly increased. Especially for 3D imaging the algorithm is applied only on ROI determined by radar. Thus, undesirable false positive targets which often negatively involves retrieved dielectric contrast are eliminated. In addition, the truncation level can be increased which allows to retrieve finer image details. By identifying a ROI this a priori information can be used in forward model and thus speed up its solution.

(ii) Second, the hybrid approach carries new opportunities to the field of non-invasive microwave thermometry in hyperthermia treatment. During hyperthermia the temperature has to be monitored is short time periods. Differential MWI approach using linear algorithms proved the potential as introduced further in Chapter 6. Iterative algorithms could provide higher precision and temperature resolution. Nevertheless, it is high computationally demanding task to obtain temperature distribution iteratively (order of hours) and thus is not feasible for real-time monitoring applications such as thermometry. Introducing hybrid approach the iterative solution in shorter time sequences could be achievable. The radar identifies ROI where the object to be monitored is located. Then each iteration is solved inside the ROI and not in whole imaging domain which can rapidly speed up dielectric profile reconstruction. The huge potential is evident especially for large body parts such as regional hyperthermia in pelvis region.

To prove the concept of hybrid approach we developed and fabricated UWB bow tie antenna operates over frequency bandwidth of 4 GHz while is attached to different standard tissues such as brain, bone, skin ,muscle and water (Figure 5.48). The antenna was fed through symmetrisation balun.

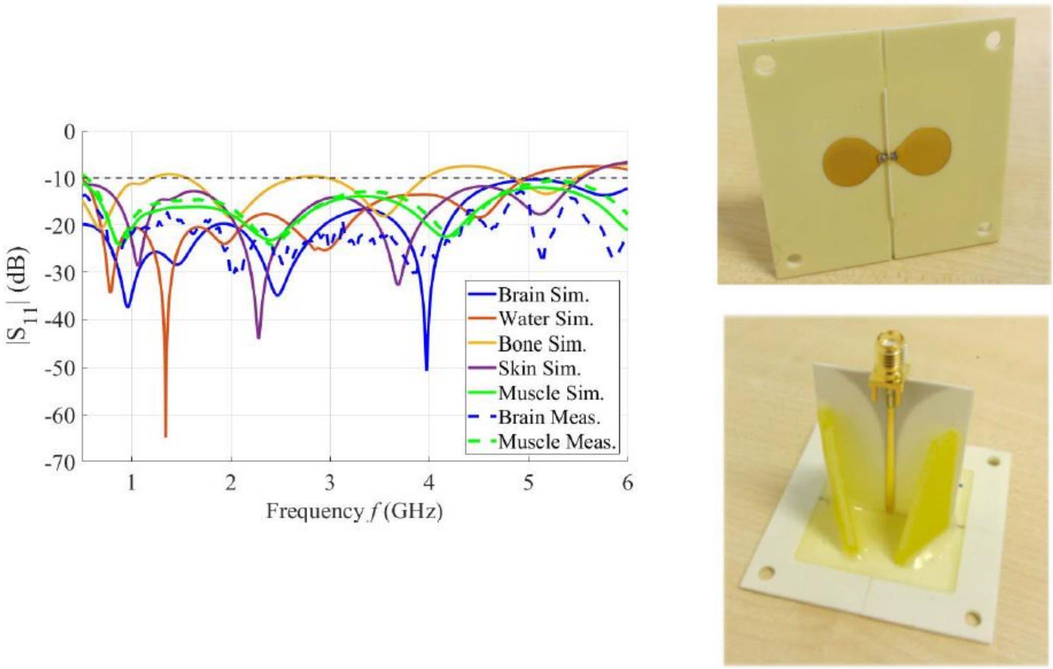

(a) (b)

Figure 5.48 Magnitudes of reflection coefficient of UWB bow tie antenna for different tissues (a), detail of antenna (b).

The UWB imaging system - octagonal container with directly attached antennas and filled with average liquid head phantom was used for testing of hybrid approach as illustrated in Figure 5.49.

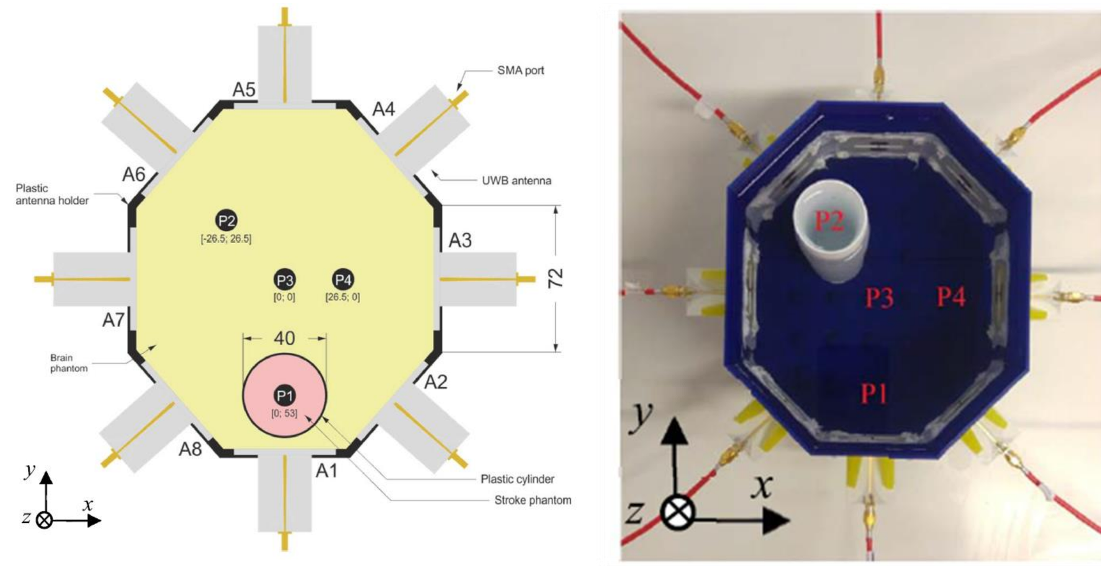

(a) (b)

Figure 5.49 Schematic perspective view on UWB imaging system with marked positions of cylindrical targets (a), photograph of UWB imaging system setup (b).

In the first step the acquired frequency domain signals with and without target using VNA were transformed to time domain by inverse discrete Fourier transform (IDFT). After that, time shift for each captured signal and each focal point was calculated. The "Delay and Sum" algorithm was employed for target position reconstruction representing as normalized intensity in particular focal point as shown in Figure 5.50. Then the ROI can be identified (purple dashed rectangle). In the second step the computed electric fields by forward model only from ROI and measured frequency domain signals are used for reconstruction of differential dielectric profile as presented in Figure 5.51.

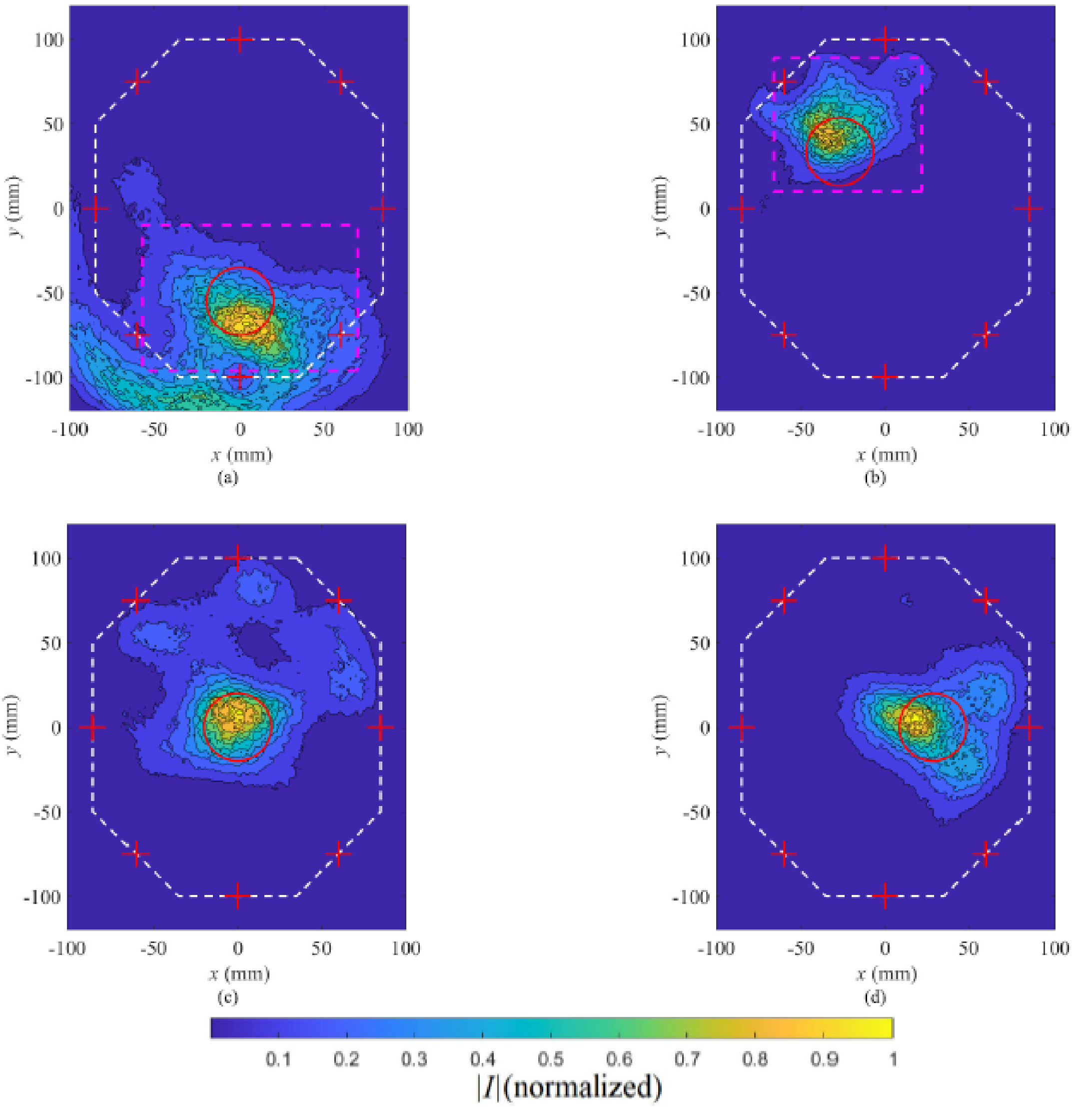

Figure 5.50 Reconstructed scattering profile (normalized intensity |I|) of liquid brain phantom with inserted cylindrical-shaped dielectric target. The position (P1–P4) of the target is marked by the red circle. (a) Corresponding to the target position P1. (b) Position P2. (c) Position P3. (d) Position P4. The antennas positions are marked by red crosses. The inner container boards are marked by the white-dashed line. The ROI is marked by purple-dashed rectangle.

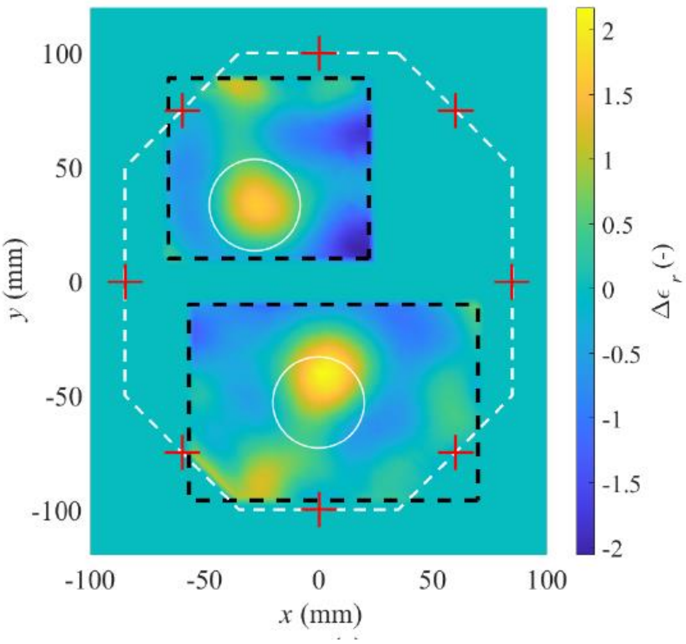

Figure 5.51 Reconstructed differential relative permittivity of liquid brain phantom with inserted cylindrical target inside the ROI (black-dashed rectangle) identified by radar-based imaging. The frequency of 1 GHz was employed. The true position of the target P1 and P2 is marked by the white circle. The antennas positions are marked by re d crosses. The inner surfaces of the container walls are marked with a white-dashed line.

In Figure 5.51 can be noticed that the range of reconstructed differential relative permittivity varies from approx. negative 2 to positive 2 and thus it would not be possible to exactly determine which contrast is true positive and which false positive. However, employing the hybrid approach the region of true target is clearly identified and therefore it can be reliably decided that the true target was the one with positive retrieved dielectric contrast approx. **+2,2**. The actual contrast measured by commercial dielectric probe was **+1,56 units** of relative permittivity between head and target phantom. The reconstruction process was also **speed up by approx. 20 %** due to hybrid approach.

5.8 Chapter conclusion

Among other things, this chapter introduced the development process and experimental validation of an antenna element suitable for a multichannel Microwave Imaging (MWI) system. The imaging system underwent both numerical and experimental validation, focusing on methodical testing for brain stroke detection using homogeneous and realistic 3D head phantoms. The strengths as well as limitations of the MWI system for brain stroke follow-up were identified and are discussed in the subsequent paragraphs, along with future perspectives for this diagnostic application.

5.8.1 Bow tie antenna and prototype of MWI system

Very first promising results were obtained using 8-port prototype of MWI system. Nevertheless, in some scenarios the prominent signal, and thus reconstruction distortion was recorded. Our assumption was focused on the insufficiency of used antenna elements which are, in our opinion, the crucial part of the MWI system. The insufficiency mainly in terms of asymmetric antenna feeding and nondirectional antenna radiation. Both of the mentioned parameters increased the antenna mutual cross coupling through surroundings, and thus eliminated the useful signal transmitting through the investigating domain.

5.8.2 Numerical analysis of various antenna elements

Due to the mentioned reasons, in Subchapter 5.4 we provided an extensive numerical analysis of different antenna types including bow tie, double-layered slot, and waveguide-based antenna. In the first part of analysis the antenna sensitivity to dielectric contrast (increase-HEM and decrease-ISCH of dielectric properties of stroke phantom placed inside the head phantom) and diameter of stroke phantom were performed. The absolute differences in the transmission coefficient of each antenna were compared where the **slot** and the bow tie antenna showed the highest and consistent changes in the transmission coefficient.

Also, the differences in transmission coefficient for various stroke phantom diameters for the slot and bow tie antenna quadratic with a correlation coefficient of over 99 %, not for the waveguide-based antenna. In the next stage of analysis, we proposed a completely **new method** for studying antenna radiation characteristics in the near-field region and in lossy mediums. Since the radiation pattern is defined only for far field region and surroundings of air, this new suggested method became a very valuable tool for description of antenna radiation and directivity. The slot antenna reached around **80 %** lower backward radiation compared to bow tie antenna. In addition, showed completely symmetrical near-field pattern versus the bow tie.

5.8.3 H-slot antenna design and experimental validation

Based on the results of numerical analysis from Subchapter 5.4 we developed a new compact, small-sized H-slot antenna with symmetrical feeding and ground plane. The main goal of the antenna design process was to minimise its geometry as much as possible and at the same time preserve impedance matching, unidirectional forward radiation, and eliminated backward radiation. The H-slot antenna showed similar performance compared to the previous introduced slot antenna and behaves much better than the bow tie. Its backward radiation was suppressed around **60 %** compared to bow tie. This corresponds to by **20 %** lower values than for the slot antenna. It was caused by the small size of the antenna (30 by 30 mm), respectively by the smaller distance of the H-slot from the edge of the antenna substrate. On the other hand, the compact small size of antenna allows its use in multichannel MWI system, the slot shape of H can be easily parametrized and due to its rectangularity, it is suitable for numerical EM field simulators based on FDTD which can be accelerated using GPUs.

5.8.4 Multilevel 24-port MWI system

The new generation of 3D 24-port MWI system proved together with implemented reconstruction algorithm very good sensitivity to differentiate between HEM stroke phantom and ISCH stroke phantom in all 3 anatomical planes sliced through head phantom (transversal, sagittal and frontal). In each scenario the system was able to identify stroke phantom position typically with sensitivity around **70 %,** relative error at maximum **25 %,** low values of localization error (circa **6 mm**) and positive PSNR in rage from **12** to **22 dB.** These parameters were valid for stroke targets of diameter of 40 mm and differential relative permittivity (Table 5.9 and Table 5.10).

The retrieved dielectric contrast based on differential electrical conductivity was very poor especially for **ISCH20** stroke phantom where always the differential contrast to positive as well as negative values appeared (Figure 5.37, Figure 5.38). Thus, the stroke phantom type determination was not possible. The relative actual change of conductivity reached lower values than the relative permittivity and thus the conductivity could be masked and distorted.

<u>Stroke phantom diameter</u>

When the diameter of target was decreased to **20 mm** which is the theoretical spatial resolution limit of given method at frequency of 1 GHz and inside the medium of relative permittivity 45, the results showed following (Figure 5.36, Figure 5.40, Table 5.9,Table 5.10):

- The objects with size close to spatial resolution limit are detectable but with higher relative error and only for specific conditions such as position P2 (+20 mm) independently on stroke phantom type.
- The area of retrieved target is about 100 % larger than actual target – it induces the distortion of sensitivity to values above 90 %.
- PSNR was preserved around 20 dB.

Stroke phantom position

The 3D antenna layout together with H-slot antennas showed to be very valuable compared to previously obtained 2D scans. The position P2 (inside the MWI system enclosed with all antennas) compared to P1 (at the level of bottom antennas) proved significant improvements of the qualitative and quantitative parameters. Sensitivity **increased by 20 %,** relative error **decreased by 20 %** and PSNR **increased by 4 dB** (Table 5.9).

Moreover, if we compare these 3D reconstructions with the previously obtained 2D reconstructions (subsection 6.3), we can conclude that there is an increase in quality, which we attribute mainly to the H-slot antennas and their key feature: weak back radiation and thus higher resistance against noise. The reconstructions could be imaged in whole investigated domain and not only in limited region around the stroke phantom position, no artefacts related to false positive targets were observed here.

Truncation level

As described in Chapter 3 the reconstruction algorithm used here in the thesis is based on TSVD regularization scheme. Therefore, the singular value truncation level is the crucial parameter for obtaining the true dielectric contrast. The expectation is that with decreasing amplitude (dB) of singular values or increasing number of singular values, respectively, the retrieved contrast will improve (relative error will be lower) as well as shape (sensitivity will be higher) and centre position of target, but stronger effects of noise will appear (PSRN will decrease). This assumption was not confirmed for all scenarios. For 40 mm targets we were always able to retrieve the high quality images with maximal **truncation level 300** (equal to amplitude of singular values around – 50 dB) where the noisy background visually appeared **but PSNR was preserved above 10 dB.** The lower amplitude of singular values around – 35 dB/-25 dB (truncation level 265/200) had to be used for scenarios of 20 mm targets and also for some 40 mm ISHC20 stroke phantoms to obtain satisfying PSNR. In experimental study of Vasquez et.al. [31] they concluded that optimal for their setup was amplitude of singular values -21 dB as trade-off between stability, noisy background and accuracy. For higher values they commented that VNA with higher dynamic range should be used, or more stable head phantom fabricated.

In our study we were able to use amplitude of singular values at minimum –25 dB and at maximum -50 dB for majority number of scenarios. This proves that our experimental setup provided less noisy data. On the other hand, more realistic phantom with calf brain was employed in the mentioned study. So, validation of our settings and whole MWI setup on anatomically and dielectrically realistic head phantom is still awaiting.

5.8.5 Hybrid MWI approach for medical diagnostic and monitoring applications

We introduced a completely new concept for microwave-based brain stroke detection in the Subchapter 5.7. The results from Subchapter 5.6.2 showed some limitations of used MWI system and reconstruction algorithm to detect stroke phantom based on retrieved differential electrical conductivity. The false positive local changes of contrast were identified in some scenarios. To eliminate this false positive targets in reconstructed images we suggested so-called Hybrid MWI approach where the radar-based imaging and differential MWT is combined. Using the radar the qualitative information about target position is obtained. After that the ROI around the target is selected and MWI algorithm retrieves the contrast only in that ROI. This can lead to **elimination of false targets** and also to speed up the algorithm by **20 %**. For the purpose of the measurements the new UWB antenna was developed, operating at the frequency band of 4 GHz and virtually attached to common human tissue phantoms such as bone, skin, brain, muscle or water.

6 CHAPTER: NON-INVASIVE REAL-TIME MICORWAVE THERMOMETRY FOR HYPERTHERMIA

This chapter is based on [A4] and on work carried out during Short-Term Scientific Mission (STSM) at Chalmers University of Technology, Department of Signal processing and Biomedical Engineering, Biomedical electromagnetics group under supervision of assoc. prof. Hana Dobsicek Trefna, time period from January till end of May 2020. The STSM was supported by COST Action CA17115 - European network for advancing Electromagnetic hyperthermic medical technologies. The publication [A4] was supported by ICT Conference Grant within mentioned COST Action.

6.1 Introduction

Hyperthermia (HT) is a therapeutic method inducing a controlled temperature elevation of 40 to 44 °C in a tumour for the time period of 60 - 90 minutes. In order to achieve full potential and treatment efficacy, temperature control in the treated region is crucial. Accurate thermometry is thus an important part of the HT systems. The gold accurate and fast standard of temperature distribution monitoring are optic fibre probes. However, these probes are inherently invasive (see Figure 6.1) and limited to information only from tip of the sensor which is very inadequate especially for strongly heterogeneous regions like for instance head and neck region. The optic fibre probes can typically provide spatial temperature resolution better than 1°C [72].

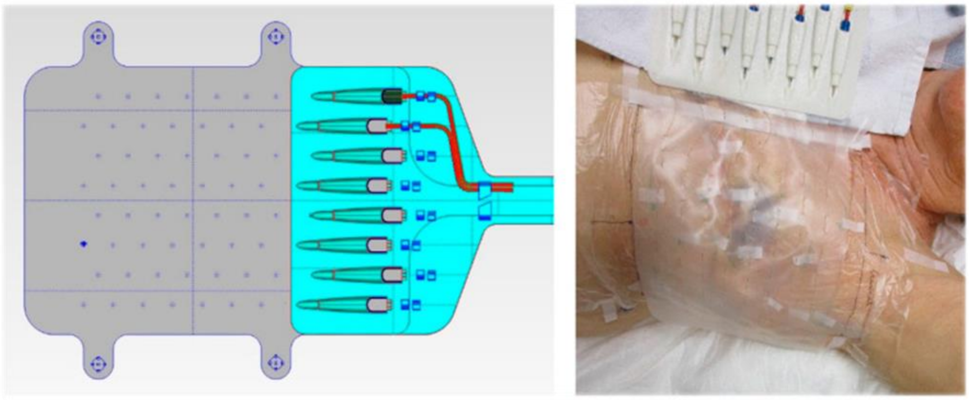

Figure 6.1 The left picture is a schematic drawing of the thermal monitoring sheet with eight seven-sensor thermocouple invasive probes. The right picture shows a real photograph on the chest wall of a study patient. Adopted from [73].

Currently, only magnetic resonance (MR) systems are clinically used to achieve a non-invasive, 3D temperature monitoring during HT treatment with spatial resolution reaching 0,5 °C [74]. The most common used method is Proton Resonance Frequency (PRF) MR thermometry which utilizes fact that the resonance frequency of water protons decreases with increasing temperature approx. 0.01 ppm/°C [75]. Typical reconstructed temperature profile is created by acquiring phase maps of tissue before and after heating. These two maps are subtracted, and final phase-change map indicates voxels which are proportional to the change in temperature as shown in Figure 6.2.

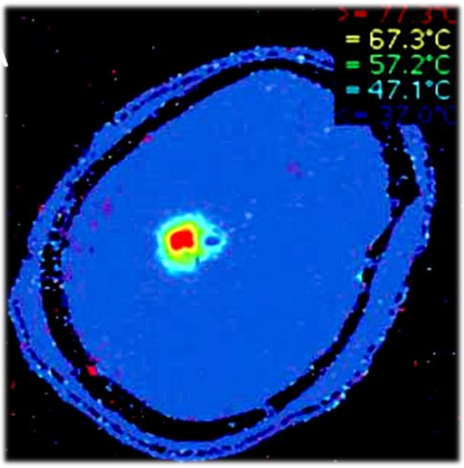

Figure 6.2 PRF MR thermometry image of a brain tumour underwent the laser ablation [76].

In view of some parameters such as: 1) lower speed and data acquisition, 2) cost, and availability 3) dimensions, 4) low sensitivity to motion artifacts, the development of new methods is desirable. In addition, the MRI compatible HT applicators need to be used. Due to the temperature dependence of dielectric parameters of biological tissues demonstrated for example by Ley et al [77], Microwave Imaging (MWI)/Microwave Tomography (MWT) is a technique with such a potential.

The very first potential of capability of microwave tomography for thermometry were demonstrated by Mallourquí et.al. in 1992 [78] on synthetic numerical data. The study identified a few essential findings: (i) a system with high repeatability and dynamic range 100 dB is required, (ii) the BA algorithm has worked for homogeneous mediums, (iii) the optimum frequencies and coupling mediums have been estimated.

In late 90's Chang et. al. [79] conducted first experimental multifrequency measurements using monopole antenna array around the heated 5cm tube filled with different concentrations of saline solution. The results showed that monitoring of temperature changes of saline solution using near-field MWI is feasible reaching mean precision of 2 °C reconstructed by iterative algorithm such as Gauss-Newton optimization. This experiment was repeated by Meaney [80] in in early 2000's but the saline tube was surgically inserted inside the pig torso together with fibre optic probes while the torso was whole submerged in plastic tank filled with saline solution. The multifrequency analysis for 700, 800, 900, 1000 MHz and different temperatures of saline tube (33, 36, 39, 42, 45, 42, 39, 36 and 33 °C) was addressed. The iterative approach utilizing the log-magnitude/phase (LMPF) minimization algorithm has been used. The recovered values of relative permittivity did not corelate with the saline tube temperature increase/decrease for any frequency. The recovered conductivity values for the heated tube exhibit significant correlation with temperature for all frequencies. The mean temperature accuracy for all frequencies was found to be 1,45 °C.

The potential of the differential MWI for thermometry was demonstrated experimentally also by Haynes et al [81]. In this work, the trend of temperature changes of heated spherical water-filled object inside developed MWI system was successfully monitored during native cooling process from 55 to 25 °C. The BA and SVD were employed, and absolute values of differential object function was imaged.

The pixel intensity of absolute differential object function in the centre of detected object corelated with temperature change over time with STD 0,6 %. The object function was not separated to relative permittivity and conductivity and thus the exact temperature of object was not estimated based on change of both parameters.

Differential microwave thermometry based on numerical data proved very promising results in study of Aram [82] or Chen [83] et. al. Iterative reconstruction approach was demonstrated on numerical 3D model of breast tissue by Onal et.al. [84]. Nevertheless, verification of various reconstruction algorithms in experiments and clinically more realistic scenarios where object to be imaged is going to be heated and not natively cooled by surrounding phantom/coupling medium is still awaited.

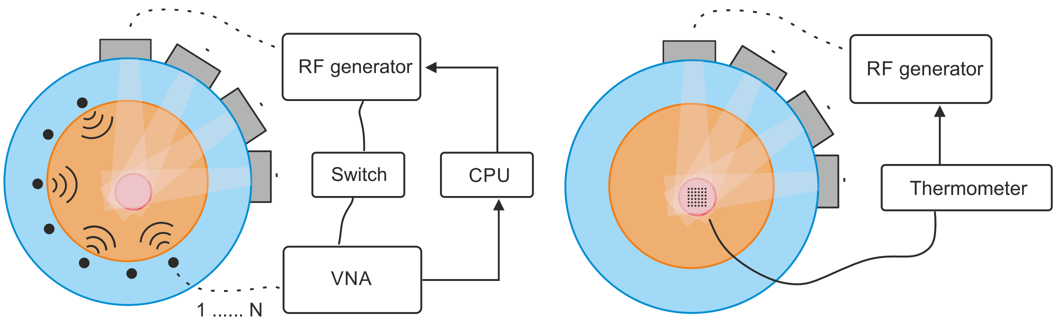

(a) (b)

Figure 6.3 Conceptional scheme of HT system combined with MWT system (a) where is water bolus – blue, tissue – orange, heated tissue region – red, HT applicator – grey, MWT antennas – black. Typical HT system with invasive thermocouples inside the heated region (b).

6.2 Main aim of the chapter

We explored the feasibility of the differential microwave imaging approach and capability of linear reconstruction method (BA/DBA, TSVD) to follow the change in temperature of the target during a cooling/heating process. The main aim was to prove that these methods could be very promising way to monitor non-invasively and in rea-time temperature distribution during hyperthermia treatment and identified the temperature resolution achievable by differential MWT. The assumption was to detect the difference of 2 °C. In the first part of the chapter, we investigated the temperature dependency of dielectric properties of different materials such as distilled water, saline solution, or muscle phantom. Next, we evaluated numerically as well as experimental capability of already designed and in laboratories of Chalmers University available 16-port monopole MWI system for microwave thermometry. Last but not least the HT system designated for head&neck region treatment was undergone testing of potential use not only for hyperthermia but also for differential MWI.

6.3 Temperature dependency of dielectric properties

Before designing of experimental setup for differential microwave-based thermometry the temperature dependency of dielectric properties of selected materials had to be verified. The human body weight is consisted of 60 % of body fluid or water, respectively. Due to that fact water could be considered as ideal material to be heated and then monitored by MWI system in terms of dielectric properties variance. In the first iteration we measured the dielectric properties of distilled water for temperature range from 24 to 50°C with step of 2 °C in frequency band from 0,5 to 1,5 GHz. We employed open-ended coaxial reflection probe technique by Agilent 85070E (Keysight, USA) and VNA Agilent PNA-L (Keysight, USA). The measurement setup is schematically illustrated in Figure 6.4. The measured trends were compared with Ellison's model as shown in Figure 6.5.

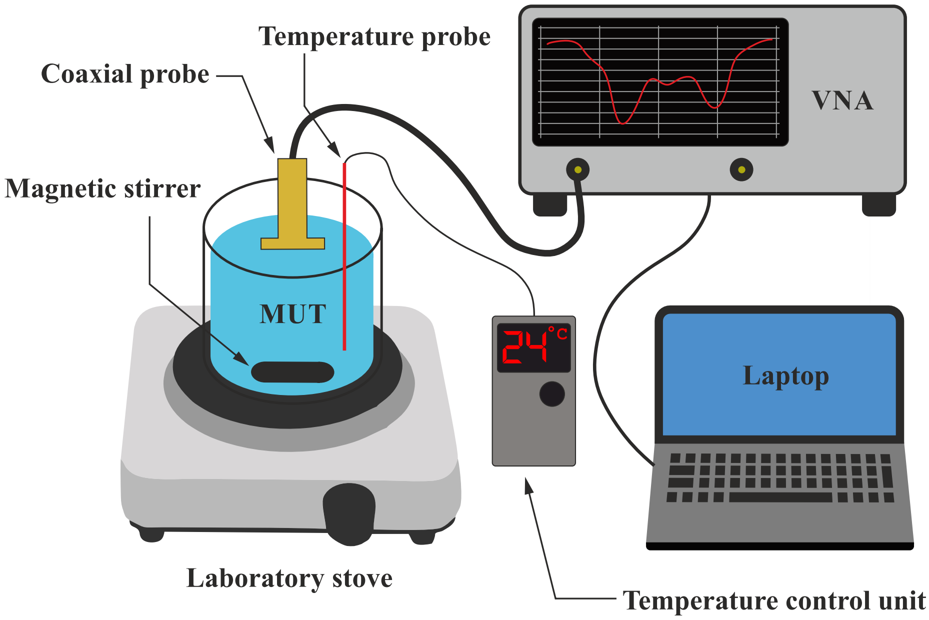

Figure 6.4 Setup for measurement of thermal dependency of dielectric properties of MUT (Material Under Test).

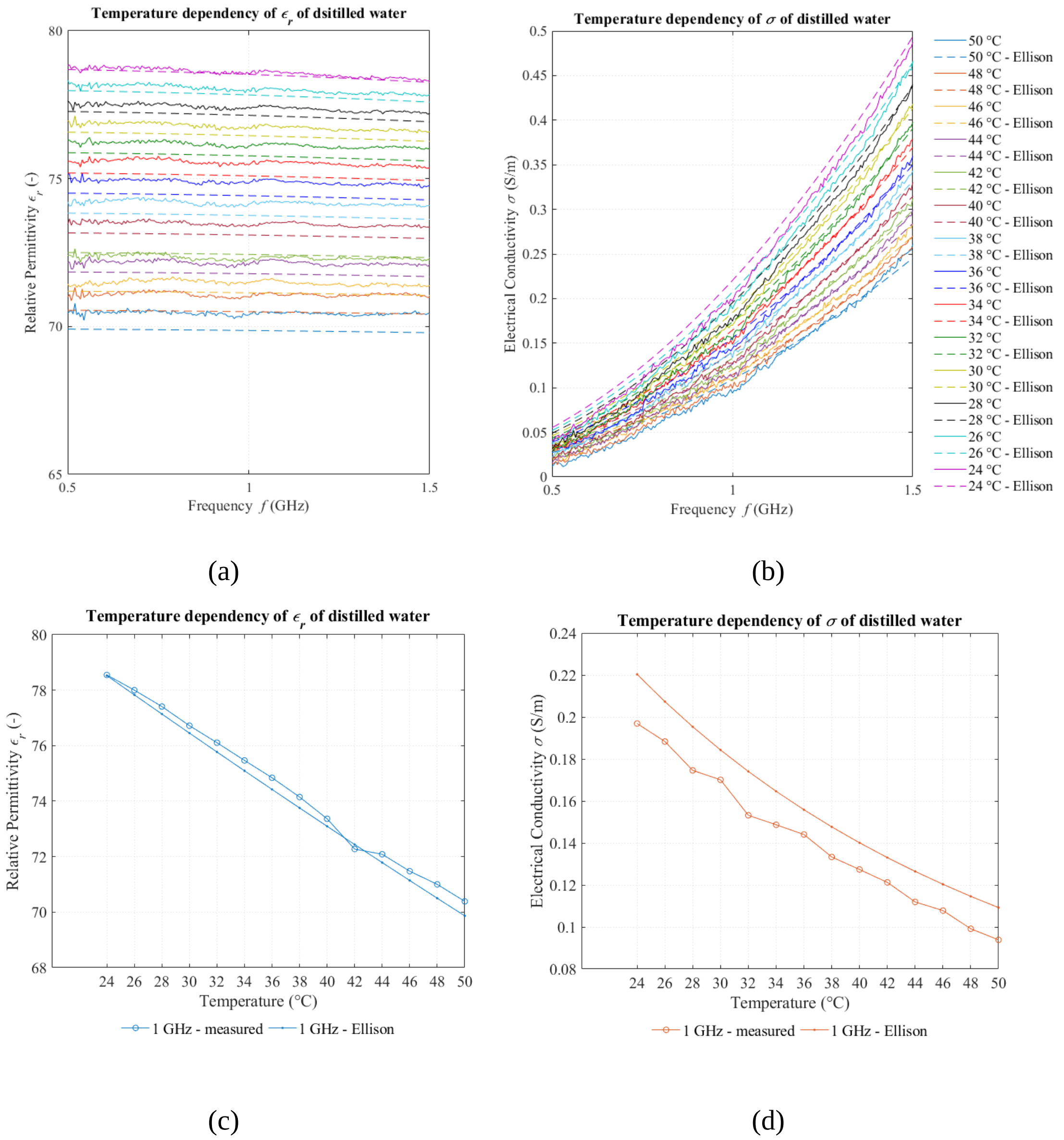

Figure 6.5 Measured temperature dependency of relative permittivity (a) and conductivity (b) of distilled water and its comparison with Ellison's model. Change of both dielectric parameters depends on temperature for single frequency of 1 GHz (c) and (d).

The change of relative permittivity for distilled water is equal to approx. 0,3 and conductivity 0,004 S/m per 1°C at frequency of 1 GHz. Permittivity proved linear dependency on temperature while conductivity changes non-linearly. The conductivity change is very low and could be bellow contrast resolution ability of MWI technique. Therefore, it could be beneficial for experimental microwave thermometry to use the 0,9% saline solution as presented earlier by Meaney [80]. The solution is very much similar to body fluid except of some dissolved proteins and amino acids. Also, the higher difference of conductivity per 1°C can be expected.

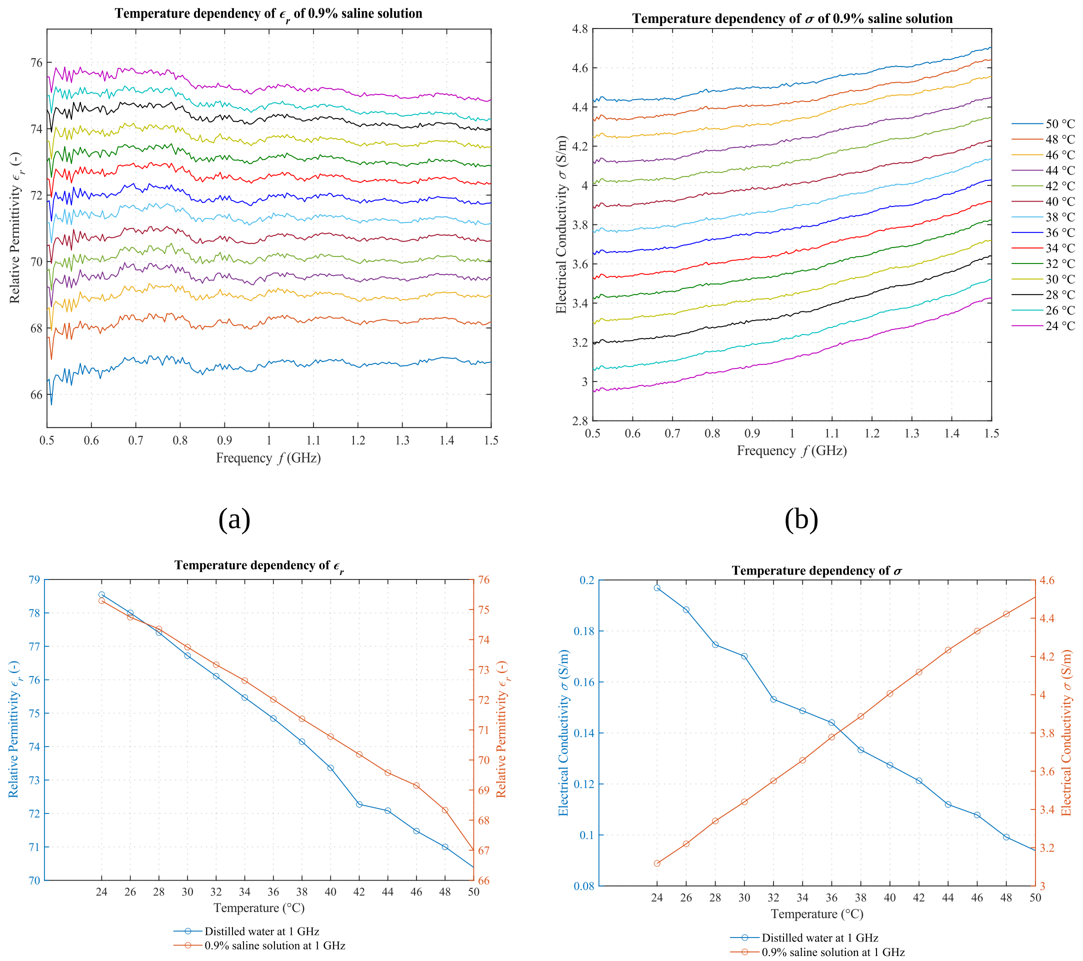

(a) (b)

(c) (d)

Figure 6.6 Measured temperature dependency of relative permittivity as well as conductivity of saline solution (a), (b) and its comparison with distilled water at frequency of 1 GHz (c) and (d).

The difference step of relative permittivity at 1 GHz behaved the same way for saline solution as well as for distilled water, approx. 0,3 per 1°C. The conductivity step per 1°C increase to circa 0,06 S/m. Next, we measured temperature dependent dielectric properties of liquid muscle phantom. It was prepared as mixture of water, sugar and salt. Different recipes for muscle phantom preparation have been already presented for instance by Fiser et.al [85]. The mixture of water, salt, agar, TX-151 and PE powder proved very similar temperature dependent dielectric properties to data obtained from measurements of porcine muscle presented by Ley et.al. [77]. However, the preparation of this phantom is time consumable and expensive compared to phantom consisted of water, sugar and salt.

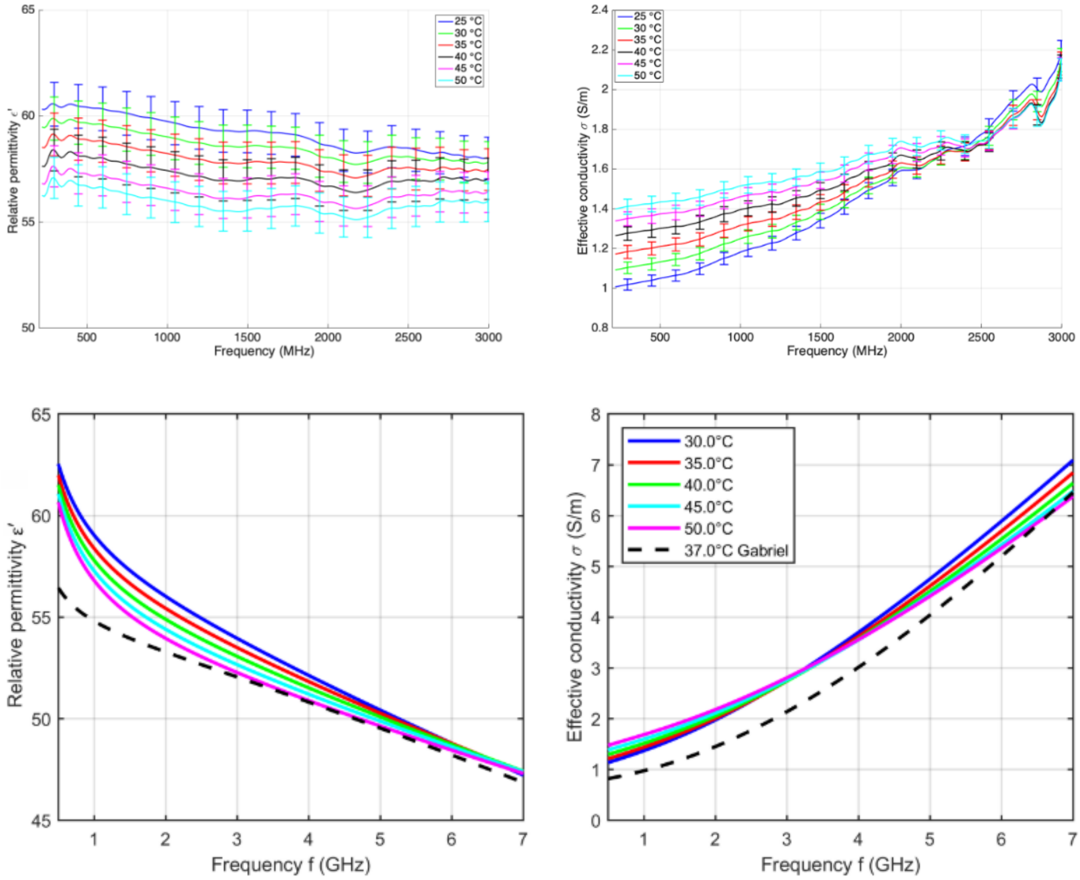

Figure 6.7 Temperature dependent relative permittivity and conductivity of muscle phantom presented by Fiser et.al. up and dielectric spectroscopy of porcine muscle presented by Ley et.al. at bottom.

Measured data of suggested liquid muscle phantom do not deviate from Fiser and Ley and are comparable with Cole-Cole model of muscle especially at frequency of interest 1 GHz as presented in Figure 6.8.

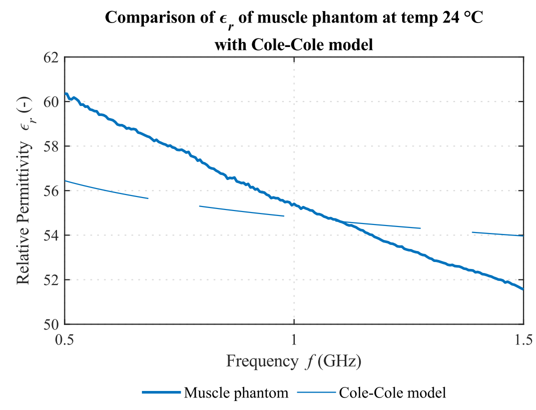

(a)

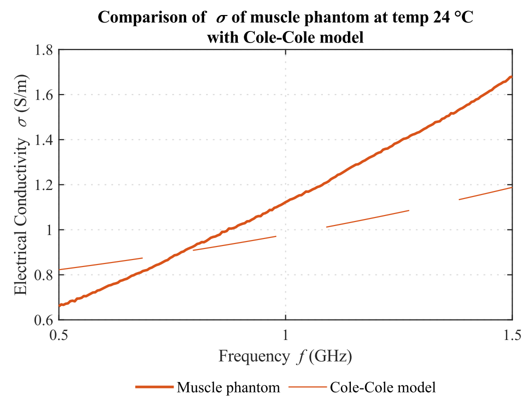

(b)

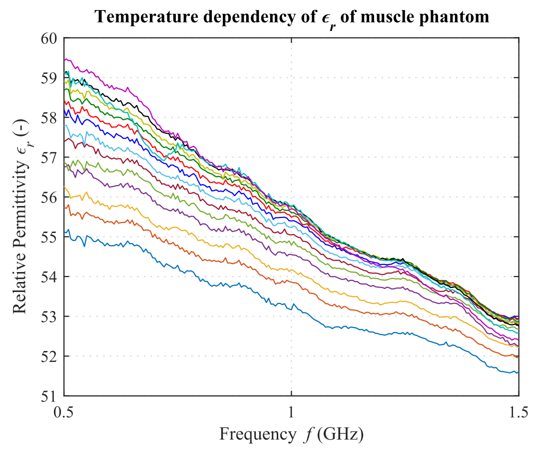

(c)

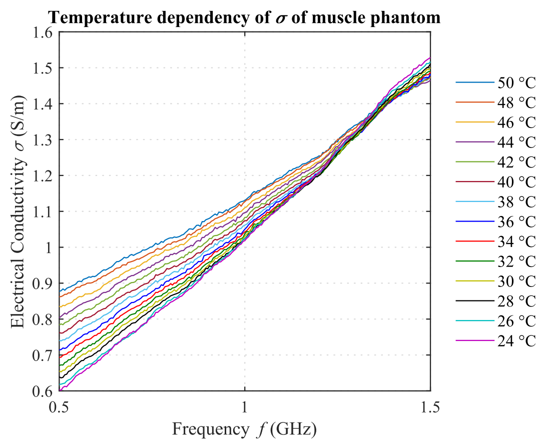

(d)

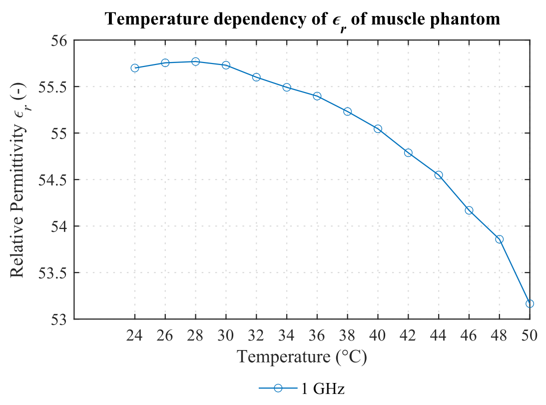

(e)

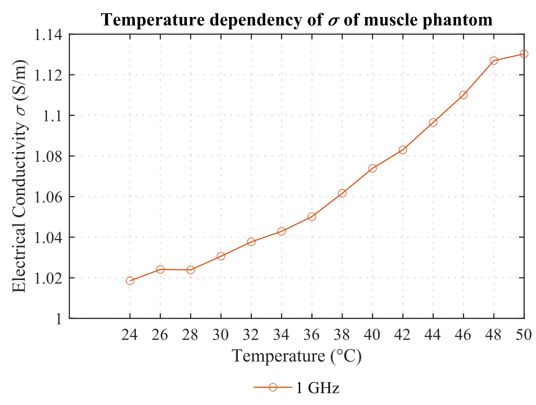

(f)

Figure 6.8 Dielectric properties of prepared liquid muscle phantom (a), (b), temperature dependency (c), (d) and trend of dielectric properties change depending on temperature at frequency of 1 GHz (e) and (f).

6.4 Experimental 16-port monopole MWI system

The MWI system designed by Meaney and Rydholm for testing of breast cancer detection [86] and available in Bioelectromagnetics group laboratories at Chalmers University was used for experimental microwave thermometry. The system consists of 16 monopole antennas (50 Ω) equidistantly positioned in circle of diameter 150 mm inside the cylindrical plastic tank filled with liquid coupling medium. The model of the system as well as monopole antenna and its dimensions are shown in Figure 6.9. The antennas operate in frequency band from 800 to 1400 MHz. And were previously designed for lossy and low permittivity matching mediums such as mixture of glyrecine and water. The computed reflection coefficient is shown in Figure 6.10.

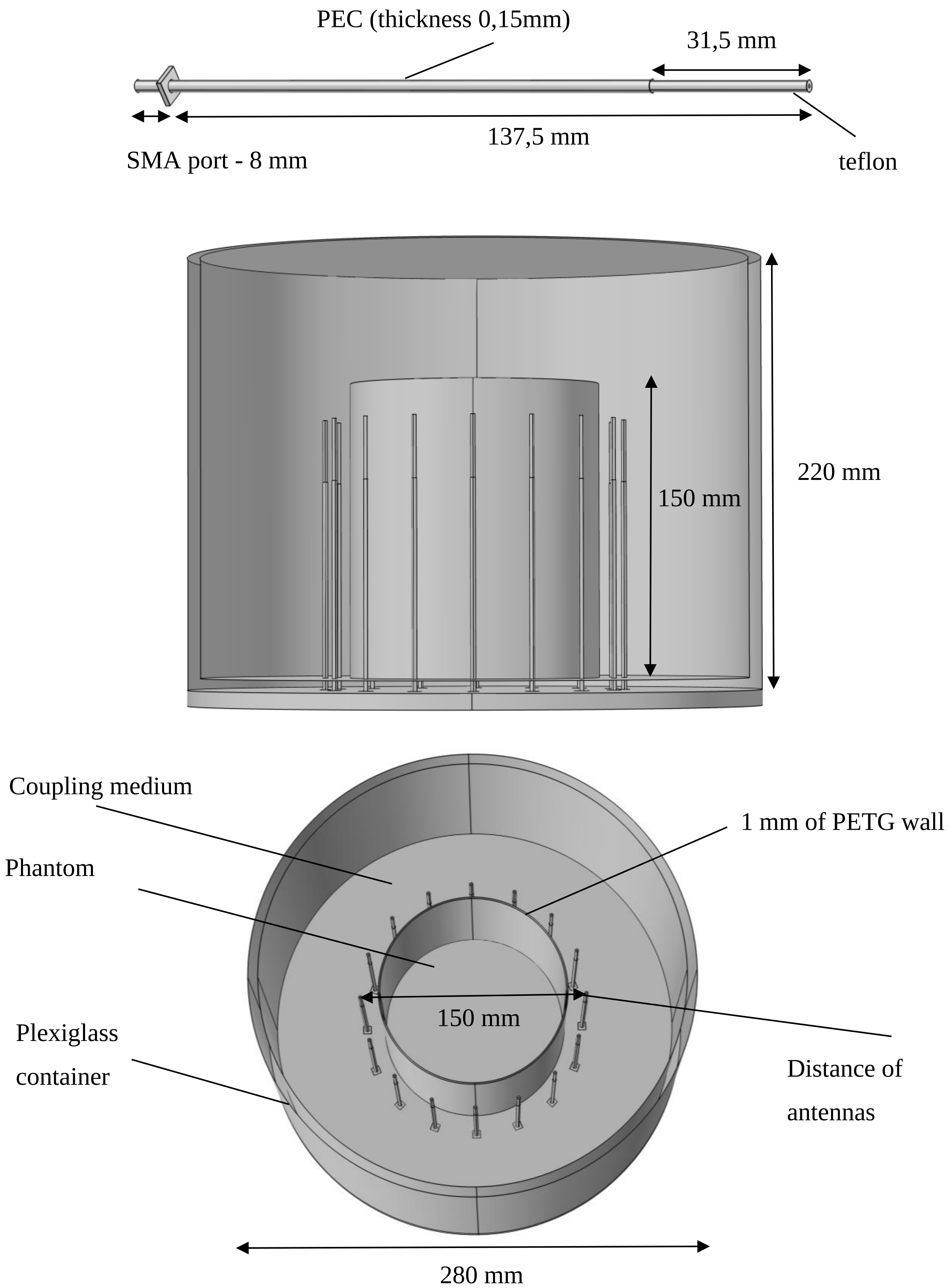

Figure 6.9 Model of monopole antenna and MWI system with its dimensions.

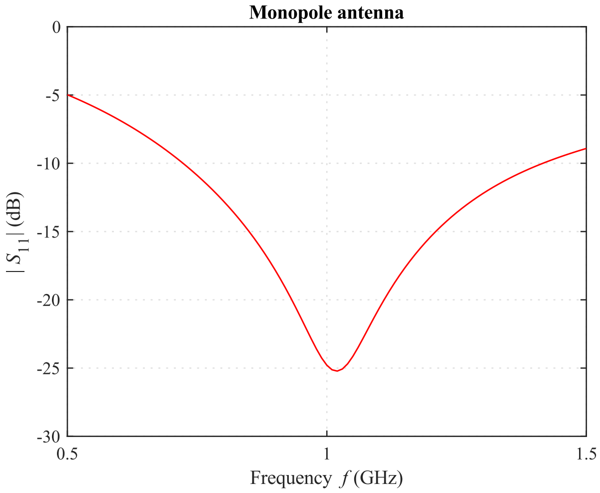

Figure 6.10 Numerically computed reflection coefficient of monopole antenna

Inside the MWI system the lossy coupling liquid prepared of glyrecine and water 80:20 weight percentages was filled. The lossy coupling medium is essential for elimination of monopole antenna mutual cross talks as studied in [48]. The dielectric properties of coupling medium are displayed in Figure 6.11.

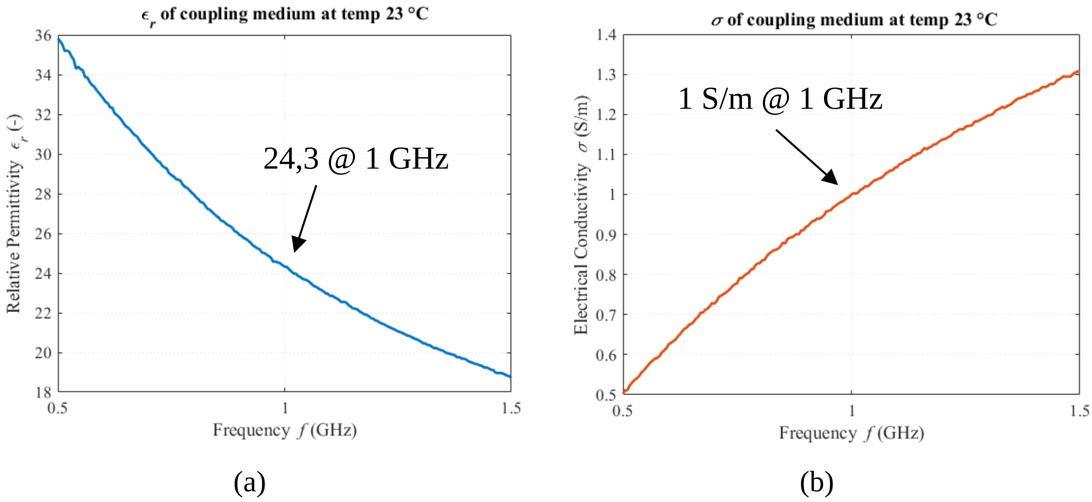

Figure 6.11 Dielectric properties, relative permittivity (a) and electrical conductivity (b) of coupling medium prepared as mixture of glycerine and water 80:20 weight percentages.

In the first iteration the cylindrical phantom and inclusion were placed inside the system to test MWI capability to detect the local dielectric contrast in terms of increase/decrease of complex permittivity. Prior to experimental testing the successful numerical analysis was proceeded and is not presented here due to simplicity of problem. The phantom and inclusion with diameter of 4 cm were prepared also from glycerine and water. The phantom was filled inside the 3D printed cylinder with wall thickness of 2 mm. The difference between relative permittivity of inclusion and phantom δ measured at 1 GHz by dielectric probe was +2,2 or +12,2, respectively and conductivity -0,06 S/m or -0,4 S/m, respectively. The experimental setup for S-parameters measurement consisted of the VNA R&S®ZNBT (Rohde&Schwarz GmbH, Germany) with dynamic range up to 140 dB as illustrated in Figure 6.12.

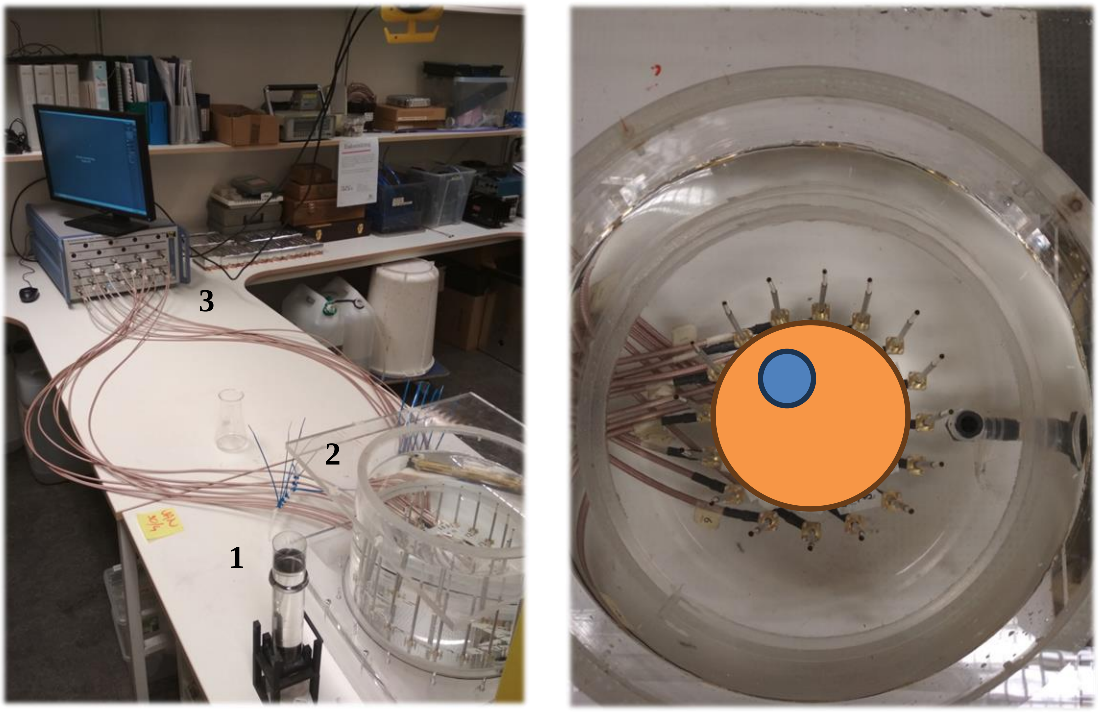

(a) (b)

Figure 6.12 Experimental setup for first iteration testing of dielectric contrast detection by monopole MWI system where in (a) is inclusion – 1, MWI system – 2 and VNA with PC – 3. In (b) schematically drawn phantom and inclusion at it position inside the plexiglass container filled with coupling medium.

The measured S-matrices together with computed electric fields by forward solver COMSOL Multiphysics were processed by many times mentioned linear reconstruction algorithm based on Born approximation and regularization by TSVD.

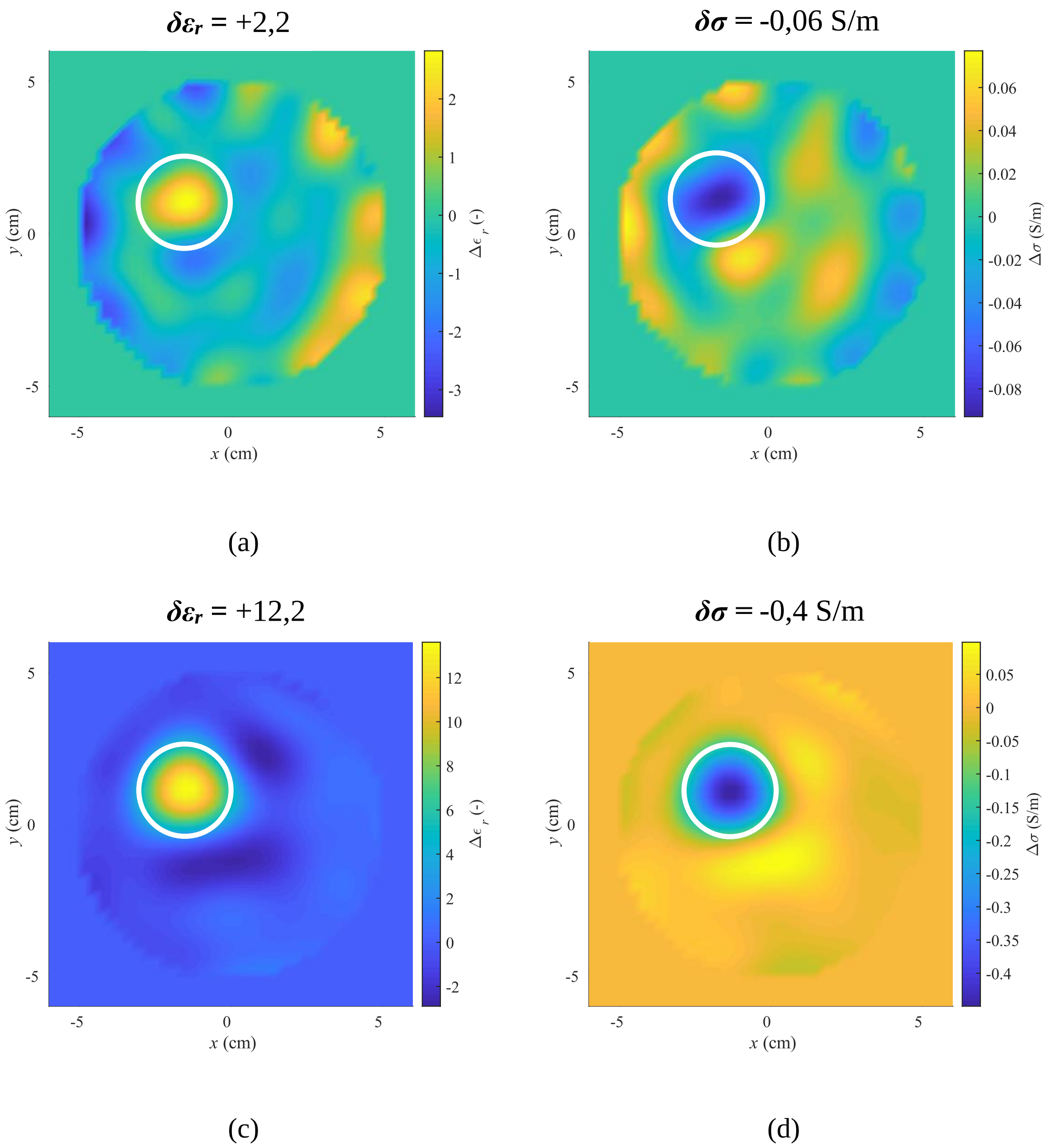

Figure 6.13 Reconstructed differential relative permittivity $\Delta\varepsilon_r$ (a), (c) and conductivity $\Delta\sigma$ (b), (d) of inclusion which actual position is marked by white circle.

As depicted above, the differential MWI imaging using monopole system showed very promising reconstruction results based on experimental measurement. Especially for higher differences of relative permittivity and conductivity the spatial as well as contrast resolution matched with differences δ measured conventionally by open-ended coaxial probe with relative error around **12 % at maximum**. Except of reconstructed conductivity for change of 0,06 S/m where the relative error reached 50 %. It was shown earlier (Subchapter 5.6.2) that very small differences of electrical conductivity bring higher inaccuracy.

In the second iteration the goal was to test capability of MWI system to follow the temperature change in terms of dielectric properties change of heated object which was placed inside the system and was naturally cooled down by surrounding coupling medium. No temperature control inside the inclusion during measurement was adapted. The inclusion was filled with coupling medium glycerine:water 80:20 heated to 50 °C and repetitive scans after 1, 2, 10, 15 and 30 minutes at frequency of 1 GHz were performed. The baseline scan was performed for empty MWI system filled only with coupling medium of given temperature of 26 °C. The behaviour of dielectric parameters of coupling medium based on temperature is plotted in Figure 6.14. While permittivity is decreasing with decreasing temperature, the conductivity increases. The reconstructed differential dielectric profiles ($\Delta\varepsilon_r$ and $\Delta\sigma$) using BA and TSVD in different time steps during cooling process of heated inclusion are summarized in Figure 6.15 or Figure 6.16, respectively.

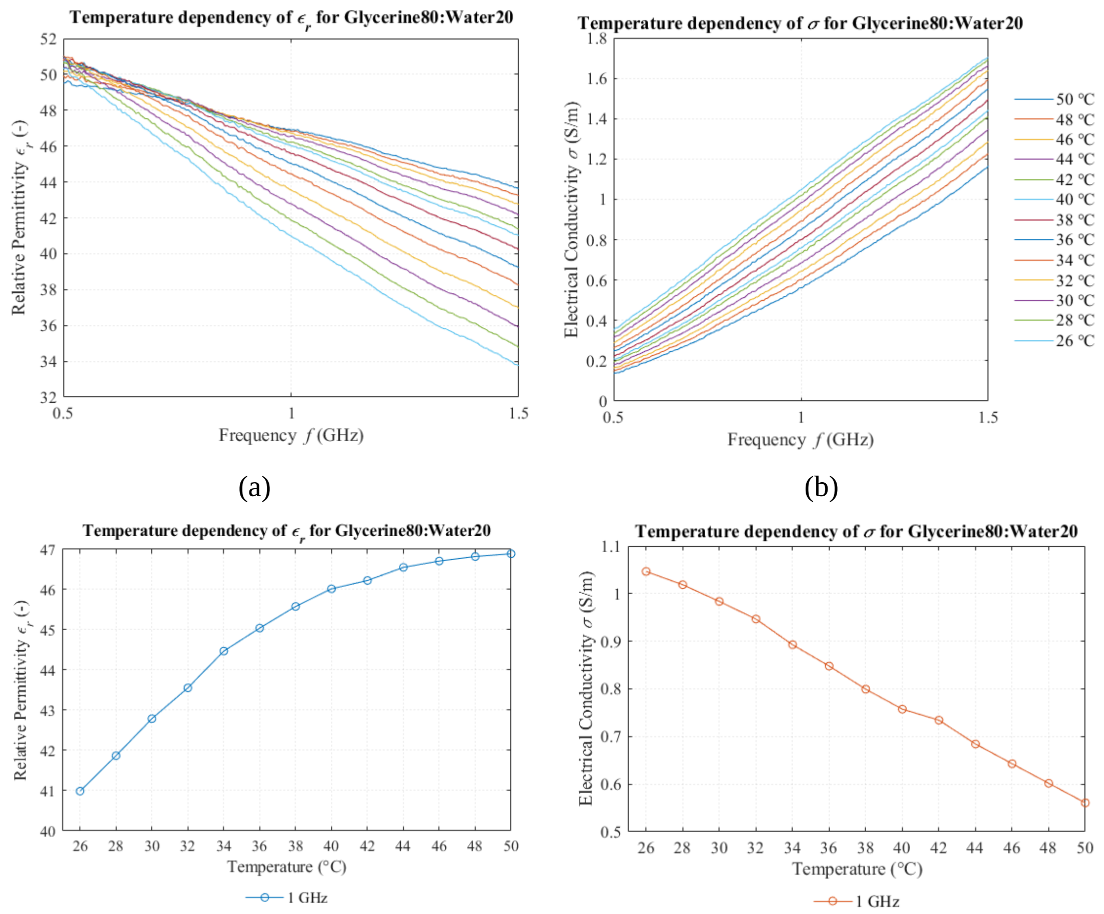

(c) (d)

Figure 6.14 Temperature dependency of relative permittivity (a) and (c), electrical conductivity (b) and (d) of coupling medium glycerine:water 80:20.

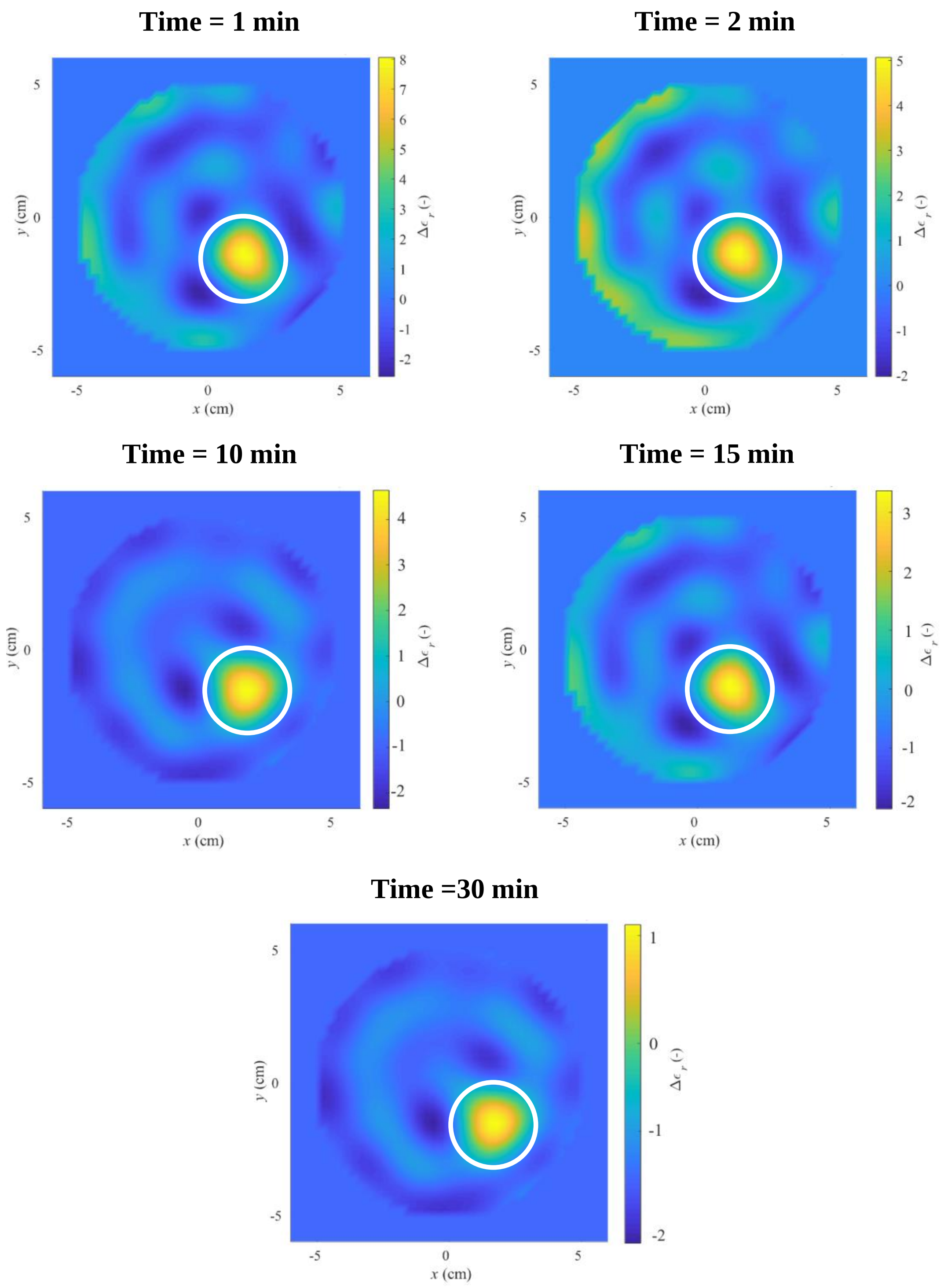

Figure 6.15 Reconstructed differential relative permittivity of inclusion heated to 50°C and placed to the MWI system where it was naturally cooled down during the time. The scans by MWI system were performed after 1, 2 10, 15 and 30 minutes from the moment of placing heated inclusion inside (white circle).

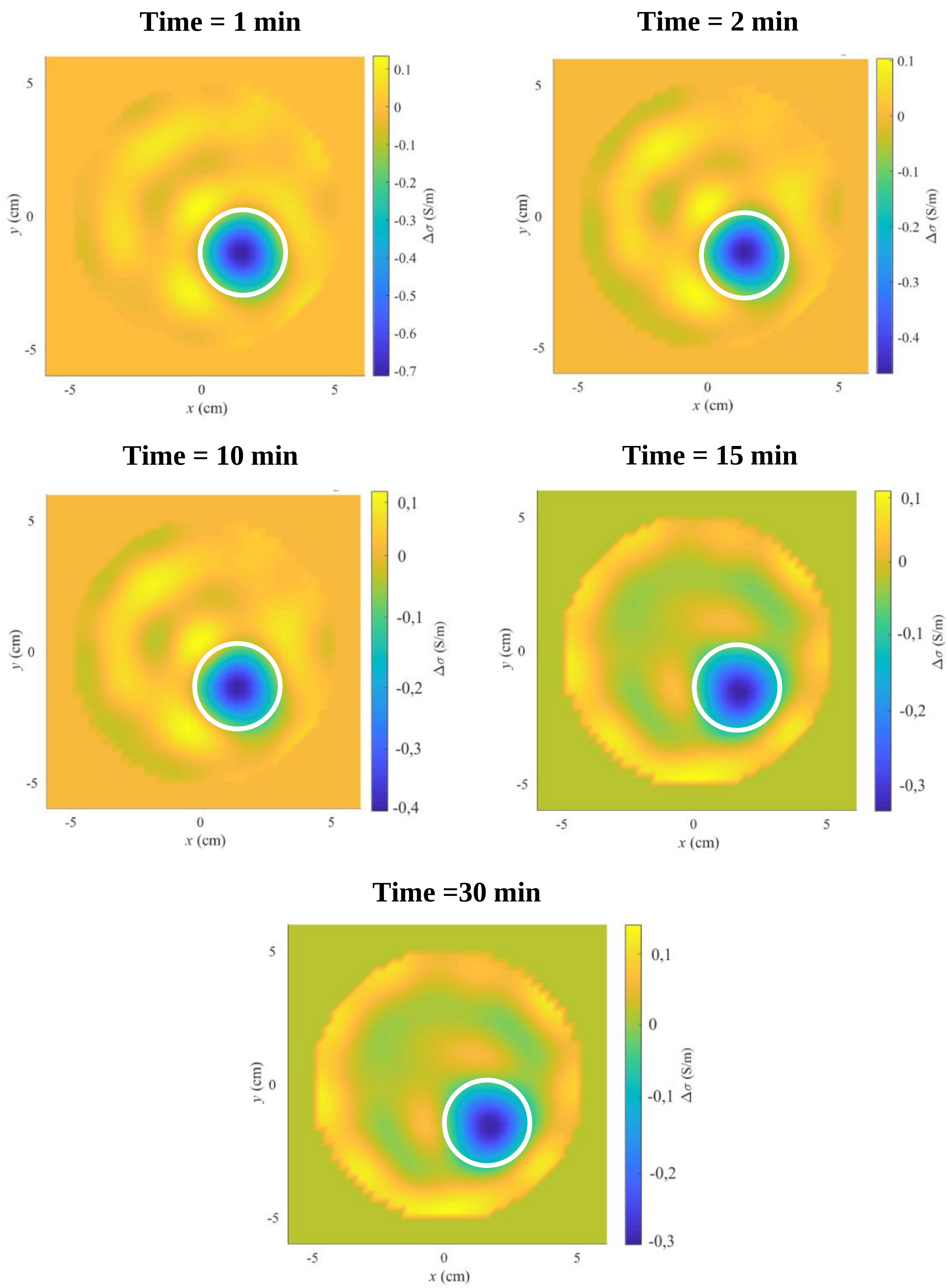

Figure 6.16 Reconstructed differential electrical conductivity of inclusion heated to 50°C and placed to the MWI system where it was naturally cooled down during the time. The scans by MWI system were performed after 1, 2 10, 15 and 30 minutes from the moment of placing heated inclusion inside (white circle).

The maximum of reconstructed differential permittivity or conductivity is always located inside the inclusion. For each time step during cooling process the reconstructed differential relative permittivity decreased, and conductivity increased which corelated with measured thermal dependency of both parameters (Figure 6.14c and d). Reconstructed discrete differences are plotted in the following Figure 6.17.

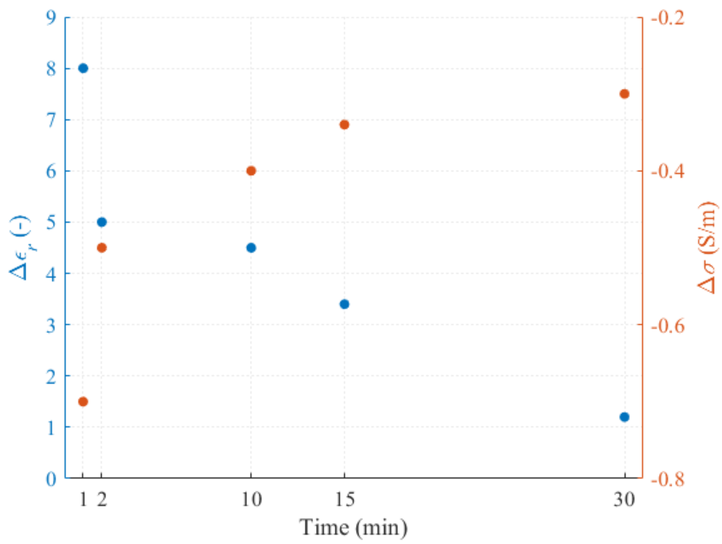

Figure 6.17 Reconstructed discrete differential values of relative permittivity and conductivity for time 1, 2, 10, 15 and 30 minutes after placing heated inclusion (50 °C) into the MWI system.

The monopole MWI system proved a concept and ability to follow up the local dielectric contrast change related to temperature change during cooling process. In clinical practice e.g. hyperthermia treatment more realistic scenario is to heat object of interest and then monitor its temperature. Therefore, **in the third iteration** we designed experimental setup allowing to heat the inclusion inside the MWI system, control its temperature by fibre optic probes and performing scans after required temperature was reached. We prepared liquid muscle phantom by mixing water, sugar and salt as presented in Figure 6.8. The phantom was enclosed in 3D printed cylinder. Inside the phantom we placed cylindrical inclusion filled with 0.9% saline solution which was circulating through heater. The scheme of setup is depicted in Figure 6.18.

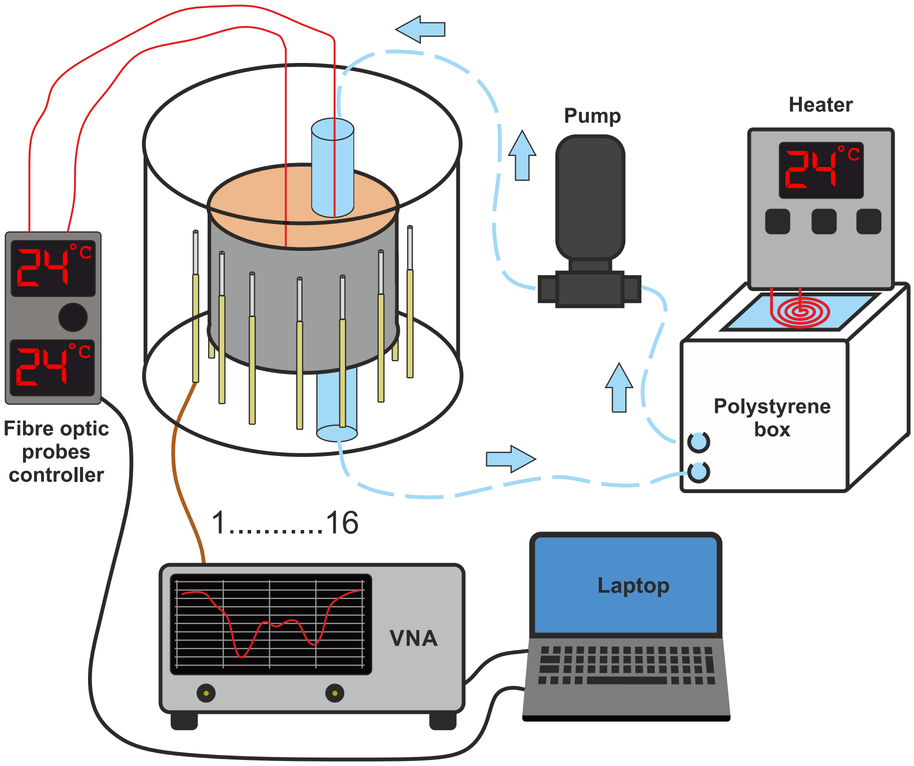

Figure 6.18 Schematic experimental setup for testing of microwave thermometry using 16-port monopole MWI system, muscle phantom (orange) and 0.9% saline solution (blue).

The measurement procedure was as follow. The requiring temperature of 0.9% saline solution was manually set on heater (from 30 to 50 °C with step of 2 °C). The step 2°C was the lowest reasonable value which was possible to stabilize for time period of measurement. The pump provided the circulation of heated solution through inclusion of diameter of 4 cm placed inside the muscle phantom. Using the fibre optic probes (FISO Technologies, Canada), we controlled the temperature inside the inclusion as well as inside the muscle phantom in close proximity of inclusion. After the temperature inside the inclusion reached the set value on controller the in-house script written in MATLAB® run the measurement of S-parameters using true multiport VNA R&S®ZNBT (Rohde&Schwarz GmbH, Germany). Output power of VNA was set to maximal 13 dBm and intermediate frequency (IF) bandwidth filter to 1 kHz as a trade-off between accuracy and scanning time. The "background" temperature of saline solution saline inside the inclusion was considered of 28 °C.

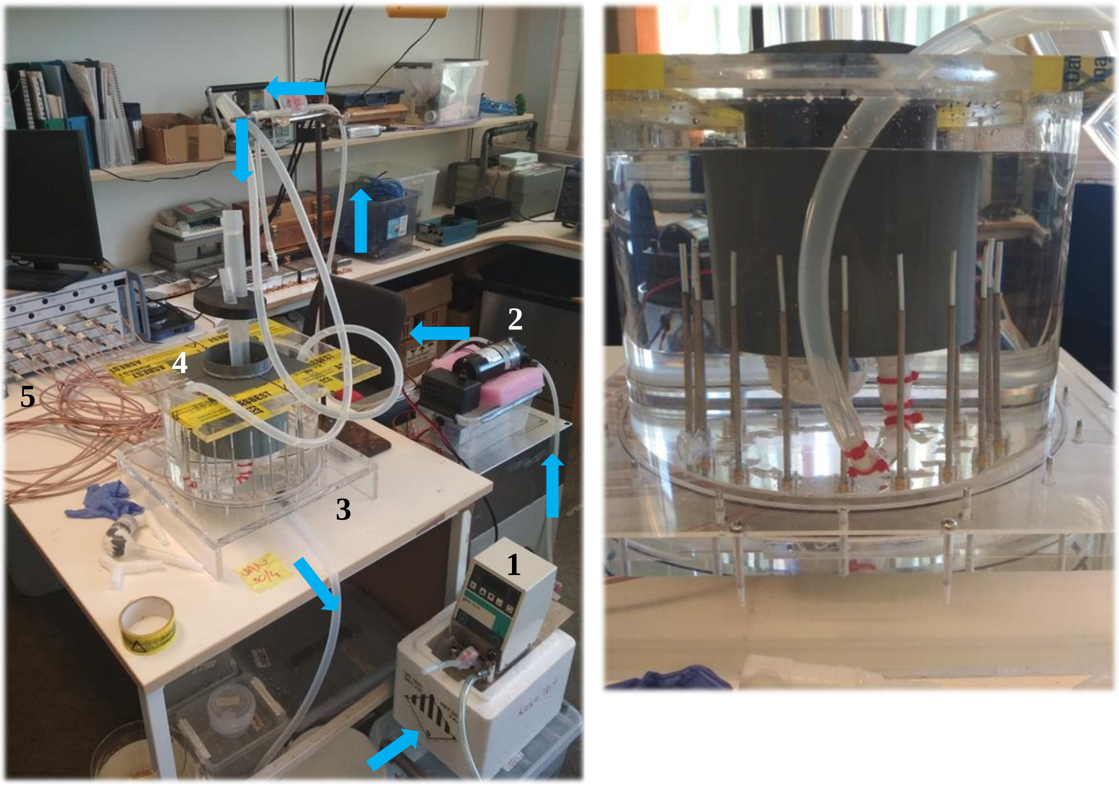

(a) (b)

Figure 6.19 Realistic photo of microwave thermometry experimental setup (a) where 1 – heater, 2 – pump, 3 – MWI system, 4 – muscle phantom with cylindrical inclusion, 5 – VNA. In (b) detail on monopole antennas and muscle phantom with inclusion inside enclosed in plexiglass container filled with coupling medium.

In first step the S-matrix for “background” (inclusion filled with saline solution of temperature 28 °C) was acquired. In next steps, S-matrices for different temperature scenarios were acquired sequentially. After each scan of each scenario the reconstruction of differential dielectric profile using DBA and regularization scheme by TSVD followed. The measurement took approx. 20 seconds and following reconstruction routine approx. 10 seconds and depended mainly on setting of IF bandwidth. In total 30 seconds which define the time resolution of differential MWI approach using linear reconstruction algorithm DBA and TSVD. The results of reconstructed differential relative permittivity as well las conductivity for different temperatures of heated saline solution inside muscle phantom are shown below in Figure 6.20.

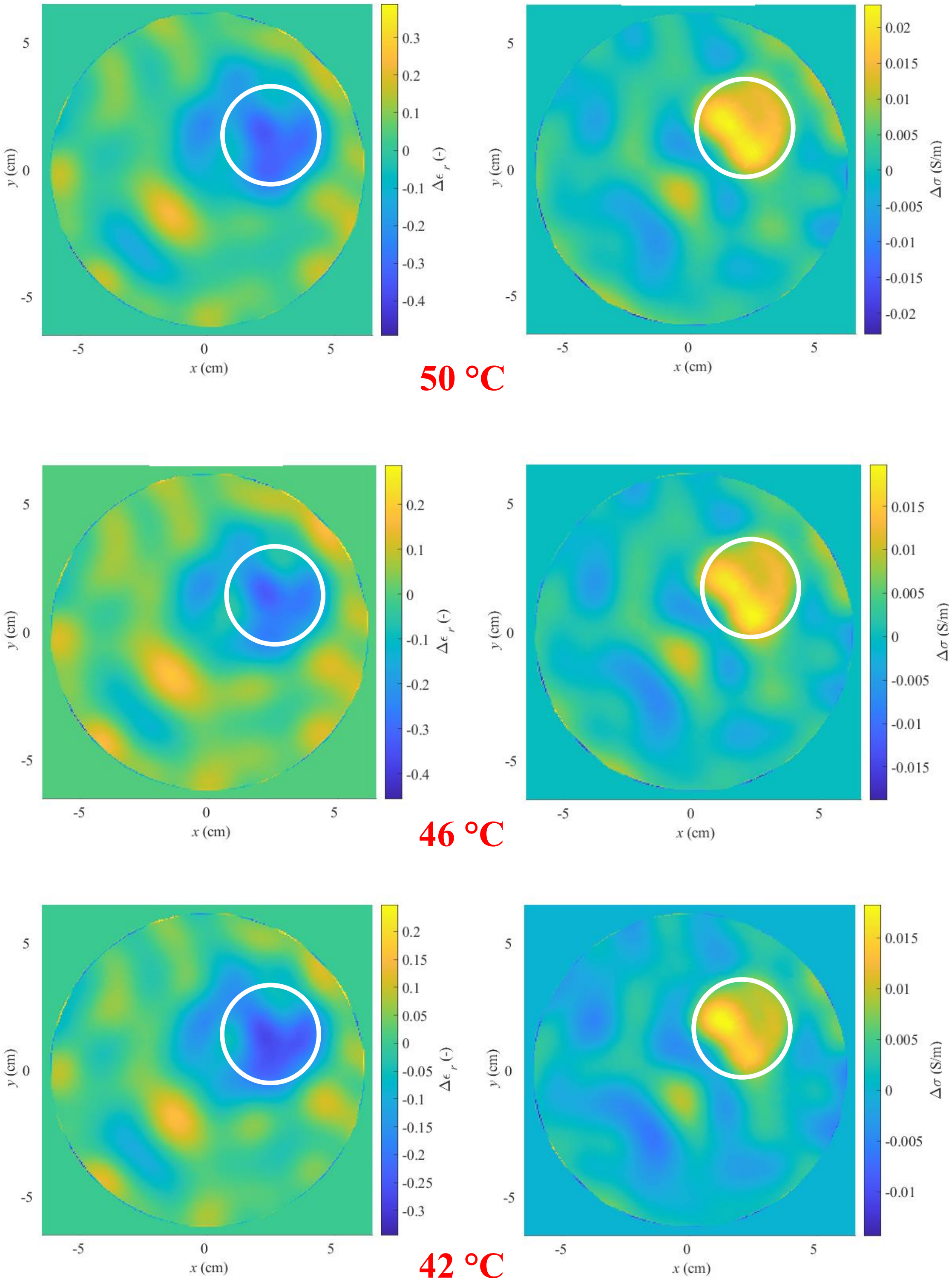

Figure 6.20 Continued.

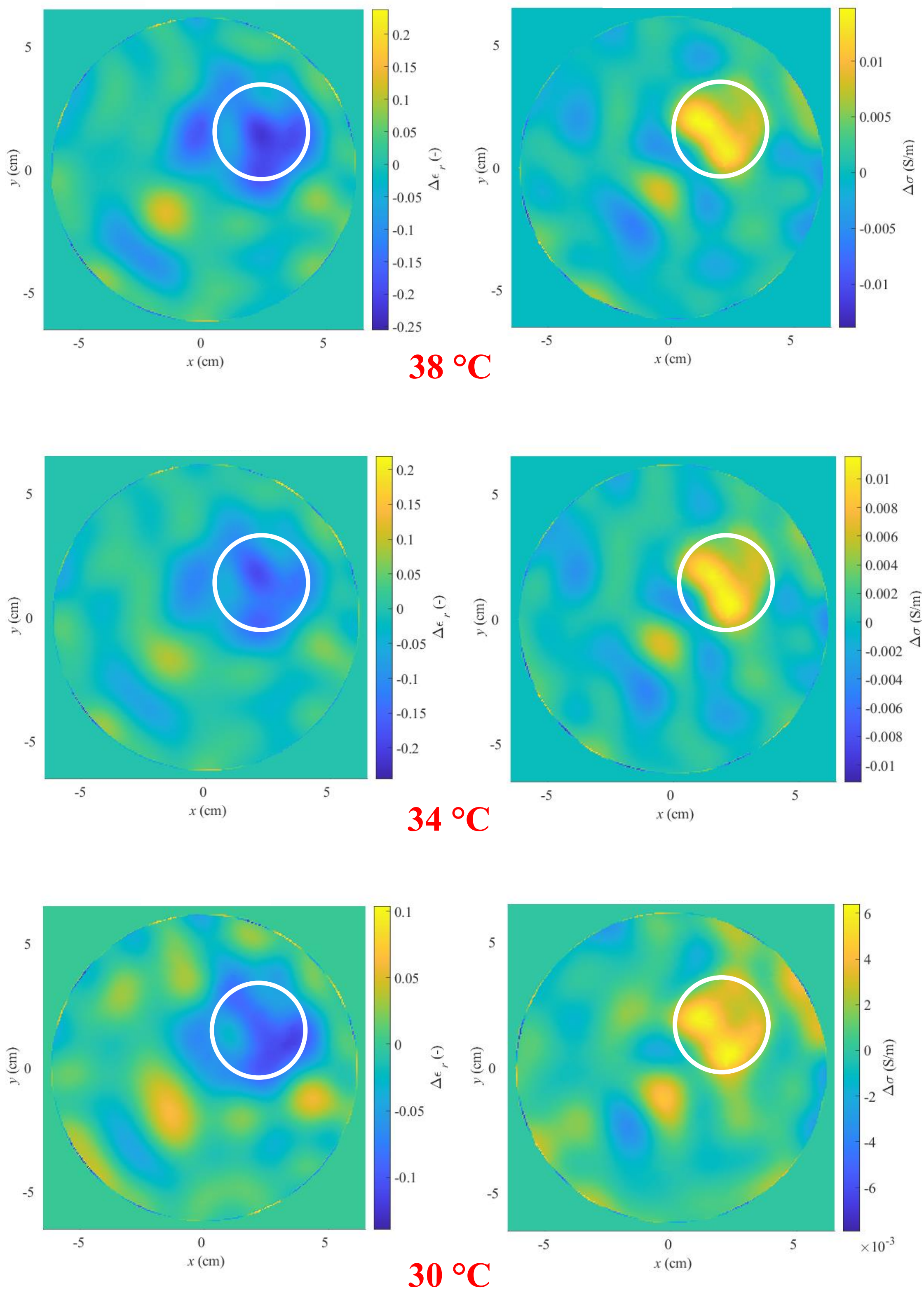

Figure 6.20 Reconstructed differential relative permittivity $\Delta\varepsilon_r$ left and conductivity $\Delta\sigma$ right for temperature scenarios from 50 to 30 °C with step of 4 °C. 2D cuts with the highest contrast were chosen. The white circle marks the actual position of the inclusion inside the phantom.

For sake of clarity the reconstructions for temperature step of 4°C are plotted. However, the maximal average reconstructed value of dielectric parameter from ROI (white circle) for temperature range from 30 to 50°C with step of 2°C was compared with measured temperature dependent dielectric parameters of saline solution by conventional probe at frequency of 1 GHz as shown in Figure 6.21. The Pearson's correlation coefficient R^2 on 95% confidential interval was calculated.

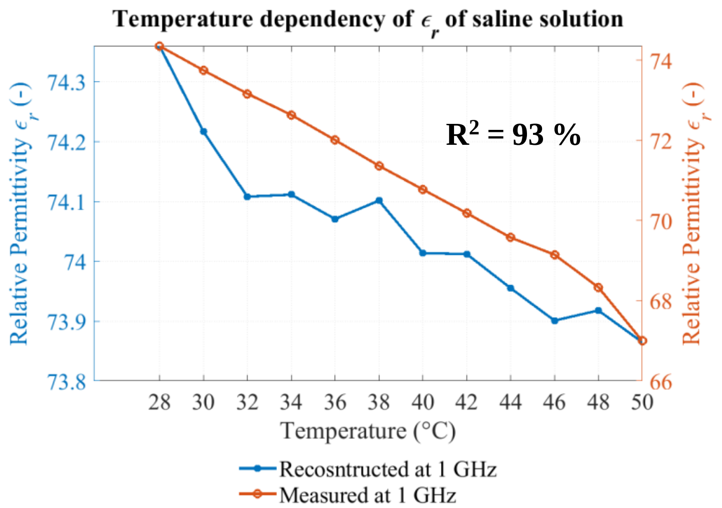

(a)

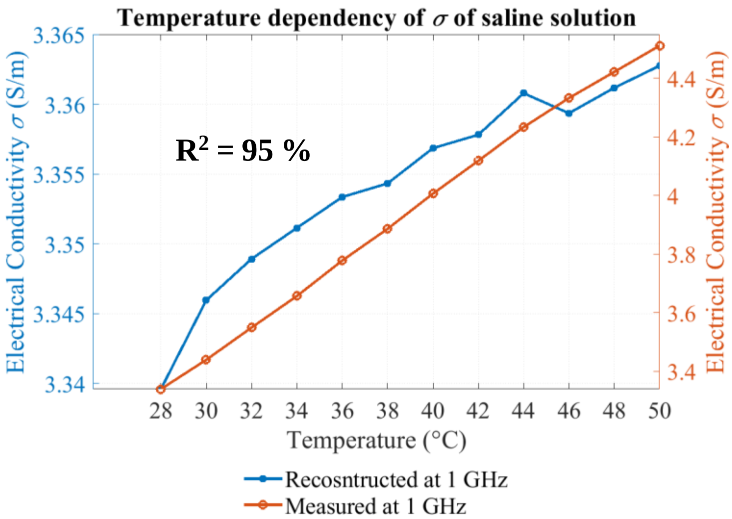

(b)

Figure 6.21 Comparison of the reconstructed and measured temperature dependency of the relative permittivity of saline solution at 1 GHz (a) and electrical conductivity (b). Pearson's correlation coefficient R^2 is plotted.

6.5 Applicator for head&neck regional hyperthermia

In laboratories of Bioelectromagnetics research group at Chalmers University of Technology the regional HT system dedicated for cancer treatment in head&neck region was developed by Takook et.al. [87] .The applicator uses as transmitters 10 self-grounded bow tie antennas immersed in plastic cavity intended to be filled by water. The antennas are held by circular plastic frame and deployed zigzag as depicted in Figure 6.22.

(a)

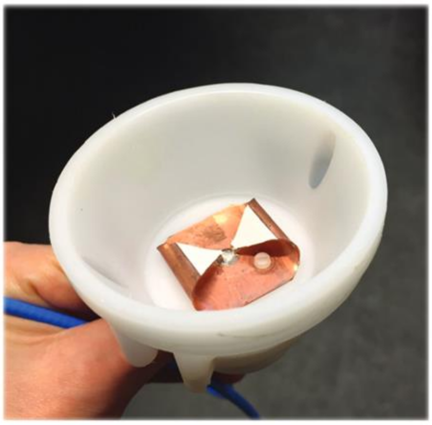

(b)

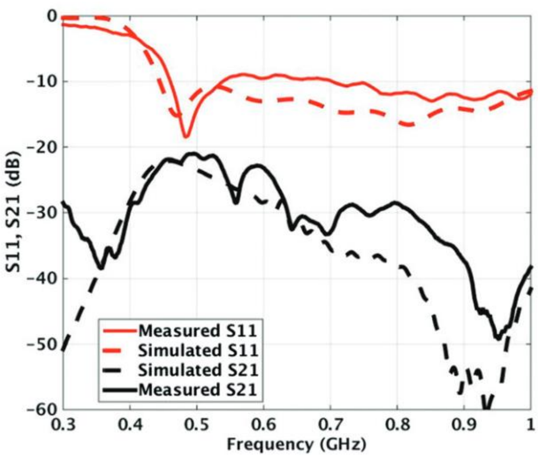

(c)

Figure 6.22 Model of HT system with zigzag positioned transmitters (a), self-grounded bow tie antenna (b) and its S-parameters (c) both adopted from [87].

The antenna operates in frequency band from 0,4 GHz to 1 GHz and thus could be also suitable to use not only for hyperthermia but also for microwave thermometry (MT) at single frequency of 1 GHz. The utilization of antenna elements for high power distribution as well as for low power S-parameters measurement could result in hybrid HT/MT system without need of any additional temperature monitor as invasive fibre optic probes, MRI or another antenna elements dedicated only for MT.

We first conducted a numerical analysis of HT system in COMSOL Multiphysics to determine its requirements and limitations for future experimental validation. The setup with muscle phantom enclosed by agar-water bolus was considered as shown in Figure 6.23.

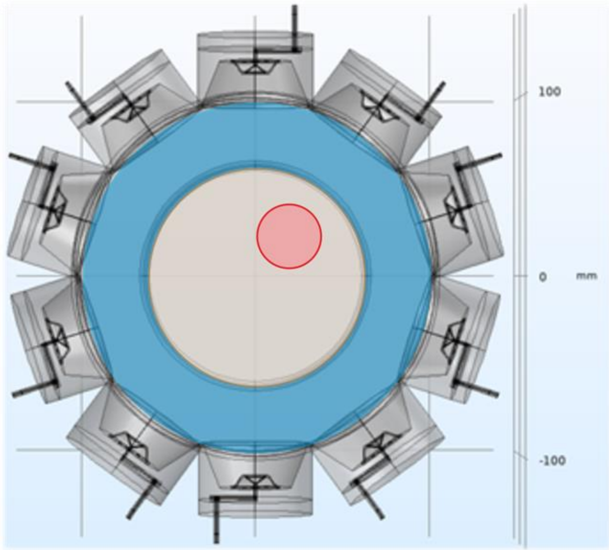

Figure 6.23 Numerical model of HT applicator from perspective view where water bolus is blue, muscle phantom orange and inclusion red marked.

Inside the muscle phantom the 4cm cylindrical inclusion with decreased relative permittivity by -3 units and increased conductivity by +0,3 S/m was placed. Using BA and TSVD we were able to reconstruct the following differential dielectric profile, Figure 6.24.

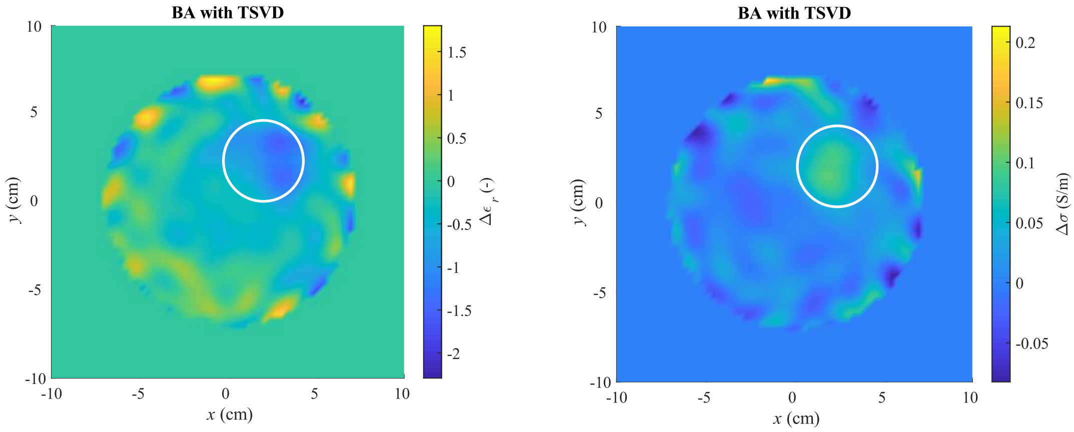

(a) (b)

Figure 6.24 Reconstructed differential dielectric profile using HT system, (a) relative permittivity, (b) conductivity of muscle phantom with cylindrical inclusion inside.

We observed high mutual cross coupling of antennas through lossless agar/water bolus which conductivity at 1 GHz reached 0,2 S/m. By gradual increasing of conductivity with step of 0,1 S/m we identified the conductivity **threshold to be 0,5 S/m**. At this value the antenna cross talks are eliminated to get sufficient reconstruction of differential dielectric profile inside the muscle phantom by HT system. Additional increasing of conductivity of bolus did not improve reconstruction results. The reconstructions based on synthetic numerical data are shown in Figure 6.25.

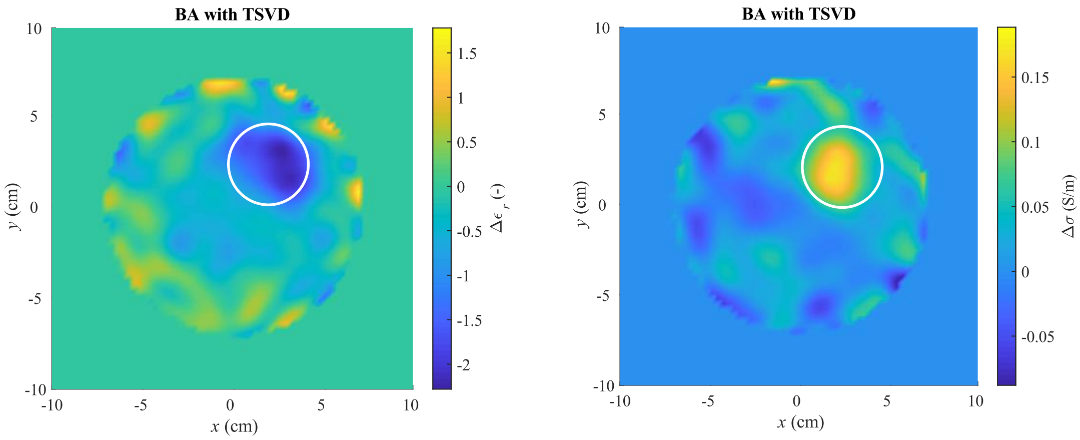

(a) (b)

Figure 6.25 Reconstructed differential dielectric properties using HT system with conductivity of agar-water bolus of 0,5 S/m.

It is obvious that lossy bolus is not suitable for hyperthermia regarding the higher input power which has to be delivered to the treated area. However, this analysis clearly showed that increasing the conductivity of bolus is essential for successful reconstruction of dielectric changes using BA/DBA. In the design process of hybrid HT/MT systems this has to be taken in account. Second option is to enclosed antennas to the cavity filled with lossy medium. This cavity will be directly attached to bolus and thus cross talks will be eliminated.

Next, the numerical analysis of capability of HT system to detect dielectric contrast based on different temperatures of pure water (27, 30 and 45 °C) positioned inside muscle phantom was performed. The dielectric contrast was representing by frequency and temperature dependent Ellison's model of pure water and its plotted in Figure 6.26. Initial temperature of inclusion was set to 25 °C. The reconstructed results were compared with model data as presented in Figure 6.27 and Figure 6.28.

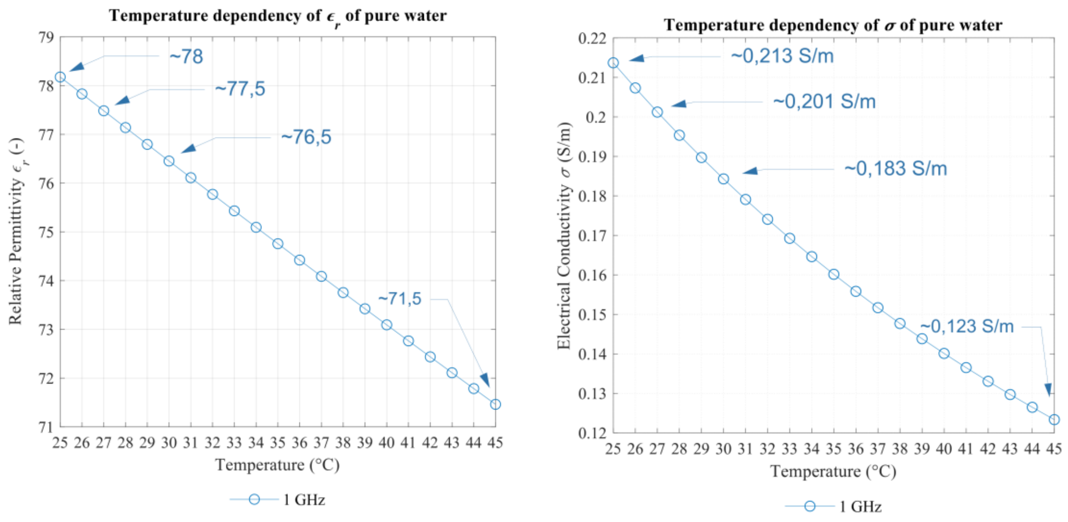

(a) (b)

Figure 6.26 Temperature dependent Ellison's model of dielectric properties of pure water for frequency of 1 GHz. (a) relative permittivity, (b) conductivity.

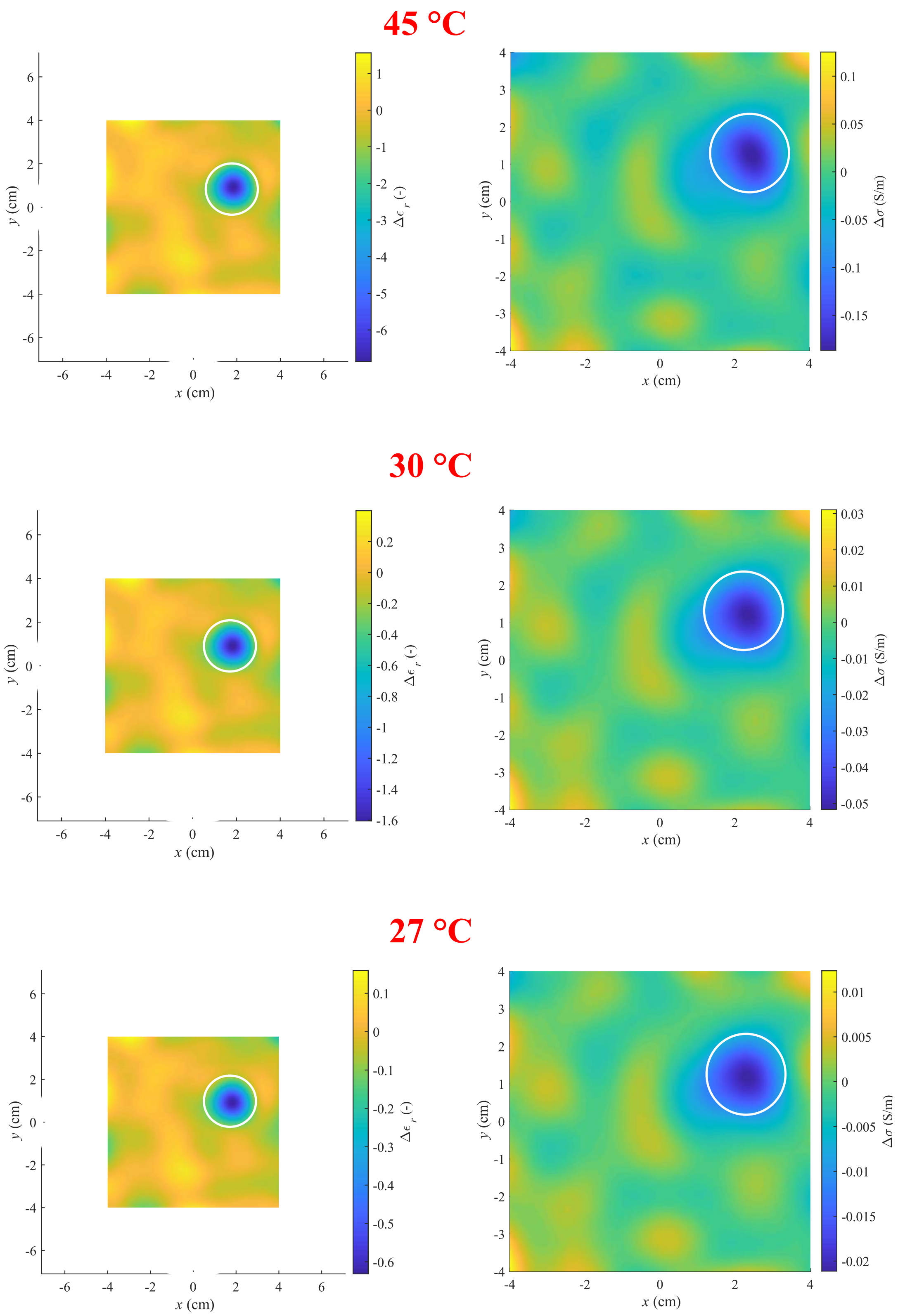

Figure 6.27 Reconstructed differential dielectric profile, relative permittivity on the left and conductivity on the right for different numerically modelled temperature of cylindrical inclusion inside the muscle phantom.

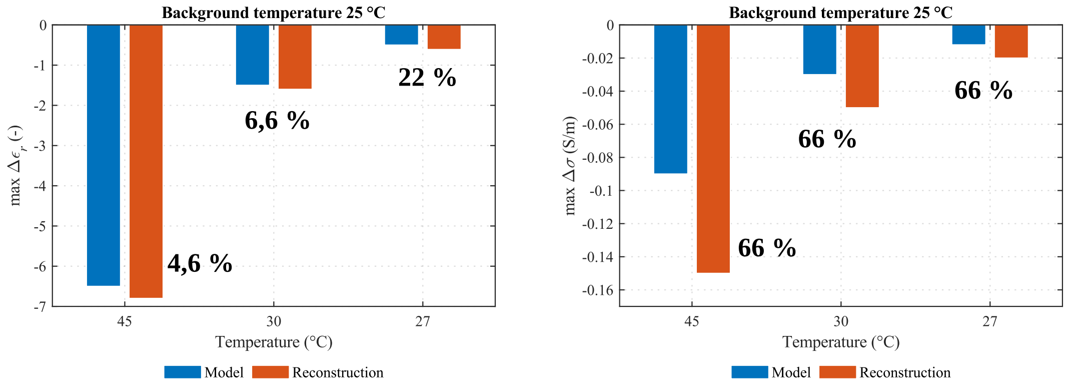

(a) (b)

Figure 6.28 Comparison of modelled changes of relative permittivity (a) and conductivity (b) for given temperatures by Ellison's model and reconstructed using DBA. Initial background temperature of inclusion was set to 25 °C. Relative error between model and reconstruction is displayed for each temperature.

For experimental measurement we prepared the agar-based water bolus with increased conductivity to 0,5 S/m at 1 GHz by adding salt. The bolus was placed around the liquid muscle phantom filled inside 3D printed cylinder and with inclusion inside. The photo of setup is in Figure 6.29.

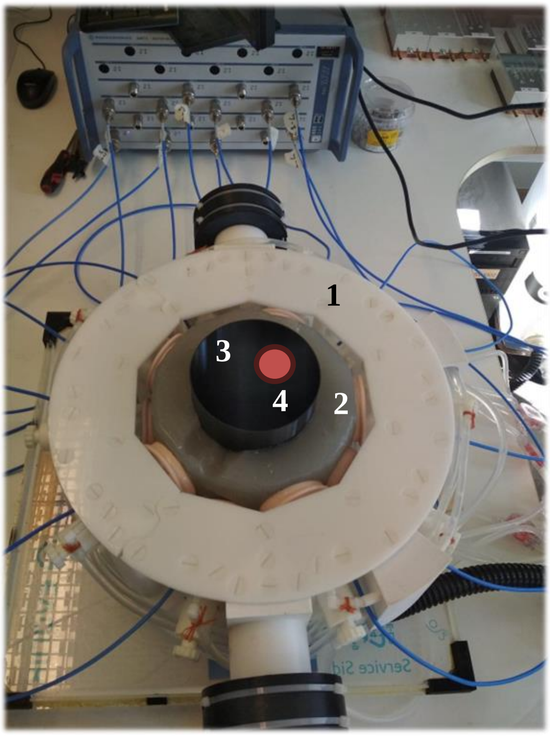

Figure 6.29 Setup for MWT using HT applicator - 1, agar-based water bolus - 2 and liquid muscle phantom – 3 and inclusion – 4.

Unfortunately, after several measurements we have not been able to reconstruct any differential dielectric profile and only noise artefacts were imaged as shown in Figure 6.30.

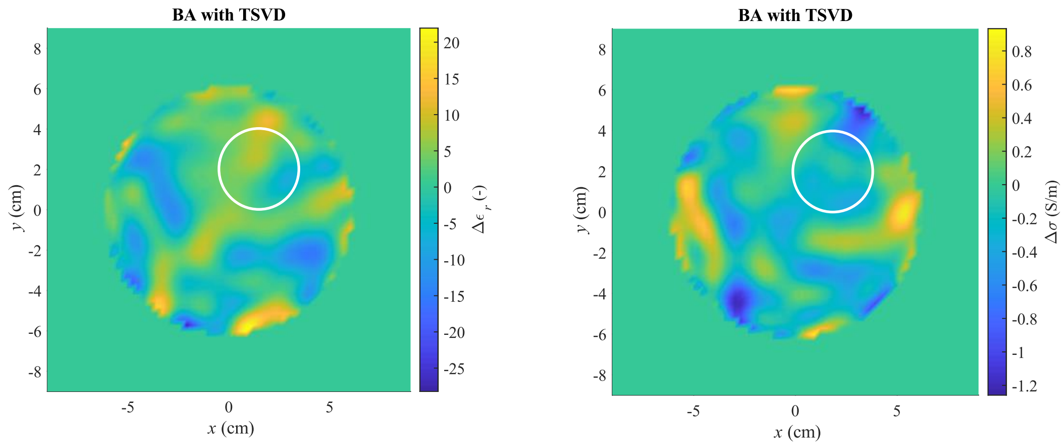

(a) (b)

Figure 6.30 Unsuccessful reconstruction of differential dielectric profile based on real data obtained by measurement with HT applicator.

6.6 Chapter conclusion

In this chapter, we introduced some preliminary results of feasibility experimental study towards non-invasive temperature monitoring using differential microwave imaging approach. In the very beginning, we examined the temperature dependency of the dielectric properties of selected materials/tissue phantoms, e.g. muscle phantom or 0.9% saline solution. These materials showed a reasonable change in both dielectric properties based on the temperature change. Thus, we employed the already developed monopole MWI system originally dedicated to breast cancer detection, and designed an experimental setup of microwave thermometry. Before that, we evaluated the capability of the MWI system to detect local changes in the dielectric properties as well as to detect changes in both dielectric parameters during a cooling process of the inserted target.

6.6.1 Microwave thermometry using a 16-port monopole MWI system

The experimental setup consisted of a liquid muscle phantom with a tube of diameter of 40 mm inside filled with 0.9% saline solution. This heterogeneous phantom was positioned inside the MWI system, which was filled with lossy coupling medium. The differential dielectric contrast of both parameters, relative permittivity and conductivity, for various temperatures of saline solution (from 28 to 50°C with step of

2°C) was obtained using differential microwave imaging approach and reconstruction algorithm based on DBA with TSVD regularization scheme.

We compared the maximal retrieved contrast with the measured values using a coaxial dielectric probe for given temperatures. Both methods were correlated to each other with a correlation coefficient of 93 or 95 % for relative permittivity or conductivity, respectively. However, the retrieved differential changes in relative permittivity and conductivity due to the change in temperature of the saline solution reached values approximately ten times lower than the measured changes and thus the exact temperature estimation, neither resolution of 2°C, was not possible. It must be noted that these experimental studies provided one of the first recent results of the feasibility of microwave thermometry employing the differential MWT (dMWT) and clinically more realistic phantoms. In addition, the change of temperature was directly related to the change in relative permittivity and conductivity. Recent study by Haynes [19] proved the concept of dMWT but was based “only” on monitoring change in absolute values of complex permittivity over time without direct temperature estimation and on clinically non-realistic homogeneous phantom or coupling medium, respectively.

The monitoring of temperature with a resolution of circa 1,5 ° C in the experimental setup with a clinically realistic scenario was reached by Meaney [80] so far. Nevertheless, the iterative reconstruction algorithm and not linear algorithm, such as DBA, was used.

The obtained results could be limited by the following effects:

- Heat flux from the heated target to the surrounding phantom. When the temperature of the saline solution reached 50 °C, the muscle phantom temperature was recorded in close proximity to the heated tube and was equal to 35 °C. This could negatively involve the measured data in terms of difference of dielectric parameters implemented in the forward model and the real setup.
- The heated saline solution was circulated through the whole system during the measurements. Thus, stationary conditions were not presented.
- The IF bandwidth filter was set to 1 kHz as a trade-off between measurement time and accuracy. Another decreasing of IF filter down to 10 Hz can improve measured data quality but for the price of increased data acquisition time.

6.6.2 Microwave thermometry using regional hyperthermia applicator

To utilize HT systems for both hyperthermia treatment as well as non-invasive microwave thermometry the great attention must be paid on waster bolus. The conductivity of the bolus at 1GHz reaches typically 0,2 S/m, and we then speak about lossless bolus. We found that this low conductivity is highly inappropriate for microwave tomography. The antennas of the HT application "communicate" through this lossless bolus and the useful signal going through the investigating domain is suppressed. Thus, no reconstructed dielectric profile has been retrieved. In the numerical study, we identified the **minimal threshold of conductivity for the water bolus to be 0,5 S/m.** For this value, we were able to retrieve dielectric contrast of the target placed inside the system. Another increase in conductivity did not lead to an improvement in the retrieved contrast. For this conductivity value the HT applicator proved sensitivity to local temperature changes simulated in FEM-based software with relative error between retrieve and modelled contrast around 20 % for temperature change of 2°C and differential relative permittivity data. The relive error was decreasing with increasing temperature difference to be reconstructed. The reconstruction process had to be done in a limited region around the target to obtain the mentioned results. We concluded that the reason for that was still the water bolus and antennas cross-talks through it. Therefore, we suggested to use lossy separators between antennas to avoid the antenna cross-talks and to improve reconstructed dielectric profiles. Increasing the water bolus conductivity is the issue for real clinical hyperthermia treatment because higher power should then be delivered to the treated region and higher bolus warming is expected, which is not desirable.

We applied the findings in experimental measurement. The lossy water bolus was used instead of separators, which has not been available yet. Unfortunately, the reconstruction of the dielectric profile based on experimental data was not successful. We identified that the problem could be the high complexity of the HT applicator, the antenna cavities are not in perfect contact with the water bolus, and thus the large reflections are recorded as well as very low values of transmission coefficients. The differences until 14 dB in measured differential S-matrix were acquired. Therefore, by using the HT applicator to combine both approaches, hyperthermia and thermometry, attention must be paid to the design of the antenna elements and the elimination of its cross-talks.

7 THESIS CONCLUSION

This thesis was focused mainly on utilization of Microwave Imaging (MWI)/Tomography (MWT) for medical diagnostic and monitoring applications. The applications were namely rapid brain stroke detection and non-invasive temperature monitoring for hyperthermia treatment. I concentrated mainly on the following topics (Chapter 5 and 6) which I consider to be my own "dissertable" contributions in the field of microwave-based medical diagnostics and monitoring.

(i) Numerical analysis of different antenna elements suitable for the mentioned applications

(ii) Design and experimental verification of a new antenna element

(iii) Development of a new 3D multichannel MWI system and its methodical experimental validation

(iv) Study of a a new concept of hybrid MWI approach

(v) Feasibility numerical as well as experimental study towards microwave thermometry using a MWI system

(vi) Feasibility numerical as well as experimental study towards microwave thermometry using the HT system

These topics were supplemented with Chapter 3 where the linear reconstruction algorithm for deferential MWI based on BA/DBA and the TSVD regularization scheme was described. In Chapter 4 the initial numerical studies focused on EM wave propagation through human head phantoms were conducted. Some important results such as minimal levels of expected transmission coefficients or spatial resolution of the MWI technique were identified.

In following paragraphs, I would like to summarize the main results related to topics (i – vi).

Chapter 5: "Design of antenna elements and MWI systems"

In the first part, the numerical analysis of different antenna elements focused on its sensitivity to dielectric contrast and to its backward radiation, was conducted. Since the antennas operate in near field region and in lossy media I designed and implemented a new methodology for evaluating near-field radiation characteristics. Based on result of analysis I developed a new compact H-slot antenna which thanks to used ground plane supressed the backward radiation and shows symmetrical feeding and mainly forward radiation.

In the second part I developed new 3D multichannel MWI system suitable for methodical testing of brain stroke detection which employed the H-slot antennas. The system and used linear reconstruction algorithm proved experimentally very good qualitative as well as quantitative parameters to detect spherical stroke targets in all three anatomical planes led through head phantom. Compared to previously obtained data by 2D MWI systems, the 3D reconstructed images reached high values of PSNR which proved very high performance of used H-slot antennas especially in suppression of backward radiation and immunity against surrounding noise. In addition, 3D antenna layout showed significant improvements of both qualitative as well as quantitative parameters in terms of stroke phantom detection compared to 2D configuration.

In the third part we demonstrated high potential of so-called hybrid MWI approach. This approach combines the radar-based imaging and tomography imaging where results of retrieved differential contrast could be significantly improved as well as the reconstruction routine can be accelerated.

Future perspectives of Chapter 5

On the basis of obtained results, I identified the following potential future steps which should be addressed in the field of microwave-based brain stroke detection.

- Data from anatomically and dielectrically realistic phantom have to confirm presented results. Attention must be paid to the dynamic range of the used hardware due to the expected higher signal attenuation around -110 dB. Also, on high fidelity between the forward model and the real scenario.

- Analysis of optimal antenna positions and orientation inside the MWI system could further improve the results.
- To perform image reconstruction using multifrequency data instead of single frequency seems to be a very promising way. However very challenging part will be design of wideband antenna with preserved suppression of backward radiation.
- Introduced hybrid approach could accelerate iterative reconstruction methods from hours to minutes and thus provide more reliable results.

Chapter 6: “Non-invasive real time microwave thermometry for hyperthermia”

In this chapter, I conducted several numerical and experimental studies focused on the feasibility of differential microwave tomography for monitoring of the temperature distribution inside the phantoms of human tissues. The first sub-chapter dealt with analysis of the temperature dependence of both dielectric parameters, relative permittivity and conductivity, for various materials such as distilled water, saline solution of muscle phantom. Next, I employed the already developed 16-port MWI system for validation of microwave thermometry concept. The initial numerical studies as well as laboratory measurements with this system showed very promising results in terms of detection of local low dielectric contrast and tracking of change in dielectric properties during the cooling process of the inserted target.

Therefore, I designed experimental setup consisting of the monopole MWI system, muscle phantom and circulating saline solution through 40mm tube positioned inside the muscle phantom. The saline solution was gradually heated from 28 to 50 °C and for each temperature step the scan of phantom was acquired. The goal of determining the resolution of the temperature of 2 ° C based on the local change in dielectric properties was not met. Nevertheless, the trend of retrieved relative permittivity and conductivity corelated with conventionally measured values in 93 or 95 %, respectively. Tracking of the trend of temperature changes based on the changes in both dielectric properties is thus feasible.

In addition, the results are based on experimental measurements on clinically more realistic phantoms, and the temperature change is directly related to the change of both dielectric parameters, which stands for unique results compared to recently published studies.

In the last part, I focused on feasibility of microwave thermometry using HT system dedicated primarily for high-power application of microwave hyperthermia in the head&neck region. The numerical study showed that the losses of water bolus (values of conductivity) have to be increased to eliminate antenna cross-talks and to retrieve the dielectric contrast. With an increased value of the bolus conductivity, the HT system showed sensitivity to numerically simulated temperature changes. The relative error between the simulated and retrieved differential dielectric contrast increased with decreasing temperature difference up to a difference of 2°C.

Future perspectives of Chapter 6

Based on obtained results, I identified the following potential future steps which should be addressed in the field of non-invasive thermometry using the differential microwave imaging approach.

- The more robust experimental setups must be developed where possible disturbances such as flow through monitored region and heat flux to surrounding domains will be eliminated.
- Using of H-slot antennas with suppressed backward radiation and symmetrical front radiation together with lossless coupling medium could increase the measured values of transmission coefficients and thus improve the MWI system sensitivity to temperature change.
- Considering the HT systems not only for hyperthermia but also for thermometry the big attention must be paid on water bolus or its conductivity, respectively. Increasing the conductivity of water bolus is not ideal solution for hyperthermia applications. The separators fabricated of lossy materials between antennas could eliminate their cross-talks while lossless of water bolus for hyperthermia is preserved.

In conclusion, I would like to state that in my opinion, the doctoral thesis fulfilled the main goals. The work and results were supported by research grants and were published either in journals with impact factor or in conference proceedings.

SCIENTIFIC PROJECTS PARTICIAPTION

Project No. SGS17/204/OHK4/3T/17: “Microwave system for detection and classification of cerebrovascular accidents”, Czech Technical University in Prague, 2017-2020, Principal investigator

Project No. CA17115: “European network for advancing Electromagnetic hyperthermic medical technologies”, Received support for Short-Term Scientific Mission (2020) and ICT Conference Grant (2021)

Project No. 17-00477Y: “Physical nature of interactions of EM fields generated by MTM structures with human body and study of their prospective use in medicine”, Czech Science Foundation, 2017-2019, Team member

Project No. 21-00579S: “Multiphysical Study of Superposition of Electromagnetic Waves in Human Head Model to Verify the Feasibility of Microwave Hyperthermia of Brain Tumors”, Czech Science Foundation, 2017-2019, Team member

Project No. LTC19031: “Development of metamaterial applicators for the regional hyperthermia system and evaluation of the accuracy of treatment planning algorithms”, Ministry of Education, Youth and Sports of Czech Republic, INTER-EXCELLANCE, INTER-COST, 2019-2022, Team member

Project No. SGS18/203/OHK4/3T/17: “Design and testing of microwave metamaterial sensors for non-invasive blood glucose measurement”, Czech Technical University in Prague, 2018-2021, Team member

Project No. SGS20/203/OHK4/3T/17: “Microwave systems for the monitoring of hyperthermic treatment of cancer in the pelvic region”, Czech Technical University in Prague, 2020-2023, Team member

Project No. SGS23/200/OHK4/3T/17: “Microwave Imaging Methods for Medical Applications”, Czech Technical University in Prague, 2023-2026, Team member

Project No. SGS14/217/OHK4/3T/17: “New Applications of EM field in Medical Diagnostics and Therapy”, 2014- 2017, Team member

REFERENCES

[1] T. A. H. S. C, “Computational Electrodynamics: The Finite-Difference Time-Domain Method, Third Edition.” Accessed: Jun. 23, 2024. [Online]. Available: https://www.amazon.com/Computational-Electrodynamics-Finite-Difference-Time-Domain-Method/dp/1580538320

[2] M. Arnold *et al.*, “Current and future burden of breast cancer: Global statistics for 2020 and 2040,” *The Breast*, vol. 66, pp. 15–23, 2022, doi: 10.1016/j.breast.2022.08.010.

[3] “Stroke Overview: Causes and types, signs and symptoms, diagnosis, and treatment.” [Online]. Available: https://synappsehealth.com/en/articles/i/stroke-overview-causes-and-types-signs-and-symptoms-diagnosis-and-treatment/

[4] J. L. Saver, “Time Is Brain—Quantified,” *Stroke*, vol. 37, no. 1, pp. 263–266, Jan. 2006, doi: 10.1161/01.STR.0000196957.55928.ab.

[5] E. S. Organisation, “Oral statement of the World Stroke Organisation (WSO) and the European Stroke Organisation (ESO),” no. September 2017, pp. 2017–2018, 2018.

[6] P. M. Meaney *et al.*, “Initial clinical experience with microwave breast imaging in women with normal mammography.,” *Acad Radiol*, vol. 14, no. 2, pp. 207–18, Feb. 2007, doi: 10.1016/j.acra.2006.10.016.

[7] J. Ljungqvist, S. Candefjord, M. Persson, L. Jönsson, T. Skoglund, and M. Elam, “Clinical Evaluation of a Microwave-Based Device for Detection of Traumatic Intracranial Hemorrhage,” *J Neurotrauma*, vol. 34, no. 13, pp. 2176–2182, Jul. 2017, doi: 10.1089/neu.2016.4869.

[8] M. Pastorino, *Microwave Imaging*. Hoboken, NJ, USA: John Wiley & Sons, Inc., 2010. doi: 10.1002/9780470602492.

[9] D. Byrne, M. O’Halloran, E. Jones, and M. Glavin, “A comparison of data-independent microwave beamforming algorithms for the early detection of breast cancer,” *Proceedings of the 31st Annual International Conference of the IEEE Engineering in Medicine and Biology Society: Engineering the Future of Biomedicine, EMBC 2009*, no. October 2019, pp. 2731–2734, 2009, doi: 10.1109/IEMBS.2009.5333344.

[10] S. Noghanian, A. Sabouni, T. Desell, and A. Ashtari, *Microwave Tomography*. New York, NY: Springer New York, 2014. doi: 10.1007/978-1-4939-0752-6.

[11] A. La Gioia *et al.*, “Open-Ended Coaxial Probe Technique for Dielectric Measurement of Biological Tissues: Challenges and Common Practices,” *Diagnostics*, vol. 8, no. 2, p. 40, 2018, doi: 10.3390/diagnostics8020040.

[12] F. Li, Y. Zheng, C. Hua, and J. Jian, “Gas sensing by microwave transduction: Review of progress and challenges,” *Front Mater*, vol. 6, no. May, pp. 1–12, 2019, doi: 10.3389/fmats.2019.00101.

[13] I. Merunka, “Feasibility Study of Microwave Differential Tomography for Medical Diagnostics and Therapy,” *Czech technical University in Prague, faculty of Electrical Engineering*, no. Ph.D. thesis, 2020, [Online]. Available: https://dspace.cvut.cz/handle/10467/92140

[14] A. Peyman, S. Holden, and C. Gabriel, “Mobile Telecommunications and Health Research Programme: Dielectric Properties of Tissues at Microwave Frequencies,” *Mobile Telecommunications and Health Research Programme*, 2005, [Online]. Available: http://www.mthr.org.uk/research_projects/documents/Rum3FinalReport.pdf

[15] C. Gabriel, S. Gabriel, and E. Corthout, “The dielectric properties of biological tissues: I. Literature survey,” *Phys Med Biol*, vol. 41, no. 11, p. 2231, Nov. 1996, doi: 10.1088/0031-9155/41/11/001.

[16] X. Li, “Body Matched Antennas for Microwave Medical Applications,” Dissertation thesis, Karlsruher Institut für Technologie (KIT), Karlsruhe, 2013. Accessed: Apr. 20, 2018. [Online]. Available: https://d-nb.info/1074672720/34

[17] David M. Pozar, *Microwave Engineering*, vol. 91. Hoboken, New Jersey, USA: John Wiley & Sons, Inc., 2017.

[18] C. Pichot, L. Jofre, G. Peronnet, and J. Bolomey, “Active microwave imaging of inhomogeneous bodies,” *IEEE Trans Antennas Propag*, vol. 33, no. 4, pp. 416–425, Apr. 1985, doi: 10.1109/TAP.1985.1143603.

[19] M. Haynes, J. Stang, and M. Moghaddam, “Real-time microwave imaging of differential temperature for thermal therapy monitoring,” *IEEE Trans Biomed Eng*, vol. 61, no. 6, pp. 1787–1797, 2014, doi: 10.1109/TBME.2014.2307072.

[20] R. Scapaticci, L. Di Donato, I. Catapano, and L. Crocco, “A Feasibility Study on Mirowave Imaging for Brain Stroke Monitoring,” *Progress In Electromagnetics Research*, vol. 36, no. November 2012, pp. 283–301, 2012.

[21] R. Scapaticci, O. M. Bucci, I. Catapano, and L. Crocco, “Robust microwave imaging for brain stroke monitoring,” *Antennas and Propagation (EuCAP), 2013 7th European Conference on*, no. Eucap, pp. 75–78, 2013.

[22] Nie Zaiping, Yang Feng, Zhao Yanwen, and Zhang Yerong, “Variational Born iteration method and its applications to hybrid inversion,” *IEEE Transactions on Geoscience and Remote Sensing*, vol. 38, no. 4, pp. 1709–1715, Jul. 2000, doi: 10.1109/36.851969.

[23] K. Bialkowski, D. Ireland, and A. Abbosh, “Microwave imaging for brain stroke detection using Born iterative method,” *IET Microwaves, Antennas & Propagation*, vol. 7, no. 11, pp. 909–915, 2013, doi: 10.1049/iet-map.2013.0054.

[24] R. A. Willoughby, “Solutions of Ill-Posed Problems (A. N. Tikhonov and V. Y. Arsenin),” *SIAM Review*, vol. 21, no. 2, pp. 266–267, Apr. 1979, doi: 10.1137/1021044.

[25] I. Merunka, A. Massa, D. Vrba, O. Fiser, M. Salucci, and J. Vrba, “Microwave Tomography System for Methodical Testing of Human Brain Stroke Detection Approaches,” *Int J Antennas Propag*, vol. 2019, pp. 1–9, Mar. 2019, doi: 10.1155/2019/4074862.

[26] M. Persson *et al.*, "Microwave-based stroke diagnosis making global prehospital thrombolytic treatment possible," *IEEE Trans Biomed Eng*, vol. 61, no. 11, pp. 2806–2817, Nov. 2014, doi: 10.1109/TBME.2014.2330554.

[27] C. Amuthadevi, K. Meena, and K. Arthi, "Acute stage of brain stroke diagnosis using hybrid genetic algorithm for optimization of feature selection and Classifier," *International Journal of Engineering and Technology(UAE)*, vol. 7, pp. 70–75, 2018, doi: 10.1080/10580530.2017.1330004.

[28] R. Scapaticci, O. M. Bucci, I. Catapano, and L. Crocco, "Differential Microwave Imaging for Brain Stroke Followup," *Int J Antennas Propag*, vol. 2014, pp. 1–11, Jan. 2014, doi: 10.1155/2014/312528.

[29] L. Crocco, I. Catapano, L. Di Donato, and T. Isernia, "The linear sampling method as a way to quantitative inverse scattering," *IEEE Trans Antennas Propag*, vol. 60, no. 4, pp. 1844–1853, 2012, doi: 10.1109/TAP.2012.2186250.

[30] M. Haynes and M. Moghaddam, "Vector green's function for S-parameter measurements of the electromagnetic volume integral equation," *IEEE Antennas and Propagation Society, AP-S International Symposium (Digest)*, vol. I, pp. 1100–1103, 2011, doi: 10.1109/APS.2011.5996473.

[31] D. O. Rodriguez-Duarte *et al.*, "Experimental Validation of a Microwave System for Brain Stroke 3-D Imaging," *Diagnostics*, vol. 11, no. 7, Jul. 2021, doi: 10.3390/DIAGNOSTICS11071232.

[32] M. Fernando, K. Busawon, M. Elsdon, and D. Smith, "Fundamental issues in antenna design for microwave medical imaging applications," in *2010 7th International Symposium on Communication Systems, Networks and Digital Signal Processing, CSNDSP 2010*, 2010, pp. 795–800. doi: 10.1109/csndsp16145.2010.5580323.

[33] L. M. R. Anne M. Gilroy, Brian R. MacPherson, *Atlas of Anatomy*. Thieme, 2008.

[34] Erik G. Lee, R. L. Hadimani, and D. C. Jiles, "„Population Head Model Repository V1.0". IT'IS Foundation." [Online]. Available: https://itis.swiss/virtual-population/regional-human-models/phm-repository/v1-0/

[35] I. Merunka, J. Vrba, O. Fiser, and D. Vrba, "Comparison of bowtie slot and rectangular waveguide-based antennas for microwave medical imaging," *IET Conference Publications*, vol. 2018, no. CP741, 2018, doi: 10.1049/CP.2018.0836.

[36] S. Semenov, T. Huynh, T. Williams, B. Nicholson, and A. Vasilenko, "Dielectric properties of brain tissue at 1 GHz in acute ischemic stroke: Experimental study on swine," *Bioelectromagnetics*, vol. 38, no. 2, pp. 158–163, 2017, doi: 10.1002/bem.22024.

[37] O. Fiser, I. Merunka, and J. Vrba, "Waveguide applicator system for head and neck hyperthermia treatment," *Journal of Electrical Engineering and Technology*, vol. 11, no. 6, pp. 1744–1753, 2016, doi: 10.5370/JEET.2016.11.6.1744.

[38] B. Borja, J. A. Tirado-Mendez, and H. Jardon-Aguilar, "An Overview of UWB Antennas for Microwave Imaging Systems for Cancer Detection Purposes," *Progress In Electromagnetics Research B*, vol. 80, no. March, pp. 173–198, 2018, doi: 10.2528/PIERB18030302.

[39] T. Zwick, M. Jalilvand, J. Kowalewski, and X. Li, "Broadband miniaturised bow-tie antenna for 3D microwave tomography," *Electron Lett*, vol. 50, no. 4, pp. 244–246, 2014, doi: 10.1049/el.2013.3974.

[40] M. A. Shokry and A. M. M. A. Allam, "UWB Antenna for brain stroke and brain tumour detection," *2016 21st International Conference on Microwave, Radar and Wireless Communications, MIKON 2016*, pp. 5–7, 2016, doi: 10.1109/MIKON.2016.7491967.

[41] H. Trefná and M. Persson, "Antenna array design for brain monitoring," *2008 IEEE International Symposium on Antennas and Propagation and USNC/URSI National Radio Science Meeting, APSURSI*, pp. 1–4, 2008, doi: 10.1109/APS.2008.4619683.

[42] J. S. Row and Y. Y. Liou, "Broadband short-circuited triangular patch antenna," *IEEE Trans Antennas Propag*, vol. 54, no. 7, pp. 2137–2141, 2006, doi: 10.1109/TAP.2006.875916.

[43] Y. Wu, M. Wang, and S. Ye, "A Campact Ultra-wideband Antenna far Strake," vol. 3, no. c, pp. 4–6.

[44] M. Lanini, S. Poretti, A. Salvade, and R. Monleone, "Design of a slim wideband-antenna to overcome the strong reflection of the air-to-sample interface in microwave imaging," *Proceedings of the 2015 International Conference on Electromagnetics in Advanced Applications, ICEAA 2015*, no. c, pp. 1020–1023, 2015, doi: 10.1109/ICEAA.2015.7297269.

[45] R. Yahya, M. R. Kamarudin, and N. Seman, "New wideband textile antenna for SAR investigation in head microwave imaging," *Conference Proceedings - 2014 IEEE MTT-S International Microwave Workshop Series on: RF and Wireless Technologies for Biomedical and Healthcare Applications, IMWS-Bio 2014*, pp. 1–3, 2015, doi: 10.1109/IMWS-BIO.2014.7032443.

[46] I. Saied, "Wideband Textile Antenna for Monitoring Neurodegenerative Diseases," *2018 IEEE 29th Annual International Symposium on Personal, Indoor and Mobile Radio Communications (PIMRC)*, pp. 356–360, 2018.

[47] A. T. Mobashsher, B. J. Mohammed, S. Mustafa, and A. Abbosh, "Ultra wideband antenna for portable brain stroke diagnostic system," *2013 IEEE MTT-S International Microwave Workshop Series on RF and Wireless Technologies for Biomedical and Healthcare Applications, IMWS-BIO 2013 - Proceedings*, vol. 1032, pp. 2–4, 2013, doi: 10.1109/IMWS-BIO.2013.6756163.

[48] P. M. Meaney, F. Shubitidze, M. W. Fanning, M. Kmiec, N. R. Epstein, and K. D. Paulsen, "Surface Wave Multipath Signals in Near-Field Microwave Imaging," *Int J Biomed Imaging*, vol. 2012, p. 11, 2012, doi: 10.1155/2012/697253.

[49] S. Semenov, B. Seiser, E. Stoegmann, and E. Auff, “Electromagnetic tomography for brain imaging: From virtual to human brain,” *2014 IEEE Conference on Antenna Measurements and Applications, CAMA 2014*, pp. 2–5, 2014, doi: 10.1109/CAMA.2014.7003417.

[50] S. Semenov, M. Hopfer, R. Planas, A. Hamidipour, and T. Henriksson, “Electromagnetic tomography for brain imaging: 3D reconstruction of stroke in a human head phantom,” *2016 IEEE Conference on Antenna Measurements and Applications, CAMA 2016*, pp. 1–4, 2017, doi: 10.1109/CAMA.2016.7815752.

[51] P. H. Tournier *et al.*, “Microwave tomography for brain stroke imaging,” *2017 IEEE Antennas and Propagation Society International Symposium, Proceedings*, vol. 2017-Janua, pp. 29–30, 2017, doi: 10.1109/APUSNCURSINRSM.2017.8072057.

[52] P.-H. Tournier *et al.*, “Microwave Tomographic Imaging of Cerebrovascular Accidents by Using High-Performance Computing,” Jul. 2016, Accessed: Jan. 30, 2019. [Online]. Available: http://arxiv.org/abs/1607.02573

[53] A. T. Mobashsher and A. Abbosh, “Microwave imaging system to provide portable-low-powered medical facility for the detection of intracranial hemorrhage,” *AMS 2014 - 2014 1st Australian Microwave Symposium, Conference Proceedings*, pp. 23–24, 2014, doi: 10.1109/AUSMS.2014.7017347.

[54] A. T. Mobashsher, A. M. Abbosh, and Y. Wang, “Microwave System to Detect Traumatic Brain Injuries Using Compact Unidirectional Antenna and Wideband Transceiver With Verification on Realistic Head Phantom,” *undefined*, 2014, Accessed: Jan. 30, 2019. [Online]. Available: https://www.semanticscholar.org/paper/Microwave-System-to-Detect-Traumatic-Brain-Injuries-Mobashsher-Abbosh/c26f8c6d6cdc6e9962664030249ce694086513e6

[55] A. T. Mobashsher, A. Mahmoud, and A. M. Abbosh, “Portable Wideband Microwave Imaging System for Intracranial Hemorrhage Detection Using Improved Back-projection Algorithm with Model of Effective Head Permittivity,” *Sci Rep*, vol. 6, no. February, pp. 1–16, 2016, doi: 10.1038/srep20459.

[56] A. T. Mobashsher and A. M. Abbosh, “On-site Rapid Diagnosis of Intracranial Hematoma using Portable Multi-slice Microwave Imaging System,” *Sci Rep*, vol. 6, no. November, pp. 1–17, 2016, doi: 10.1038/srep37620.

[57] A. T. Mobashsher and A. M. Abbosh, “Three-dimensional human head phantom with realistic electrical properties and anatomy,” *IEEE Antennas Wirel Propag Lett*, vol. 13, pp. 1401–1404, 2014, doi: 10.1109/LAWP.2014.2340409.

[58] A. T. Mobashsher, “Wideband Microwave Imaging System for Brain Injury Diagnosis,” *Phd Thesis, The University of Queensland*, 2016, doi: 10.14264/uql.2016.280.

[59] A. Fhager, S. Candefjord, M. Elam, and M. Persson, “Microwave Diagnostics Ahead: Saving Time and the Lives of Trauma and Stroke Patients,” *IEEE Microw Mag*, vol. 19, no. 3, pp. 78–90, 2018, doi: 10.1109/MMM.2018.2801646.

[60] J. A. Tobon Vasquez *et al.*, “A Prototype Microwave System for 3D Brain Stroke Imaging,” *Sensors*, vol. 20, no. 9, p. 2607, May 2020, doi: 10.3390/s20092607.

[61] J. A. Tobon Vasquez *et al.*, “Design and Experimental Assessment of a 2D Microwave Imaging System for Brain Stroke Monitoring,” *Int J Antennas Propag*, vol. 2019, pp. 1–12, 2019, doi: 10.1155/2019/8065036.

[62] J. Vrba, *Lékařské apliakce mikrovlnné techniky*. Vydavatelství ČVUT, 2003. Accessed: Jan. 12, 2019. [Online]. Available: https://search.mlp.cz/cz/titul/lekarske-aplikace-mikrovlnne-techniky/2387750/

[63] W. J. Ellison, “Permittivity of Pure Water, at Standard Atmospheric Pressure, over the Frequency Range 0–25THz and the Temperature Range 0–100°C,” *J Phys Chem Ref Data*, vol. 36, no. 1, pp. 1–18, Mar. 2007, doi: 10.1063/1.2360986.

[64] Erik G. Lee, R. L. Hadimani, and D. C. Jiles, “„Population Head Model Repository V1.0". IT’IS Foundation.” [Online]. Available: https://itis.swiss/virtual-population/regional-human-models/phm-repository/v1-0/

[65] “IEEE 1528-2013 - IEEE Recommended Practice for Determining the Peak Spatial-Average Specific Absorption Rate (SAR) in the Human Head from Wireless Communications Devices: Measurement Techniques.” Accessed: Oct. 17, 2010. [Online]. Available: https://standards.ieee.org/findstds/standard/1528-2013.html

[66] J. Tesarik, O. Fiser, and L. Diaz, “Prototype of Simplified Microwave Imaging System for Brain Stroke Follow Up,” *Lhotska L., Sukupova L., Lacković I., Ibbott G. (eds) World Congress on Medical Physics and Biomedical Engineering 2018. IFMBE Proceedings, vol 68/3. Springer, Singapore*, vol. 68/3, pp. 771–774, 2019.

[67] R. Scapaticci, J. Tobon, G. Bellizzi, F. Vipiana, and L. Crocco, “Design and Numerical Characterization of a Low-Complexity Microwave Device for Brain Stroke Monitoring,” *IEEE Trans Antennas Propag*, vol. 66, no. 12, pp. 7328–7338, Dec. 2018, doi: 10.1109/TAP.2018.2871266.

[68] O. M. Bucci, L. Crocco, R. Scapaticci, and G. Bellizzi, “On the Design of Phased Arrays for Medical Applications,” *Proceedings of the IEEE*, vol. 104, no. 3, pp. 633–648, 2016, doi: 10.1109/JPROC.2015.2504266.

[69] J. Sachs, S. Ley, T. Just, S. Chamaani, and M. Helbig, “Differential ultra-wideband microwave imaging: Principle application challenges,” 2018. doi: 10.3390/s18072136.

[70] E. C. Fear, X. Li, S. C. Hagness, and M. A. Stuchly, “Confocal microwave imaging for breast cancer detection: Localization of tumors in three dimensions,” *IEEE Trans Biomed Eng*, vol. 49, no. 8, pp. 812–822, 2002, doi: 10.1109/TBME.2002.800759.

[71] O. Fiser *et al.*, “UWB Bowtie Antenna for Medical Microwave Imaging Applications,” *IEEE Trans Antennas Propag*, vol. 70, no. 7, pp. 5357–5372, 2022, doi: 10.1109/TAP.2022.3161355.

[72] E. Schena, D. Tosi, P. Saccomandi, E. Lewis, and T. Kim, “Fiber optic sensors for temperature monitoring during thermal treatments: An overview,” *Sensors (Switzerland)*, vol. 16, no. 7, pp. 1–20, 2016, doi: 10.3390/s16071144.

[73] A. Bakker *et al.*, “Clinical feasibility of a high-resolution thermal monitoring sheet for superficial hyperthermia in breast cancer patients,” *Cancers (Basel)*, vol. 12, no. 12, pp. 1–18, 2020, doi: 10.3390/cancers12123644.

[74] C. Wyatt *et al.*, “Hyperthermia MRI Temperature Measurement: Evaluation of Measurement Stabilization Strategies for Extremity and Breast Tumors NIH Public Access,” *Int J Hyperthermia*, vol. 25, no. 6, pp. 422–433, 2009, doi: 10.1080/02656730903133762.

[75] S. K. Das, E. A. Jones, T. V Samulski, S. K. Das{, E. A. Jones{, and T. V Samulski{, “A method of MRI-based thermal modelling for a RF phased array,” *International Journal of Hyperthermia*, vol. 17, no. 6, pp. 465–482, 2001, doi: 10.1080/02656730110068320.

[76] A. Semonche *et al.*, “MR-Guided Laser Interstitial Thermal Therapy for Treatment of Brain Tumors”, Accessed: Jun. 24, 2024. [Online]. Available: www.intechopen.com

[77] S. Ley, S. Schilling, O. Fiser, J. Vrba, J. Sachs, and M. Helbig, “Ultra-wideband temperature dependent dielectric spectroscopy of porcine tissue and blood in the microwave frequency range,” *Sensors (Switzerland)*, vol. 19, no. 7, 2019, doi: 10.3390/s19071707.

[78] J. J. Mallorqui, A. Broquetas, L. Jofre, and A. Cardama, “Non-invasive active thermometry with a microwave tomographic scanner in hyperthermia treatments in hyperthermia treatments,” 1992.

[79] J. T. Chang, K. Paulsen, P. Meaney, and M. Fanning, “Non-invasive thermal assessment of tissue phantoms using an active near field microwave imaging technique,” *International Journal of Hyperthermia*, vol. 14, no. 6, pp. 513–534, 1998, doi: 10.3109/02656739809018252.

[80] P. M. Meaney *et al.*, “Microwave thermal imaging: Initial in vivo experience with a single heating zone,” *International Journal of Hyperthermia*, vol. 19, no. 6, pp. 617–641, 2003, doi: 10.1080/0265673031000140822.

[81] M. Haynes, J. Stang, and M. Moghaddam, “Real-time microwave imaging of differential temperature for thermal therapy monitoring.,” *IEEE Trans Biomed Eng*, vol. 61, no. 6, pp. 1787–97, Jun. 2014, doi: 10.1109/TBME.2014.2307072.

[82] M. Ghaderi Aram, L. Beilina, and H. Dobsicek Trefna, “Microwave thermometry with potential application in non-invasive monitoring of hyperthermia,” *J Inverse Ill Posed Probl*, vol. 28, no. 5, pp. 739–750, 2020, doi: 10.1515/jiip-2020-0102.

[83] G. Chen, J. Stang, M. Haynes, E. Leuthardt, and M. Moghaddam, “Real-Time Three-Dimensional Microwave Monitoring of Interstitial Thermal Therapy,” *IEEE Trans Biomed Eng*, vol. 65, no. 3, pp. 528–538, 2018, doi: 10.1109/TBME.2017.2702182.

[84] H. Onal, T. Yilmaz, and M. N. Akinci, “A BIM-Based Algorithm for Quantitative Monitoring of Temperature Distribution During Breast Hyperthermia Treatments,” *IEEE Access*, vol. 11, pp. 38680–38695, 2023, doi: 10.1109/ACCESS.2023.3253482.

[85] O. Fiser, S. Ley, M. Helbig, J. Sachs, M. Kantova, and J. Vrba, “Temperature dependent dielectric spectroscopy of muscle tissue phantom,” *Proceedings of European Microwave Conference in Central Europe, EuMCE 2019*, pp. 550–553, 2019.

[86] T. Rydholm, “Experimental Evaluation of a Microwave Tomography System for Breast Cancer Detection,” 2018, [Online]. Available: https://research.chalmers.se/en/publication/505529

[87] P. Takook, M. Persson, J. Gellermann, and H. D. Trefná, “Compact self-grounded Bow-Tie antenna design for an UWB phased-array hyperthermia applicator,” *International Journal of Hyperthermia*, vol. 33, no. 4, pp. 387–400, May 2017, doi: 10.1080/02656736.2016.1271911.